

TECHNISCHE UNIVERSITÄT DARMSTADT

GSI - HELMHOLTZZENTRUM FÜR
SCHWERIONENFORSCHUNG GMBH

DOKTORARBEIT

**Shell structure in the vicinity of the
doubly magic ^{100}Sn via Coulomb
excitation at PreSPEC**

Referent:

Prof. Dr. Dr. h.c.

Norbert PIETRALLA

Korreferent:

Prof. Dr. Thomas AUMANN

Externe Betreuerin:

Dr. Magdalena GÓRSKA

Vom Fachbereich Physik der Technischen Universität Darmstadt

zur Erlangung des Grades eines Doktors der Naturwissenschaften (Dr. rer. nat.)

genehmigte Dissertation von M. Sc. Physics

Giulia Guastalla

aus Mantova, Italien



Darmstadt 2014

D 17

Tag der Einreichung: 14.10.2014

Tag der Prüfung: 17.11.2014

Abstract

The PreSPEC setup in combination with the high intensity primary beams available at GSI provided unique opportunities for the key nuclear structure studies on exotic nuclei. The experiment performed on the neutron deficient ^{104}Sn aimed to deduce the reduced transition probability of the first excited 2^+ state quantified by the $B(\text{E}2; 0^+ \rightarrow 2^+)$ value. This result is the central point in the discussion of the evolution of nuclear structure in proximity of the doubly magic nucleus ^{100}Sn . As ^{100}Sn is not yet accessible for such measurements, a series of experiments have been performed for neutron-deficient Sn isotopes over the past few years. These data showed excessive experimental $B(\text{E}2)$ strength compared to shell model calculations below neutron number $N=64$ and they are therefore not excluding a constant or even increasing collectivity below ^{106}Sn . Hence, the measurement of the $B(\text{E}2)$ value in the next even-even isotope toward ^{100}Sn , i.e. ^{104}Sn , was a crucial step to verify the robustness of the shell gap of ^{100}Sn . Moreover, ^{104}Sn is the heaviest isotope of the Sn isotopic chain for which a shell model calculation without significant truncation of the valence space can be performed and therefore with this experimental value the validity of Large Scale Shell Model (LSSM) calculations could be tested. As a main result of the experiment a $B(\text{E}2)$ value corresponding to $0.10(4) \text{ e}^2\text{b}^2$ has been extracted for ^{104}Sn . The experimental value showed a very good agreement with the predicted one and, despite the large error bar, it clearly established a downward trend of the $B(\text{E}2)$ values of the Sn isotopic chain toward $A=100$. This implied enhanced stability of the $N = Z = 50$ shell closure against ph-excited quadrupole modes. However, an experiment of this kind is very challenging for several reasons. First, ^{104}Sn lies in proximity of the proton drip line and has therefore a small production cross section, second, the high energy of the beam causes a large background which by far dominates the γ -ray spectra. To overcome the last aspect, an investigation of the components of the background has been performed taking advantage of the complexity of the PreSPEC experimental setup, which provides over 1000 parameters for the detailed analysis of the events. In addition to the known radiation produced in atomic processes, evidences of interactions of high energy protons, provoking a loss of the detection efficiency and a worsening of the quality of the data, have been observed. However, from the new information obtained on the background in the PreSPEC data, several improvements of the setup are suggested in view of new challenging experiments in the future with HISPEC/DESPEC at the FAIR facility.

Kurzfassung

An der GSI hat die Kombination von hochintensiven Primärstrahlen mit dem PreSPEC Setup für hochpräzise Gammaspektroskopie einzigartige Möglichkeiten für Experimente mit exotischen Atomkernen geboten. Das Experiment, das an dem neutronenarmen Kern ^{104}Sn durchgeführt wurde, hatte zum Ziel die reduzierte Übergangswahrscheinlichkeit des ersten angeregten 2^+ Zustands - $B(E2; 0^+ \rightarrow 2^+)$ - zu bestimmen. Dieser Wert spielt eine zentrale Rolle bei der Diskussion der Evolution der Kernstruktur in der Nähe des doppelt magischen Kerns ^{100}Sn . Da ^{100}Sn nicht direkt für solche Experimente verfügbar ist, wurden in den vergangenen Jahren eine Reihe von Experimenten mit immer neutronenärmeren Sn Isotopen durchgeführt. Die experimentell gefundenen $B(E2)$ Werte für Sn Isotope mit weniger als $N=64$ Neutronen stehen im Gegensatz zum Trend der von Schalenmodellrechnungen vorhergesagt wird. Tatsächlich konnte anhand der experimentellen Daten konstante oder sogar ansteigende Kollektivität für Sn Isotope leichter als ^{106}Sn bisher nicht ausgeschlossen werden. Daher war die Messung des $B(E2)$ Wertes in ^{104}Sn ein entscheidender Schritt, um die Robustheit des Schalenabschlusses in ^{100}Sn zu verifizieren. Darüberhinaus ist ^{104}Sn bisher das schwerste Sn Isotop für das Schalenmodellrechnungen ohne signifikante Trunkierung des Valenzraumes durchgeführt werden können. Daher bietet die experimentelle Messung eine einzigartige Möglichkeit Ergebnisse von LSSM-Rechnungen (Large Scale Shell Model) mit experimentellen Daten zu vergleichen. Als wichtigstes Ergebnis des Experiments konnte eine reduzierte Übergangswahrscheinlichkeit von $B(E2) = 0.10(4) e^2 b^2$ für ^{104}Sn bestimmt werden. Dieser Wert ist in guter Übereinstimmung mit dem vorausgesagten Wert und deutet - trotz der relativ grossen Fehlerunsicherheit ? auf einen abnehmenden Trend der $B(E2)$ Werte in den Sn Isotopen in Richtung $A=100$ hin. Daher konnte auf erhöhte Stabilität des $N = Z = 50$ Schalenabschlusses gegenüber Quadrupol Anregungsmoden geschlossen werden. Experimente dieser Art stellen aus verschiedenen Gründen eine grosse Herausforderung dar. Einerseits ist ^{104}Sn nahe der Protonen-Dripline und hat daher einen kleinen kleinen Produktionswirkungsquerschnitt. Des Weiteren wird durch die, zur Produktion nötige, hohe Strahlenergie Hintergrundstrahlung erzeugt, die das gemessene Spektrum dominiert. Daher wurden die einzelnen Komponenten des Hintergrundes untersucht, wobei die Komplexität des PreSPEC Setups mit über 1000 Parametern ausgenutzt wurde, die eine detaillierte

Contents

Analyse ermöglichten. Zusätzlich zu der bekannten Hintergrundstrahlung, die von atomaren Prozessen ausgeht, konnten Hinweise auf Wechselwirkungen von hochenergetischen Protonen identifiziert werden, die einen negativen Effekt auf die Effizienz der Messung und die Qualität der gemessenen Spektren hatten. Ausgehend von diesen neuen Erkenntnissen zur Herkunft der Hintergrundstrahlung konnten verschiedene Verbesserungen des experimentellen Aufbaus, im Hinblick auf zukünftige Experimente mit dem HISPEC/DESPEC-Setup an FAIR, gemacht werden.

Contents

Abstract	iii
Kurzfassung	v
List of Figures	ix
List of Tables	xv
1 Introduction	1
2 Stability of the shell closure at $N=Z=50$	7
2.1 Introduction to Large Scale Shell Model calculations	7
2.1.1 The effective residual interaction	9
2.1.2 The monopole interaction	10
2.2 Nuclear structure in ^{100}Sn	11
2.3 The $B(E2)$ values in the tin isotopic chain	14
3 The PreSPEC fast-beam setup	17
3.1 Radioactive beams at FRS	18
3.1.1 Production mechanism	18
3.1.2 Separation method	20
3.1.3 FRS detectors	21
3.2 Isotope identification after the secondary reaction: LYCCA	23
3.3 The EUROBALL cluster array and AGATA	25
3.3.1 The EUROBALL cluster array	25
3.3.2 AGATA	27
3.4 Atomic and nuclear background	28
4 Experimental details and data analysis of the $B(E2)$ value measurement in ^{104}Sn	33
4.1 Relativistic Coulomb excitation	34
4.2 Analysis of the data	36
4.2.1 Calibration of the MUSIC	36
4.2.2 Calibration of the ToF	38

4.2.3	A/q correction for position dependency	40
4.2.4	Isotope selection	41
4.2.5	Determination of the velocity of the ions after the target	44
4.2.6	γ -time range selection	45
4.2.7	Scattering angle range selection	46
4.3	Extraction of the result and discussion	47
4.3.1	Estimation of the background level	49
4.3.2	Extraction of the B(E2) value	50
4.3.3	Result and comparison with LSSM calculations	51
5	Analysis of the background observed with PreSPEC	57
5.1	Background analysis with Euroball data	58
5.2	Information on the background events from AGATA	69
5.3	Impact of the background for PreSPEC experiments	72
5.4	Summary and conclusions	82
	Acknowledgements	93

List of Figures

1.1	Chart of nuclei (also called Segré chart). ^{100}Sn lies at the $\text{N}=\text{Z}$ line and, at the same time, at the limit of stability for proton-emission [3].	2
2.1	Single-particle energy spectra in ^{56}Ni and ^{100}Sn [30]. The levels are shown relative to the middle of the gap (λ_f) which accounts for Coulomb shift (ΔE_c) between proton and neutrons. Experimental values for ^{56}Ni are compared to updated extrapolations for ^{100}Sn [19].	13
2.2	Experimental $\text{B}(\text{E}2)$ values of the even-mass Sn isotopes, compared to SM predictions. The data were measured at REX-ISOLDE [38, 39], MSU [40], IUAC [41], GSI [42–44], ORNL [45, 46].	14
3.1	Cross section for the production of Sn isotopes via fragmentation of ^{129}Xe and ^{124}Xe on a ^{27}Al target, and via fission of ^{238}U on a ^{208}Pb target [56].	19
3.2	Schematic drawing of the FRS. The trajectory of ions with a specific A/q and with the achromatic setting of FRS are drawn in red. The slits are represented in green and the focal planes are indicated by the letter F and consecutive numbers.	21
3.3	Photograph of the Finger detector in use from 2010 to 2012. The area of the detector was divided in 15 strips to allow good detection efficiency at high rates [58].	22
3.4	Identification plots of the ions in FRS with high ion rates (10^5 s^{-1}): the A/q value, deduced from ToF measurements, is plotted versus the proton number Z , obtained from the MUSIC. In the figure on the left the ToF was obtained using the Finger detector, while in the figure on the right a standard scintillator was used at the intermediate focal plane. Sufficient A/q resolution of the Finger detector in contrast to the standard scintillator is evident from this comparison.	23
3.5	Schematic drawing of the LYCCA setup. For more details on the use of each detector see the text.	24
3.6	Representation of one module of the LYCCA $\Delta\text{E-E}$ wall telescope. The DSSSD detector, divided in 32 strips, is placed in front of an array of 9 (3×3) $\text{CsI}(\text{Tl})$ scintillators.	24
3.7	Doppler broadening of the energy of the γ -rays as a function of the angle of emission, considering the opening angle of $\sim 3^\circ$ of the EUROBALL crystals. The red line indicates approximately the largest observation angle of the EUROBALL crystals. In the inset a photograph of a cluster detector consisting of seven crystals is shown.	26

3.8	Photograph of the PreSPEC setup. The beam comes from the lower left side.	27
3.10	Short traces from an AGATA crystal, superimposed using different colors. The height of the trace is proportional to the energy deposited by the radiation. The white trace, at variance with the others, shows a saturation of the energy range.	28
3.9	Drawing of an AGATA crystal. Each crystal is electrically divided in 36 segments, six azimuthal and six axial, plus a central contact, named <i>core</i>	28
3.11	Angle-integrated cross section as a function of γ -ray energy for the atomic background from ^{132}Sn on a ^{208}Pb target at different beam energies.	30
3.12	γ -ray energy spectrum of a EUROBALL cluster from an in-beam experiment at PreSPEC. The peaks on top of the smooth background are coming from nuclear reactions of the beam impinging on the surrounding material.	31
4.1	Beam energy versus Coulomb excitation cross sections for the first excited 2^+ and 3^- states and the giant dipole resonance (GDR), for a ^{136}Xe beam incident on a Pb target. A minimum impact parameter of 16 fm is assumed in the calculation [60].	35
4.2	Schematic drawing of the Coulomb excitation reaction.	36
4.3	β values of the Xe beam versus the energy loss in the MUSIC. The data are fitted with a polynomial function of second order.	37
4.4	Z values obtained after calibrating the energy loss signals in the MUSIC detector for the dependency of the energy loss in the gas with the velocity of the fragments, for the ^{104}Sn measurements.	38
4.5	Plot of β versus $TOF_m \cdot \beta$ used to calibrate the ToF in relation to the velocity of the fragments. The range spanned by the three points, obtained using the primary beam at different energies, includes the expected energy of the fragments. The function used for the fit was a polynomial of first order.	39
4.6	Position of the ion from the TPC versus the time difference of the two PMTs signals of the scintillator at the final focal plane.	40
4.7	A/q versus the position of the ions from a TPC at the final focal plane, for the ^{104}Sn measurement. On the left it is possible to observe a dependency of A/q on the position, while on the right the same plot is shown with a correction of this dependency applied.	41
4.8	A/q distribution deduced from ToF measurement versus Z of the ions obtained from the MUSIC, for the ^{104}Sn measurement. The values of A/q have been corrected for the dependency on the x position at the final focal plane (see Par. 4.2.3).	42
4.9	Spectrum of the values of Z obtained from the MUSIC detector. The events between the two red lines are the ones selected for the analysis of ^{104}Sn	42
4.10	A/q from ToF measurement versus the position on the x axis of the ions at the final focal plane from the TPC, after a restriction on the nuclei with $Z=50$ has been applied to the data.	43

4.11 Total energy deposited by the ions in the CsI(Tl) crystals of the LYCCA wall telescope versus the energy loss from the DSSSD detectors for the events selected as ^{104}Sn in the FRS. The graphical cut, shown with a black line, selects the ions that had the same Z before and after the target.	44
4.12 Doppler corrected γ -ray energy spectra (x axis) performed for twenty different values of β (y axis). The latter were obtained decreasing of 0.1 % at each step the event-by-event value measured in FRS. The final spectrum has been chosen by looking at the projections on the x axis [67].	45
4.13 Time spectrum from the Germanium detectors (the scale is inverted). The borders of the chosen time range are shown by the two red lines (about 15 ns).	46
4.14 Examples of γ -ray energy spectra produced gating on different ranges of the scattering angle for the ^{112}Sn experimental data. Below 15 mrad the contribution from elastic scattering is covering the peak corresponding to the $2_1^+ \rightarrow 0^+$ transition.	47
4.15 Doppler corrected energy spectra for ^{112}Sn (upper panel), and for ^{104}Sn (lower panel). The peak associated to the $2^+ \rightarrow 0^+$ transition is indicated by the arrow. The dashed line indicates the estimated background level.	48
4.16 Simulated peak shape for the $2^+ \rightarrow 0^+$ transition for ^{112}Sn (up) and ^{104}Sn (down) considering the energy straggling in the target. The FWHM is 36 keV and 22 keV respectively. The simulation has been performed considering a fixed incoming velocity and only one angle for the Germanium detector (courtesy of P. Boutachkov).	49
4.17 Experimental $B(E2; 0^+ \rightarrow 2^+)$ values for $^{104-114}\text{Sn}$. The average of the $B(E2)$ values in $^{106-114}\text{Sn}$, weighted on the respective uncertainties, is indicated by the yellow band (see references in the caption of Fig. 2.2) [72]. For ^{104}Sn , the results obtained from measurements performed in GSI, RIKEN [73] and MSU [74] and the average of the three values, weighted on the respective uncertainties, are reported.	52
4.18 The $B(E2)$ values calculated considering an isovector-dependent neutron effective charge, normalized at $N=66$, and SPE states fitted on the excited states in the tin isotopes [76, 77] are represented by a thick black line (picture modified from Ref. [77]). The thin black line and the experimental $B(E2)$ values are described in the caption of Fig. 2.2.	55
5.1 Time versus energy values of the hits in a crystal of the Euroball Cluster array (the time axis is reversed, i.e. the earliest events are on the right) and the projections on the x (time) and y (energy) axis. The time ranges A, B, C and D are defined in Tab. 5.1.	59
5.2 Crystal time spectra for the different energy ranges (from top to down: good, low, overflow and missing energy values). The vertical lines show the boundaries of the time ranges considered. The x axis is, as in the previous spectra, reversed.	61
5.3 Time spectrum of the crystals selecting the hits with energy values between 80 and 6800 keV. The time axis is, as in the previous spectra, reversed.	62

5.4 Cluster multiplicity for hits in time range A (black line), B (red line), in C (green line) and in D (blue line), normalized at the values for multiplicity one. No energy condition has been applied. It can be observed that in the first two cases, the cluster multiplicity is mainly one. In the time range C, instead, in addition to the peak at multiplicity one, a peak at multiplicity six is also present. In the time range D, the cluster multiplicity is mainly one and two but higher multiplicities are also present in a considerable amount.	63
5.5 Scheme representing the arrangement of the 15 clusters of the Euroball array. The crystals are numbered from 0 to 6, anticlockwise, and 6 is always the central one. In this scheme, the number in the central crystal refers to the cluster number. The crystals drawn in black are not considered due to bad or missing response of the detectors.	64
5.6 Hit pattern of the Euroball array when signals in time range C are selected. The clusters with a higher numbers of counts (0, 1, 6, 7, 8) are the ones forming the inner ring. The hit pattern for signals in time range A and B is similar.	65
5.7 Hit pattern of the Euroball array when signals in time range D are selected. The clusters with a higher numbers of counts (1, 6, 7, 11, 12) are in an horizontal band in the upper part of the array (see scheme in Fig. 5.5).	65
5.8 Position of the ions at the final focal plane of FRS from the TPC detector (scale reversed) versus the cluster number of the inner ring which registered a hit in coincidence. In the upper plot, the events with cluster multiplicity equal to six in the first delayed time peak (C) are selected, while in the lower plot events that produce low cluster multiplicity in the prompt time peak (B) are chosen. Only in the first case, a correlation between the position of the beam and the hit in the germanium detectors is noticeable.	66
5.9 Energy loss (ΔE) in the target DSSSD selecting events with cluster multiplicity one and two in the time range B (black line), equal to six in the time range C (red line) and array multiplicity higher then six (blue line) in the time range C. All the distributions have been normalized at $\Delta E = 1200$ keV.	67
5.10 X position versus y position of the hit in the TPC at the final focal plane. The area has been divided in three regions (a , b , c), in order to verify the variation of the number of counts in the lateral region with respect to the center, applying different analysis conditions. For this picture, the condition on energy loss in the target DSSSD lower then 1000 keV has been applied.	68
5.11 γ -ray energy spectra selecting the events with array multiplicity equal to one or two in the time range B (red line) and the events with array multiplicity higher then six in the time range C (blue line). In the first case, only the 511 keV transition (the energy released by the positron-electron annihilation) is pronounced above the smooth exponential background. In the second case, the 596 keV and the 834 keV neutron lines are clearly visible.	69

5.12	γ -ray energy spectrum of an AGATA crystal, from an experiment of the PreSPEC fast-beam campaign. The broad peak at very high energies is caused by the saturation of the preamplifier.	70
5.13	Core preamplifier signals of an AGATA crystal. The trace on the left has the typical shape, with an exponential decay, while the trace on the right saturates the range of the preamplifier. The energy range, in this case, was 22 MeV.	70
5.14	Distribution of the overflows in AGATA, normalized to a central crystal.	71
5.15	Distribution of the regular energy signals in AGATA, normalized to a central crystal.	71
5.16	Array multiplicity of hits with energy higher than 500 keV in the prompt time range. A selection on the events with cluster multiplicity equal to six in the time range C and with at least a hit with energy between 1000 keV and 3000 keV in the time range B is applied.	73
5.17	Examples of possible hit patterns in the Euroball array when multiplicity six in the time range C (pink crystals) occurs in coincidence with multiplicity higher than one in the time range B (yellow crystals). The case of prompt hits well separated from the saturated crystals is shown on the left. An example of an event with the prompt hits in the vicinity of the saturated crystals is on the right.	73
5.18	Array multiplicity of all the hits in the good energy range after add-back.	74
5.19	Array multiplicity of all the hits between 1000 - 3000 keV after add-back.	75
5.20	Array multiplicity for the events with at least a bad hit (58 % of the total number of events) (from top to bottom: for the inner, the middle and the outer ring).	78
5.21	Array multiplicity for the events with only good hits (42 % of the total number of events) (from top to bottom: for the inner, the middle and the outer ring).	79
5.22	Array multiplicity of all the hits in the event (from top to bottom: for the inner, the middle and the outer ring).	81

List of Tables

2.1	Information on ^{100}Sn from Refs. [28, 29].	12
2.2	B(E2) values of the Sn isotopes shown in Fig. 2.2.	16
4.1	Results for the B(E2) value measurements performed on ^{104}Sn at the different laboratories and the average of the three values, weighted on the respective uncertainties.	53
5.1	Classification of hits according to the time registered in the array. In the third column, the occurrence of events with at least one of these hits is given in percent with respect to the total number of events.	60
5.2	Classification of hits according to the energy registered in the array. In the third column, the occurrence of events with at least one of these hits is given in percent with respect to the total number of events.	60
5.3	Percent of events with at least one hit within the specific energy range and the different time intervals, among the total number of events with at least a hit in the same time range.	60
5.4	Fraction of counts on the sides (a and c) and on the center (b) at the TPC at the final focal plane, when the different conditions listed are applied. It can be notice that, when a signal is registered in both target and wall DSSSD, the hits in the TPC are more concentrated in the center. Requiring cluster multiplicity six in the time range C and/or low energy loss in target DSSSD, instead, the number of counts on each side exceed the number of counts in the center.	68
5.5	Average presence of the different hit types in the three rings of the Euroball array, per crystal and per event, when at least one bad hit is present (58 % of the total number of events).	76
5.6	Average presence of the hits with good energy values in the three rings of the Euroball array, per crystal and per event, when no bad hits are present (42 % of the total number of events).	76
5.7	Calculated efficiencies of the three rings (positioned at 700 mm distance from the target) of the full Euroball Cluster array, for γ -rays of energy equal to 1.3 MeV, and the efficiencies scaled considering only the available crystals.	77
5.8	Reduced efficiency for the detection of one γ -ray in the three rings of the Euroball cluster array when the number of crystals is decreased in relation to the multiplicity of bad hits.	77

5.9 Reduced efficiency for the detection of one γ -ray in the three rings of the Euroball cluster array when the number of crystals is decreased in relation to the multiplicity of all the hits.	80
------------------------------------------------------------------------------------------------------------------------------------------------------------------------------------------------------------------	----

Chapter 1

Introduction

An open challenge for fundamental physics is to reach a comprehensive understanding of the nuclear force that rules the evolution of the nuclear structure throughout the Segré chart [1]. The complexity of this force can be deduced from the large diversity of phenomena (as the various collective modes and shapes) that appears in different nuclear systems. Models that aim to become general and reliable nuclear theories need therefore to include constraints from different regions of the chart of nuclides.

The nuclear Shell Model (SM) is based on the prediction of groups of orbitals, named *shells*, separated by energy gaps at the *magic numbers* (2, 8, 20, 28, 50, 82, ...) for which corresponding shells are filled [2]. This approach allows to reduce the numerical complexity inherent the nuclear system (many-body problem) in an advantageous way: the particles in the filled shells are considered as non-interacting, thus only the valence nucleons and a limited number of orbitals in which they can scatter are considered. A weak point of the model is the derivation of the interaction between nucleons from experimental data, which entails a strong dependency of the interaction on the mass region considered for its derivation and on the availability of experimental information in the same region. As a consequence, predictions become less reliable for radioactive nuclei, often referred to as *exotic* since they are not present in the material forming our world. Due to their low production cross sections, these nuclei cannot be easily accessed by direct measurements and therefore very few experimental data provide benchmarks for the theoretical models. Nuclei with unusual proton-to-neutron ratio, moreover, are important as they can show enhanced or unpredicted features of the effective nuclear force and thus provide crucial information for a qualitative and quantitative progress of the nuclear structure models.

A radioactive nucleus of particular interest is the very neutron-deficient $^{100}\text{Sn}_{50}$. A double shell closure, expected for the two-fold presence of the magic number 50, would provide an inert core and thus a starting point for SM predictions in this region of the nuclear chart. Moreover, as it lies on the $N=Z$ line (i.e. it is *self-conjugated*), it can show enhanced effects of the residual interaction between protons and neutrons occupying identical orbitals. Furthermore, as ^{100}Sn is close to the proton drip-line (the limit of stability for proton emission, see Fig. 1.1), it is the heaviest nucleus in the Segré chart which combines the aforementioned peculiarities. Hence, it represents a cornerstone for nuclear structure studies.

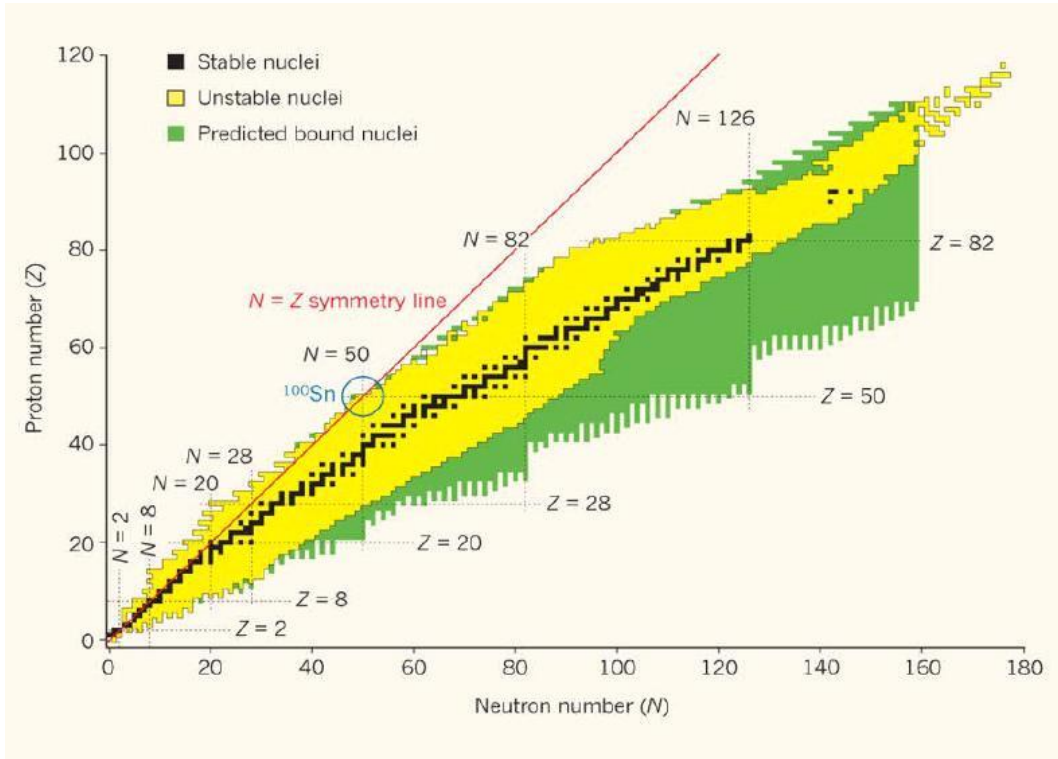


FIGURE 1.1. Chart of nuclei (also called Segré chart). ^{100}Sn lies at the $N=Z$ line and, at the same time, at the limit of stability for proton-emission [3].

In the past decades, along with improvements of radioactive beams, the target of the experiments could move toward more and more unstable nuclei, providing insights on the structure of very exotic nuclei. Experimental investigations around ^{100}Sn , in particular, aimed to verify whether the predicted shell closure is confirmed or it is broken by strong residual correlations [4]. However, the very low intensity of the radioactive beams and the presence of large background from reactions have been an obstacle for the measurement of many relevant observables. Reactions in inverse

kinematics of the one-particle (hole) neighbors are not feasible, at present and in the foreseeable future, due to the very low cross section for the production of this isotopes. Consequently, spectroscopic factors are not obtainable and the single-particle energy spectrum of ^{100}Sn can be built only from the observation of excited states of the neighboring nuclei and via extrapolations from more remote nuclei. Lifetime measurements of low-lying excited states of the light tin isotopes are also not feasible due to the presence of low-lying 6^+ isomers ($> \text{ns}$) that would hamper the measurement of the underlying short-living ($< \text{ns}$) states. On the other hand, the presence of isomers are in turn sources of important information. In the case of the ^{100}Sn region, in particular, the observation of core-excited isomers and spin-gap isomers allows to study the role of core excitations and p-n correlations, respectively [5]. Furthermore, studies of the systematics of seniority isomers along an isotopic chain can be used as a signature of the presence of a shell closure and the concomitant wave-function purity [6]. In neutron-deficient nuclides, the shell structure can also be investigated through the α -emission process. The probability of α -cluster formation, indeed, contains information on the structure of the states connected by α -transitions and it is influenced by the presence of shell closures. The observed increase of the α -decay energy in the transition decay chains has been considered a result of the strong binding of nucleons in the vicinity of ^{100}Sn and therefore a direct proof of the $\text{N}=\text{Z}=50$ shell closure [7].

Measurements which more closely approached ^{100}Sn and provided important information on its structure have been carried out in the last years at GSI. The PreSPEC project (2010-2014) combined radioactive beams provided by the SIS/FRS facility with state-of-the-art γ -ray spectrometers (EUROBALL cluster array and AGATA) for in-beam γ -ray spectroscopy measurements on very unstable nuclei. The complexity of the experiments (over 1000 parameters and up to 11 VME crates), necessary for the full identification of each event, made them the most challenging experiment in nuclear structure research. In addition, the large number of indispensable detectors present along the beam line were sources of unwanted reactions which interfered with the observation of the physical process of interest. An accurate analysis of the data and a good understanding of the background reactions have played therefore a fundamental role for the extraction of the physics result. One of the recent important results has been obtained from the measurement of the transition probability (or strength) of the Gamow-Teller (GT) decay of ^{100}Sn to ^{100}In . This type of decay occurs between orbitals that have the same angular momenta but can have different spin. Its strength is therefore entirely related to the initial and to the final state of the decay and it provides indications of the purity of the states involved. Despite the low intensity of the radioactive beam (0.75 ^{100}Sn nuclei per hour), the large energy window for the

β -decay (~ 7.4 MeV), allowed to obtain significant results. The very large GT decay strength measured, denominated *super-allowed*, gave indeed evidence of the purity of the ground state in ^{100}Sn and of the first excited state in ^{100}In [8]. This result established the first direct proof of the robustness of the $N=Z=50$ shell closure [8]. To directly investigate then the role of the quadrupole collectivity on the stability of the shell closure, the observable of choice is the reduced transition probability for the electromagnetic transition from the ground state (g.s.) to the first 2^+ state, the $B(E2; 0^+ \rightarrow 2^+)$ value (in the following abbreviated as $B(E2)$). This observable is indeed directly related to the reduced matrix element for the E2 transition between the wave function Ψ_i of the initial state J_i and the wave function Ψ_f of the final state (J_f) (in this case the 0^+ and the 2^+ state, respectively), as it is defined as [9]:

$$B(E2; J_i \rightarrow J_f) = \frac{1}{2J_i + 1} |\langle \Psi_f | E2 | \Psi_i \rangle|^2. \quad (1.1)$$

$B(E2)$ values are frequently expressed in units of $e^2\text{fm}^4$ or $e^2\text{b}^2$, where e is the charge of the electron. They can also be found in literature in terms of Weisskopf units (W.u.), which give an estimate of the $B(E2)$ with respect to the single-particle proton transition. The relation between the mentioned scales is $B(E2)_{w.u.} = 0.05940 \text{ A}^{4/3} e^2\text{fm}^4$ for a decay transition. The $B(E2)$ value, as described above, is related to the transition probability of the opposite transition (i.e. the $2^+ \rightarrow 0^+$ decay) by a factor 5. As the $B(E2)$ value in ^{100}Sn is not at the moment accessible at the present facilities, predictions are made taking into account the trend of the $B(E2)$ values in the more easily accessible tin isotopes. The central topic of this work is the measurement of the $B(E2)$ value in ^{104}Sn , the closest isotope to ^{100}Sn reached so far.

In Chapter 2, after an introduction of the SM and Large Scale Shell Model (LSSM) calculations, the nuclear structure of ^{100}Sn inferable from the available direct and indirect observations and from SM calculations is described. In particular, the discrepancy of the measured $B(E2)$ values of the tin isotopic chain with the SM predictions is presented, which calls into question the persistence of the number 50 as a magic number for this unstable nucleus. The FRS and the PreSPEC fast-beam setup, which have been used to perform the measurement of the $B(E2)$ value in ^{104}Sn , are described in Chapter 3. In Chapter 4, an overview of the experiment and of the data analysis performed to suppress the background and to observe the expected peak in the γ -ray spectra are described. Moreover, the $B(E2)$ value extracted for ^{104}Sn has been compared with state-of-the-art Large Scale Shell Model (LSSM) calculations and the interpretation of the experimental result in relation to the debated $N=Z=50$ shell closure is reported.

In Chapter 5, the analysis of the components of background in the ^{104}Sn data and of the impact on experiments at PreSPEC, or similar facilities, are discussed.

Chapter 2

Stability of the shell closure at $N=Z=50$

^{100}Sn , predicted by the Shell Model to be the heaviest self-conjugated doubly-magic nucleus, provides an important benchmark to test the validity of calculations in nuclei far from the valley of stability on its neutron-deficient side. On the other hand, experimental information which would provide constraints for the model are very scarce in this region. Meaningful conclusions on the shell structure in the ^{100}Sn region have been recently obtained with Large Scale Shell Model (LSSM) calculations [8], which use state-of-the-art SM codes capable to treat efficiently large dimensions of the configuration space [10, 11]. In the first part of this chapter, the basics of the Shell model and of LSSM calculations are presented. Afterwards, the present status of the nuclear structure of ^{100}Sn derived from the available experimental evidences and from SM extrapolations is described. Finally, the comparison of the experimental $B(E2)$ values in the Sn isotopic chain with the SM predictions is shown having a central role in the debate on the robustness of the $N=Z=50$ shell closure against core excitation.

2.1 Introduction to Large Scale Shell Model calculations

The nucleus is a complex system of interacting particles whose description through a microscopic approach becomes rapidly intractable as nucleons are added. For medium-heavy-nuclei, methods that simplify the problem allowing, at the same time, the correct reproduction of the low-lying states are required. In the Shell Model, a A -nucleons

system is expressed as the sum of the kinetic energy of each nucleon (T_i) and a two-body nucleon-nucleon interaction ($V(i, j)$) by the Hamiltonian

$$H = \sum_{i=1, \dots, A} T_i + \sum_{i, j=1, \dots, A} V(i, j) . \quad (2.1)$$

Introducing then a one-body central potential $U(r_i)$, the last equation can be rewritten as

$$H = \sum_{i=1, \dots, A} [T_i + U(r_i)] + \sum_{i, j=1, \dots, A} [V(i, j) - U(r_i)] = H^0 + H^{res} . \quad (2.2)$$

In this way, the Hamiltonian is divided in two terms: H^0 , describing the independent motion of the nucleons in a central potential, and H^{res} , representing the residual interaction among the nucleons. To reduce then the dimension of the matrices describing a nuclear system, the *model space*, i.e. the set of orbitals that the particles (holes) can occupy, is separated in two parts: an inert *core*, chosen in correspondence of a completely filled shell (closed shell), and the *valence space*, the group of orbitals above the core where nucleons interact via a residual interaction. Consequently, the general Hamiltonian (2.1) is transformed into an *effective* one

$$H_{\text{eff}} \Psi_{\text{eff}} = E_{\text{eff}} \Psi_{\text{eff}} \quad (2.3)$$

adapted to the restricted basis (Ψ_{eff}). The residual interaction acting between the nucleons outside the core is called *effective interaction* [10].

The valence space has to include all the orbitals relevant for a correct reproduction of the structure of the nucleus, but, at the same time, its size has to be small enough so that the dimension of the matrix is tractable. Especially in the case of medium- and heavy-mass nuclei, the model space that can be treated by standard diagonalization methods [12] is very often too small to reproduce the experimental data in the respective mass region. As a perfectly inert core does not exist in nature, $p-h$ (particle-hole) excitations across the shell gap can have an important role and the valence space has to be extended to orbitals below the shell gap. Hence, the inert core considered in the calculations is chosen at the shell closure below the one under study. In the case of ^{100}Sn , the core assumed is ^{80}Zr ($Z=40$, $N=40$), in order to allow proton or neutron $p-h$ excitations, or ^{90}Zr ($Z=40$, $N=50$), so that only proton $p-h$ excitations take place.

To perform calculations on such large valence spaces, LSSM codes, powerful computer programs that employ algorithms to reduce either the dimension of the basis or the complexity of the calculations, are used. More information on the different LSSM codes are summarized in Refs. [10, 13]. The number of $p - h$ excitations allowed in a calculation are referred to as *truncation scheme* or *truncation level* and are indicated by the letter t . This parameter is chosen in relation to the nucleus considered and the highest value it can assume is determined by the present computational capabilities. In order to include polarization effects of the core that are not considered in the calculation due to the truncation of the valence space, a *polarization charge* (δe), i.e. a factor added to the real charge (e) of protons and neutrons, is used [9].

2.1.1 The effective residual interaction

The effective interaction is the residual interaction which acts between the nucleons in the valence space. Thus, it has to include the effects from the underlying core and from higher orbits. The three different approaches used to derive it are briefly described in the following.

- Empirical. In a simple approach, single particle energies (ϵ_j) are extracted from the difference in *binding energies* (BE) of a nucleus with a *closed shell* (CS) and a nucleus with one nucleon (hole) more (CS ± 1) in the orbital j :

$$\epsilon_j = BE(CS \pm 1; I = j) - BE(CS; g.s.) . \quad (2.4)$$

Hence, it is then possible to obtain a two body matrix element considering a CS ± 2 nucleus as follow:

$$\langle j^2 J | V | j^2 J \rangle = BE(CS \pm 2; j^2, I = J) - BE(CS; g.s.) - 2\epsilon_j . \quad (2.5)$$

Only diagonal TBME can be extracted in this way, which means that model spaces with more than one orbit mixing are neglected [11]. Alternatively, with an iterative procedure, *single particle energies* (generally abbreviated SPEs) and *two-body matrix elements* (TBMEs) are considered as parameters and they are adjusted with a least-squares fit until the calculated energy values reach a convergence with the experimental one. With this method, as a drawback, the interaction obtained has a strong dependence on the set of experimental data used and on the mass region considered [11, 14].

- Schematic. A simple form of the effective interaction can be constructed on basic properties of the nuclear force. A well known example is the surface-delta interaction. It is based on the short-range characteristic of the nuclear force and on three assumptions: 1) the interaction takes place at the surface of the nucleus, 2) the two-body force is present only if the spatial positions of the nucleons are overlapping, 3) the probability to find a particle at the surface is independent of the shell-model orbit in which it moves. Despite its simplicity, it is successfull in describing many nuclear properties [14]. Other types of schematic interactions are the Skyrme [15, 16] and the Gogny [17, 18] interaction, which use relativistic mean fields parameterized to fit experimental gross properties. They have been successfully used to calculate masses, shapes, radii, level densities and single particle energies [19].
- Realistic. The interaction is derived from the NN (*nucleon-nucleon*) potential, obtained from free NN scattering experiments. The strong short-range repulsion present in the bare NN interaction is removed applying the Brückner theory in the form of G-matrix [13, 20]. As the interaction needs to be adapted to valence space considered, a dependence on the mass region is included and a new interaction for every new core nucleus has to be calculated. This problem has been solved with an alternative approach which resulted in the V^{low-k} potential. It can be used to calculate core polarization TBME without A dependence, allowing the same input interaction to be used in different nuclear regions [21]. Moreover, additional corrections to the effective interaction, as couplings to orbits outside the valence space, can be approximately accounted for via perturbative techniques [22].

It is important to point out that the validity of an effective interaction is restricted to the valence space considered for its derivation. Moreover, what does not belong to the model space, as transitions or decays involving orbitals outside the valence space, cannot be calculated reliably [11].

2.1.2 The monopole interaction

The effective interaction can be divided in a monopole part (H_m), which rules the evolution of the SPE, and a multipole one (H_M), which is related to the development of correlations:

$$H = H_m + H_M . \quad (2.6)$$

H_m can be considered as the mean energy brought to the nucleus by the addition of two interacting nucleons in the orbitals j and j' [3] and it is expressed as

$$V_{jj'}^m = \frac{\sum_J (2J+1) \langle jj'J | V | jj'J \rangle}{\sum_J (2J+1)} , \quad (2.7)$$

where J runs over all the possible couplings of j and j' [23]. The SPEs for a closed shell (ϵ_j^{CS}) can be extracted from the known one of a higher closed shell ($\epsilon_j^{CS'}$) with the relation [24]:

$$\epsilon_j^{CS} = \epsilon_j^{CS'} + \sum_{j'} (2j' + 1 - \delta_{jj'}) V_{jj'}^m . \quad (2.8)$$

The energy values obtained in this way are called *effective single particle energies* (ESPE). This method gives excellent results near closed shells but it fails to reproduce the evolution of the single particle energies from one closed shell to the next one [24]. This deficiency, attributed to a saturation of the monopole interaction in the center of the shell, is solved fitting the monopole matrix elements to the evolution of the experimental SPEs between two closed shell. The phenomenological correction obtained gives very good results in reproducing the SPEs but, on the other hand, it limits SM calculations only to regions with enough experimental data [24].

2.2 Nuclear structure in ^{100}Sn

Experimental data on the nuclear structure of ^{100}Sn are very scarce due to the very low cross section for the production of this nucleus, as commented in the Introduction (the available information are reported in Tab. 2.1). Only the relative position between the two neutron single-particle states immediately above the $N=50$ gap is known from the measured transition between the $g_{7/2}$ and $d_{5/2}$ orbitals in ^{101}Sn [25]. All the other single particle energy states that build the spectrum of ^{100}Sn in Fig. 2.1 are extrapolated with the empirical method described in Sec. 2.1.1 from the better known ^{90}Zr (CS) and its $\text{CS} \pm 1$ (^{89}Zr , ^{91}Zr , ^{91}Nb), $\text{CS} \pm 2$ (^{92}Mo) and $\text{CS} + 1 \pm 1$ (^{90}Nb , ^{92}Nb) neighbors. Because of the saturation of the monopole interaction in the middle of the shell, an effective shell model fit for the full $Z=N=28,50$ shell is used to adjust the position of the $\pi\nu$ ($g_{9/2}$, $p_{3/2}$) levels relative to the $\pi\nu$ ($g_{9/2}$, $p_{1/2}$) orbitals [19, 26, 27].

TABLE 2.1. Information on ^{100}Sn from Refs. [28, 29].

Lifetime (s)	1.16(20)
mass excess (keV)	-57280(300)
binding energy/A (keV)	8253(3)
β^+ decay energy (keV)	7030(240)
n separation energy (keV)	17410(590)
p separation energy (keV)	3200(360)
Q_α (keV)	-4140

In absence of sufficient experimental data, predictions for ^{100}Sn are compared to the case of the analogue ^{56}Ni , a self-conjugated doubly magic ($N=Z=28$) nucleus which is easier to observe experimentally. As ^{56}Ni lies one full major shell lower than ^{100}Sn , the level schemes differ only by one angular momentum unit (except for the additional $2s_{1/2}$ in the ^{100}Sn). Moreover, both nuclei are characterized by a spin-orbit (SO) open shell (i.e. orbitals with the same angular momentum but different spin orientation are lying in two different major shells), as it can be noticed looking at the position of $f_{5/2}$ and $f_{7/2}$ in ^{56}Ni and of $g_{7/2}$ and $g_{9/2}$ in ^{100}Sn . This condition entails that spin-flip transitions, together with the E2 $\Delta j = \Delta l = 2$ stretched transitions (between $f_{7/2}$ and $p_{3/2}$ in ^{56}Ni and between $g_{9/2}$ and $d_{5/2}$ in ^{100}Sn) can occur across the shell gap, reducing in this way the rigidity of the core. In ^{56}Ni , indeed, despite the presence of a large shell gap (6.4 MeV), an enhanced transition probability from the core is observed. Comparison with LSSM calculations established that only 50-60% of the ground state is composed by the closed shell configuration [30]. It is therefore possible to speak about a *softness* of the $N=Z=28$ shell closure. Consequently, due to the strong resemblance of the SPE structures, the possibility of a large transition probability across the gap, and therefore of a weakness of the shell closure, arises also for ^{100}Sn . For ^{100}Sn , in addition, stretched E3 transitions between $p_{1/2}$ and $g_{7/2}$ are plausible. On the other hand, indirect evidences suggest a robust shell closure in ^{100}Sn , at variance with what is observed in ^{56}Ni . The measured enhanced energy in the α decay in the $^{109}\text{Xe} \rightarrow ^{105}\text{Te} \rightarrow ^{101}\text{Sn}$ [7] and $^{110}\text{Xe} \rightarrow ^{106}\text{Te} \rightarrow ^{102}\text{Sn}$ chains [31], is explained as an effect of the $N=Z=50$ shell closure. Furthermore, while the GT decay strength in the ^{56}Ni decay is widely fragmented [32], in ^{100}Sn mainly one state is populated: most of the decay strength is concentrated in the $0^+ \rightarrow 1^+$ ($\pi g_{9/2}^{-1}, \nu g_{7/2}$) transition. This result, besides giving indications of a subtle difference in the single particle energy structure between the two nuclei, infers the purity of the ground state for ^{100}Sn , proving a robust

$N=Z=50$ shell closure [8]. Moreover, this scenario is in agreement with what is observed in the case of the heavier doubly-magic ^{132}Sn and ^{208}Pb , where large shell gaps ($\approx 4,5$ MeV [33, 34]) are linked to robust shell closures [35, 36]. Whether ^{100}Sn resembles the behavior of these heavier nuclei or the lighter ^{56}Ni , is to be experimentally determined.

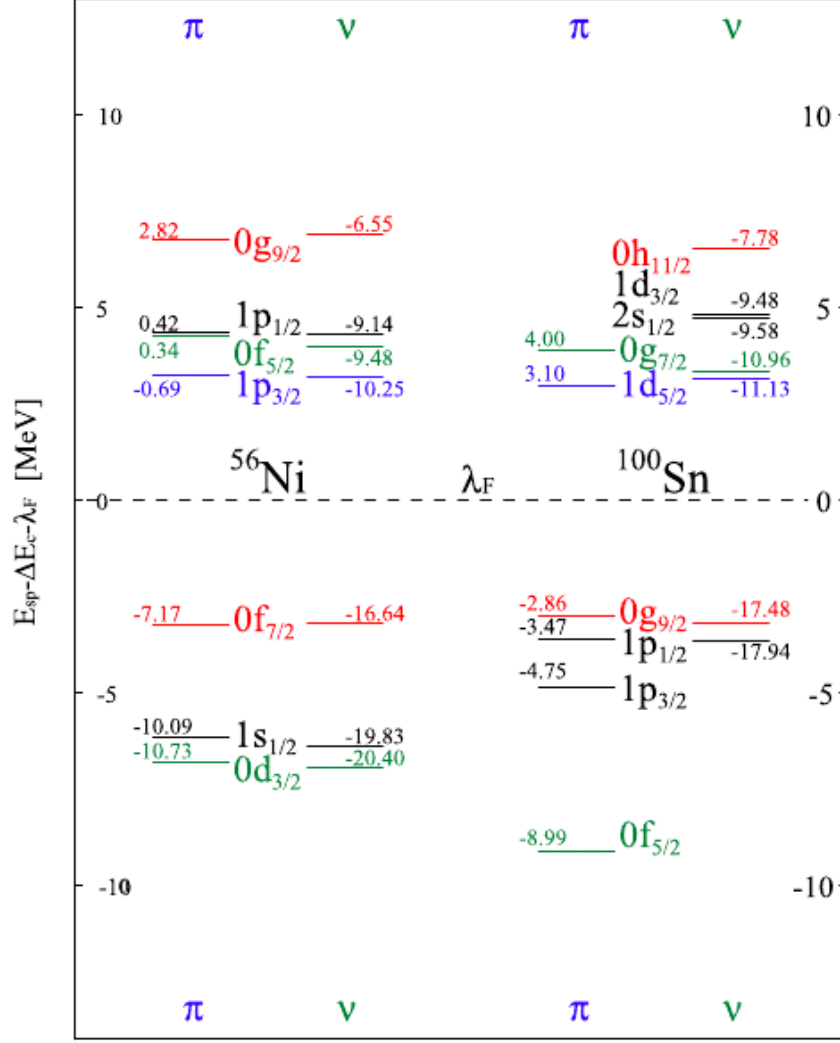


FIGURE 2.1. Single-particle energy spectra in ^{56}Ni and ^{100}Sn [30]. The levels are shown relative to the middle of the gap (λ_f) which accounts for Coulomb shift (ΔE_c) between proton and neutrons. Experimental values for ^{56}Ni are compared to updated extrapolations for ^{100}Sn [19].

2.3 The $B(E2)$ values in the tin isotopic chain

In order to investigate the role of the core polarization for E2 transitions, the $B(E2)$ value is a sensitive tool as it provides direct information on the wave functions of the states connected by these transitions (see Eq. 1.1). The measurement of the $B(E2)$ value in ^{100}Sn is not possible at the present facilities but, in the past years, many experiments investigated the experimentally reachable Sn isotopes in order to observe the trend along the tin chain toward ^{100}Sn . The tin isotopes are forming the longest chain of semi-magic nuclei ($Z=50$) and they are therefore particularly suitable for systematic studies. Moreover, the energy values of the first 2^+ states are almost constant along the whole chain, in line with predictions of the generalized seniority scheme [37]. Following the same model, the reduced transition probabilities for the $2^+ \rightarrow 0^+$ transition was therefore expected to form a parabola, symmetric with respect to the middle of the shell.

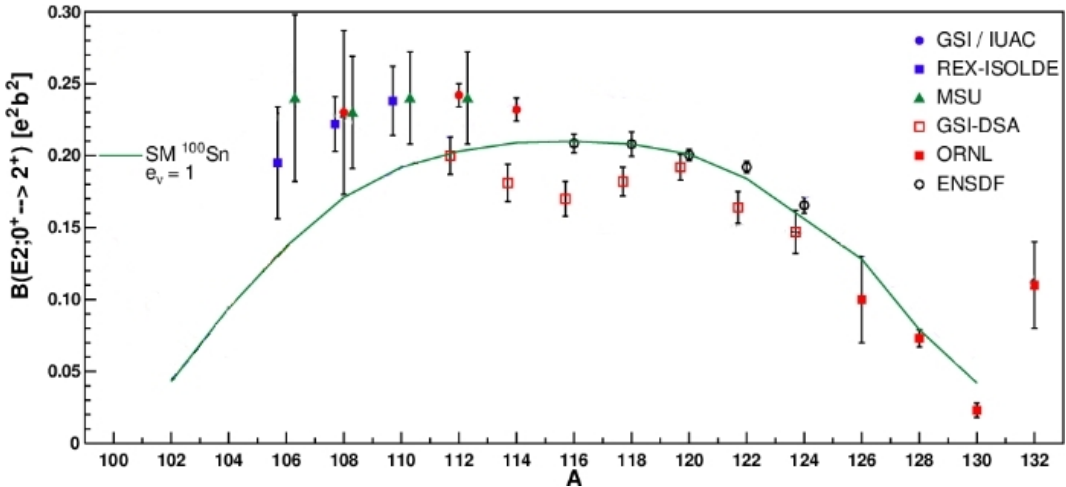


FIGURE 2.2. Experimental $B(E2)$ values of the even-mass Sn isotopes, compared to SM predictions. The data were measured at REX-ISOLDE [38, 39], MSU [40], IUAC [41], GSI [42–44], ORNL [45, 46].

The experimental results and the adopted $B(E2)$ values for the Sn isotopes shown in Fig. 2.2 are listed in Tab. 2.2. In the mid-shell, the results from lifetime measurements performed in GSI with the Doppler Shifted Attenuation (DSA) method (red empty squares) deviate from the adopted values (black circles) and the previous results for $^{112,114}\text{Sn}$ obtained with the Coulomb excitation technique. In particular, a lower collectivity in the middle of the neutron shell, with a shallow minimum at $N=66$, can be observed [44]. This behavior can be explained as a consequence of the filling of

the $s_{1/2}$ neutron orbit: as this orbit can easily contribute to the first 2^+ state only coupling to the $d_{3/2}$, a reduction of the collectivity of this state can be expected [44]. The validity of these results, however, has been called into question by newer values, not yet published but presented in Ref. [47], which confirmed the previously measured values.

The adopted values for the neutron-reach isotopes are in a good agreement with the behavior predicted by the generalized seniority scheme. Nevertheless, a sudden increase from ^{116}Sn to ^{114}Sn and an almost constant trend down to ^{106}Sn , that deviates from the SM predictions, are clearly observed. This situation can be interpreted as a higher than expected quadrupole collectivity that persists toward ^{100}Sn and thus as a weak $N=Z=50$ shell closure, in analogy with the case of ^{56}Ni . In support of this hypothesis, a similar asymmetry in the trend of $B(E2)$ values toward the light doubly magic nucleus is observed also for the light Ni isotopes [30]. However, the large uncertainties on the values for the unstable $^{106-110}\text{Sn}$ hamper the derivation of an unequivocal conclusion for the light Sn region. The measurements on these isotopes reported in Fig. 2.2 have been performed at two different facilities, at the REX-ISOLDE facility [48] and at the NSCL (MSU) [49] employing the safe Coulomb excitation and the intermediate-energy Coulomb excitation technique, respectively. It can be noticed that the experiments at the REX-ISOLDE facility have visibly smaller error and that the $B(E2)$ obtained for ^{106}Sn is significantly lower than the one obtained at NSCL, indicating a reduction with respect to the constant trend observed in $^{108-114}\text{Sn}$ [39]. All the values are anyway in disagreement with the theoretical predictions and many effects have been considered to explain this discrepancy. In particular, observing that the inclusion of excitations from the $Z=50$ core in the valence space gives a significant increase of the predicted values [42], it is assumed that most of the missing E2 transition strength is due to proton core excitations. Moreover, considering the tensor interaction acting between $j = l \pm 1$ orbitals [50], protons from the $0g_{9/2}$ orbital are less bound as less neutrons occupy the $0g_{7/2}$ orbital, i.e. in light tin isotopes, and can more easily contribute to E2 excitations. However, more precise results are needed to determine to which extent the predicted values in $^{106-110}\text{Sn}$ deviate from the experimental data and to give better constraints to the models. Likewise, experiments in lighter nuclei would shed a light on the behavior of the $B(E2)$ values approaching ^{100}Sn .

TABLE 2.2. B(E2) values of the Sn isotopes shown in Fig. 2.2.

A	B(E2; $0^+ \rightarrow 2^+$) ($e^2 b^2$)
106	0.195(39)
	0.240(58)
108	0.222(19)
	0.230(39)
	0.230(57)
110	0.220(22)
	0.238(24)
112	0.240(14)
	0.242(8)
	0.200(12)
114	0.24(5)
	0.183(12)
116	0.209(6)
	0.170(10)
118	0.209(8)
	0.183(9)
120	0.2020(40)
	0.191(10)
122	0.1920(40)
	0.164(10)
124	0.148(15)
	0.1660(40)
126	0.127(8)
128	0.080(5)
130	0.023(5)
132	0.11(3)

Chapter 3

The PreSPEC fast-beam setup

PreSPEC nuclear structure experiments at GSI are performed with relativistic beams (at energies up to 1 GeV/u for Uranium) delivered by the UNIversal Linear ACcelerator system (UNILAC) coupled with the synchrotron SIS-18. Radioactive ion beams are obtained from the stable ones via fragmentation or in-flight fission on a target positioned at the entrance of the FRagment Separator (FRS) [51]. The latter provides separation, tracking and identification of the secondary beams and serves to focus the isotopes of interest on a secondary target. The high energy of the secondary beams (in the range of 100-400 MeV/A at the secondary target) allows for a clear separation and an event-by-event identification of very rare reaction products, not similarly accessible in other facilities, allowing exclusive in-beam γ -ray spectroscopy. Studies of low lying collective states via relativistic Coulomb excitation as well as of higher spin states via fragmentation reactions can be performed then at the secondary target to obtain new insights in the nuclear structure of radioactive nuclei.

Within the Rare Isotope INvestigations at GSI (RISING) project [52], a collaborative European experiment run from 2003 to 2009, nuclear structure studies on unstable isotopes were performed combining the FRS and high-resolution Ge-detectors array. PreSPEC is the successor of RISING and it is the preparatory phase of the future High-resolution In-flight SPECtroscopy (HISPEC) project. The latter is a part of FAIR (Facility for Antiproton and Ion Research), the facility of new generation at the moment under construction at the GSI site. During the PreSPEC campaign some of the detectors present in the FRS and their electronics have been replaced in order to be able to accept higher ion rates. At present, 10^7 pps (particles per second) at the intermediate focal plane of FRS and 10^5 pps at the final one are the detection counting rates limits. Moreover, in view of HISPEC, the first prototype of LYCCA (Lund York

Cologne Calorimeter) [53] has been tested and used. LYCCA is a flexible array of detectors which provides event-by-event information on the position, the charge and the mass of the ejectiles after the secondary target. The most important new feature that distinguish LYCCA from CATE (CAlorimeter TElescope), the detector used for second reaction product identification at RISING, is the possibility to discriminate the masses of the ions via ToF (time of flight) measurements.

During the fast-beam RISING campaign (2003-2005) and the first part of the PreSPEC phase (2010-2011), the γ -rays emitted in reactions at the secondary target were detected with 15 detectors of the EUROBALL cluster array, placed in three rings at forward angles. In the second part of the PreSPEC phase (2012-2014), 16 to 22 crystals of AGATA (Advance GAMMA Tracking Array), a new generation of position-sensitive high-purity germanium, were employed in a much more compact geometry [54].

As complementary γ -ray detectors, the PreSPEC setup includes the HECTOR array, composed of eight large volume BaF_2 scintillators, and from 2012 the HECTOR+ array, composed of eight large volume LaBr_3 scintillators [55]. HECTOR and HECTOR + were positioned at 35 cm from the secondary target, at a polar angle of 90° with respect to the beam direction or at backward angles. These detectors have been included in the setup because of their good γ -ray efficiency also at very high energies (2% at 1 MeV and 1% at 10 MeV) and excellent time resolution.

3.1 Radioactive beams at FRS

The FRS is a magnetic spectrometer designed to separate the unstable isotopes produced at relativistic energies at GSI. The following description of the device focuses mainly on the aspects that are relevant for spectroscopy experiments. A full description can be found in [51].

3.1.1 Production mechanism

At the FRS, exotic beams are produced via fragmentation reaction or in-flight fission of high energy stable beams extracted from SIS-18. The reaction is chosen according to the area of interest in the nuclear chart. Medium-mass neutron-rich nuclei can be best produced via fission of relativistic heavy primary beams (^{238}U) on a ^9Be or ^{208}Pb target. Proton-rich nuclei as well as light and heavy neutron-rich nuclei are produced via fragmentation of the primary beam, usually on a ^9Be target.

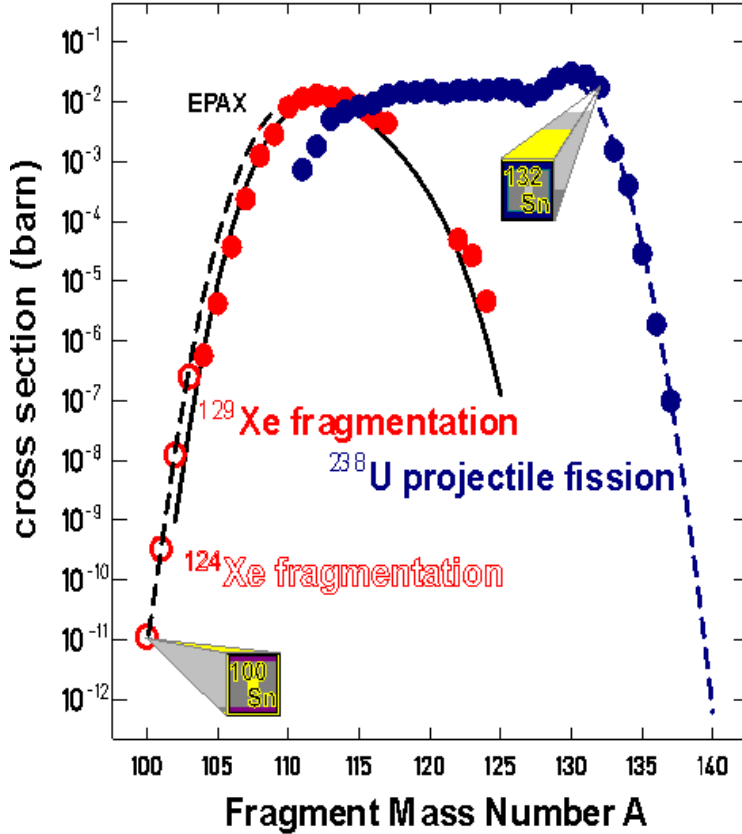


FIGURE 3.1. Cross section for the production of Sn isotopes via fragmentation of ^{129}Xe and ^{124}Xe on a ^{27}Al target, and via fission of ^{238}U on a ^{208}Pb target [56].

In Fig. 3.1 the production cross section for Sn isotopes via fragmentation and projectile fission are presented. In this case, the products of the two mentioned type of reactions are covering different ranges of mass number.

Dependently on the reaction used, the transmission of fragments through the FRS is considerably different. In a fragmentation reaction, the momentum of the projectile is transferred to the products, that are therefore maintaining the same direction. Hence, the transmission of the isotopes can reach values of about 50% for spectroscopy measurements. In the case of fission, the energy released in the reaction causes an extra momentum vector transfer to the two products and influences their direction. The transmission is therefore limited to a small fraction of the total yield.

3.1.2 Separation method

In the primary target (in the following also called production target) the isotope of interest is unavoidably produced together with often strongly populated contaminants. The separation of these isotopes in the FRS is realized via the so called $B\rho$ - ΔE - $B\rho$ method.

One of the basic principles exploited by this method is the proportionality relationship between the magnetic rigidity ($B\rho$) of the nucleus and its *mass over charge ratio* (A/q). It can be deduced considering the Lorentz force acting on a particle with velocity v , mass m and charge q moving in a homogeneous magnetic field B

$$\vec{F}_{Lorentz} = q \cdot \vec{v} \times \vec{B} \quad (3.1)$$

and taking into account that in FRS \vec{v} and \vec{B} are perpendicular to each other and therefore the Lorentz force acts like a centripetal force:

$$|\vec{F}_{Lorentz}| = \frac{mv^2}{\rho} , \quad (3.2)$$

with ρ being the bending radius of the trajectory. The combination of these last two expressions gives

$$B\rho = \frac{p}{q} , \quad (3.3)$$

where $p = mv$ is the momentum of the ion. The magnetic rigidity $B\rho$ is therefore specific for an ion with a certain mass over charge ratio and velocity. At relativistic energies the ion is fully stripped, i.e. $q=Ze$, and the momentum transforms as $p = \beta\gamma Auc$ (being $\beta = v/c$, c the speed of light, γ the Lorentz factor and u the atomic mass unit). The formula of the magnetic rigidity results

$$B\rho = \beta\gamma c \frac{Au}{Ze} , \quad (3.4)$$

with explicit proportional relation with the mass over charge ratio.

The building blocks of the FRS are four large magnetic dipoles and the respective four focal planes. The bending radius of the dipoles is kept fixed at $\rho=11.25$ m and

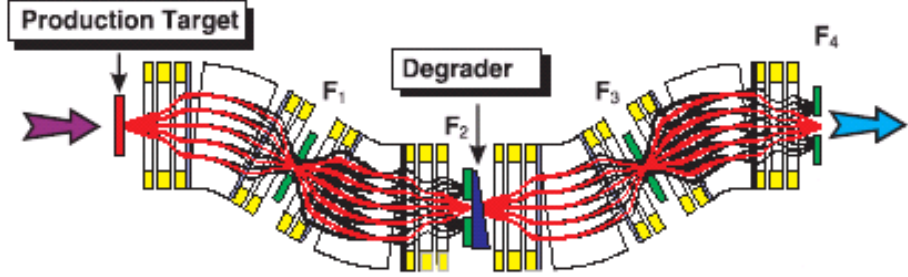


FIGURE 3.2. Schematic drawing of the FRS. The trajectory of ions with a specific A/q and with the achromatic setting of FRS are drawn in red. The slits are represented in green and the focal planes are indicated by the letter F and consecutive numbers.

the B fields are chosen such that ions with a certain magnetic rigidity have a central trajectory. At the intermediate focal plane, i.e. after the first two dipoles, the ions with a specific value of A/q are distributed on the x axis (horizontal and perpendicular to the beam direction) according to their momentum. To minimize the momentum spread, a wedge-shaped degrader is inserted there to let nuclei with different energies pass through different thickness of matter. In this way, the wanted species can be further separated by $B\rho$ and focused in space to the final focal plane by the last two dipoles. The selection of the ions is performed also via slits inserted perpendicular to the beam direction. They are present at each focal plane and their position can be adjusted in order to block the passage of specific parts of the secondary beam which cannot be separated out by other means. Multiple sets of quadrupole magnets are present to provide horizontal and vertical focusing of the ions at each focal plane. The FRS is equipped also with sextupole magnets and steerers for higher order corrections.

3.1.3 FRS detectors

As described in the previous paragraph, the secondary beam passing through the FRS is composed of a cocktail of isotopes and the one of interest can represent only a small fraction of all the ions. Hence, it is fundamental to identify the mass and the proton number of the nuclei arriving to the last focal point in order to be able to select them.

The Z of the ions is obtained from energy loss measurements in the MUltiple Sampling Ionization Chamber (MUSIC). The main part of this detector is a gas cell filled of pure CF_4 gas at room temperature and pressure. The cloud of electrons created by the ion passing through the chamber is collected by eight anodes and is proportional to the

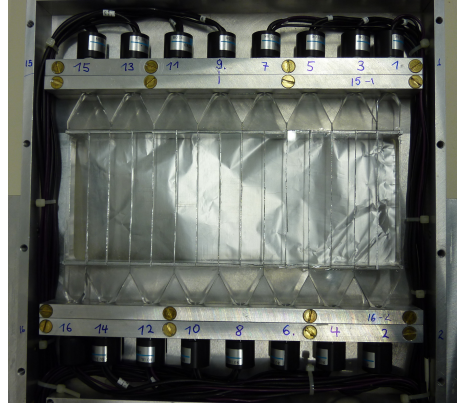


FIGURE 3.3. Photograph of the Finger detector in use from 2010 to 2012. The area of the detector was divided in 15 strips to allow good detection efficiency at high rates [58].

energy loss by the ion in the gas. The latter quantity is related to the proton number Z of the ion via the expression

$$-\frac{dE}{dx} = Z^2 f(\beta) \quad (3.5)$$

that can be deduced from the Bethe-Bloch formula [57]. The term $f(\beta)$ is a function of the velocity obtained as explained in Par. 4.2.1.

The A/q value is extracted from ToF measurements, performed with plastic scintillators (BC420) positioned at the intermediate and at the final focal plane.

A new ToF segmented plastic scintillator, called Finger, was added at the intermediate focal plane to sustain high ion counting rates. The prototype in use from 2010 to 2012 was made of 15 strips (Bicron BC-420, 14 mm width) and read out by 16 fast PMTs (see a photograph of the detector in Fig. 3.3). From 2014 a new version of the detector, made of 52 strips (4.5 mm width) and read out by 54 PMTs, replaced the prototype and allowed rates higher than $3 \cdot 10^6 \text{ s}^{-1}$. As shown in the plots of Fig. 3.4, at high beam intensity the standard scintillator failed to separate the A/q value of different ion species, while with the Finger detector good efficiency and A/q resolution are obtained [58].

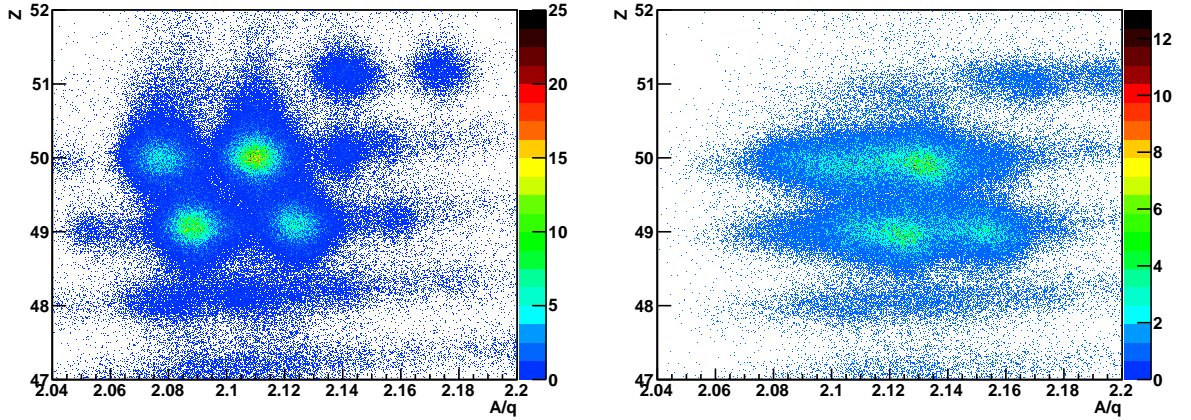


FIGURE 3.4. Identification plots of the ions in FRS with high ion rates (10^5 s^{-1}): the A/q value, deduced from ToF measurements, is plotted versus the proton number Z , obtained from the MUSIC. In the figure on the left the ToF was obtained using the Finger detector, while in the figure on the right a standard scintillator was used at the intermediate focal plane. Sufficient A/q resolution of the Finger detector in contrast to the standard scintillator is evident from this comparison.

Time Projection Chambers (TPCs) were used as position sensitive detectors. Two of them were present at the intermediate focal plane and two at the final one to reconstruct the trajectory of the particle.

More information on the detectors used at FRS can be found in the Ref. [59].

3.2 Isotope identification after the secondary reaction: LYCCA

For performing fast-beam experiments it is required to identify and to track the path of the ions after the secondary target in order to reconstruct the reaction that has occurred in the secondary target. LYCCA has been designed to provide unique identification and tracking of nuclear reaction products by their mass A and charge Z through event-by-event time-of-flight, energy loss and total energy measurements. During the PreSPEC-EUROBALL campaign the first prototype LYCCA-0 has been used. A schematic drawing of the setup is shown in Fig. 3.5. The identification of the proton number Z of the nucleus is obtained from the energy loss (ΔE) and residual energy (E) measurements via the well established $\Delta E-E$ method (described in Chapter 4).

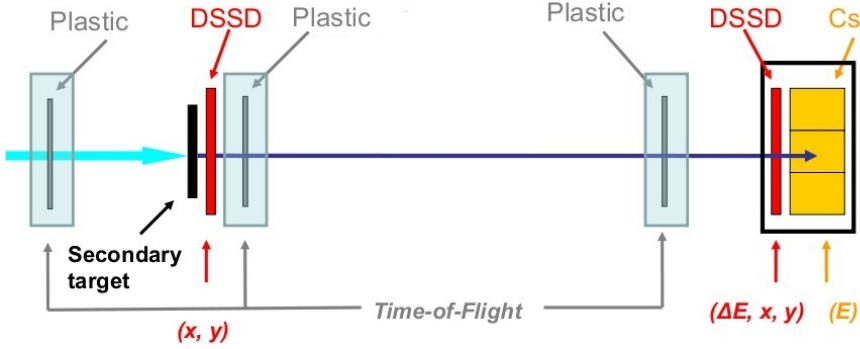


FIGURE 3.5. Schematic drawing of the LYCCA setup. For more details on the use of each detector see the text.

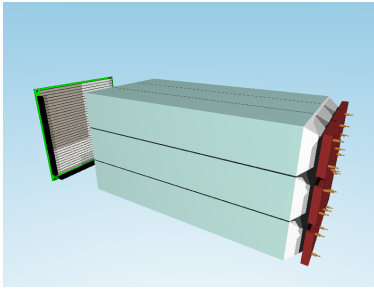


FIGURE 3.6. Representation of one module of the LYCCA ΔE - E wall telescope. The DSSSD detector, divided in 32 strips, is placed in front of an array of 9 (3×3) CsI(Tl) scintillators.

This information is provided by the LYCCA ΔE - E wall telescope, divided in 4×3 modules and positioned about 3.1 m downstream from the target. Each module of the telescope is composed of a Double Sided Silicon Strip Detector (DSSSD), which provides the energy loss signal, backed by 3×3 crystals of Caesium Iodide scintillators (CsI(Tl)), providing the residual energy information (see Fig. 3.6). Each DSSSD, made of silicon wafers $303 \mu\text{m}$ thick, is square shaped and has an active area of 58.5 mm^2 . Each of its fronts, p-side and n-side, is subdivided into 32 strips in orthogonal direction, providing the x and y position. The telescope array covers an angle relative to the beam direction (in the following called θ) of about $\pm 3.0^\circ$, the relevant ones for Coulomb excitation experiments at 100 MeV [60].

To achieve the mass separation (up to $A \simeq 100$), a high-precision time-of-flight (ToF) system was integrated. It is composed by a ToF Start detector, placed before the secondary target, and a ToF Stop detector, positioned before the LYCCA wall telescope. They consist of large-area plastic-scintillator detectors: a circular membrane of Saint-Gobain BC-420, with 2 mm thickness and 27 cm diameter, read out by 32 photo

multipliers tube (PMTs). The in-beam test of this equipment showed an intrinsic timing resolution of $\Delta t \leq 50$ ps FWHM [61].

Due to the relativistic energy of the beam, the emitted γ -rays are largely affected by the Doppler Shift effect (details will be described in the next section). The position of the ion at the target is therefore needed to perform an accurate Doppler Shift correction. This information is obtained with a DSSSD positioned 1 cm before the target.

3.3 The EUROBALL cluster array and AGATA

Gamma-ray spectroscopy experiments within the PreSPEC project are based on large arrays of High-Purity Germanium (HPGe) detectors. In the first phase of the campaign, from 2010 to 2011, the EUROBALL cluster array has been used, replaced from 2012 by the advanced AGATA setup, with a number of crystals varying between 16 and 22.

The arrangement of the detectors, in both PreSPEC campaigns, took into account the two main relativistic effects occurring when the γ -rays are emitted in-flight, the Lorentz forward boost of the γ -ray intensity distribution and the energy Doppler Shift. The former can be defined as the forward focusing of γ -ray distribution in the laboratory frame. To take advantage of it, both arrays have been positioned at small angles relatively to the beam direction. It is therefore expected that the first ring of crystals, i.e. the one at smallest θ angles, registers a higher number of counts. The latter refers to the difference between the value of γ -ray energy seen by the detectors and the one in the reference frame of the source. This difference is related to the velocity of the source and the angle of emission of the radiation. The accuracy in the correction of the energy shift therefore increases when the solid angle coverage of the single detector unit is reduced (see Fig. 3.7), i.e. increasing the distance of the detector from the target or reducing the detector size.

3.3.1 The EUROBALL cluster array

The EUROBALL cluster array consisted of 105 crystals (15 clusters) of HPGe detectors. A common cryostat contained 7 encapsulated crystals, arranged as shown in the inset of Fig. 3.7. The clusters were arranged in three rings, with average angles of 16° ,

33° and 36° and at a distance from the target of ~ 700 mm. A γ -ray energy resolution of $\sim 1.24\%$ (FWHM) was obtained, with photopeak efficiency of 2.81% at $\beta \sim 0.5$ [60].

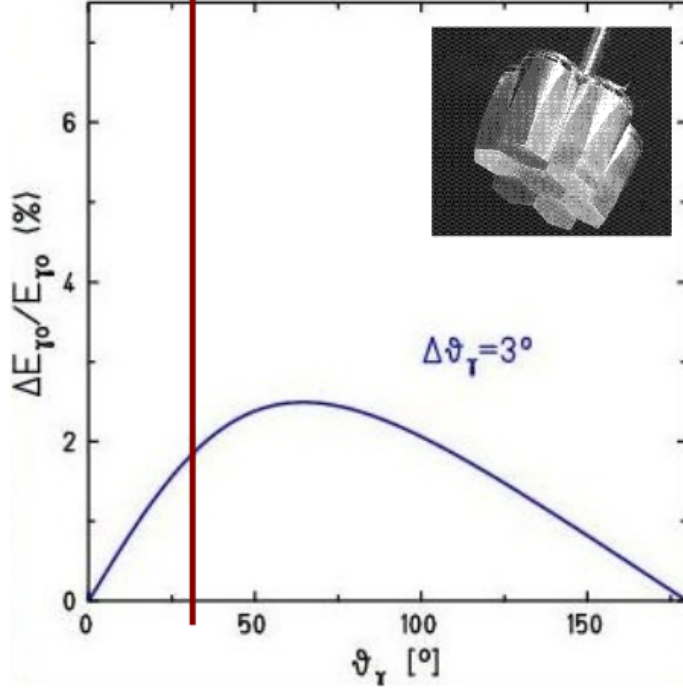


FIGURE 3.7. Doppler broadening of the energy of the γ -rays as a function of the angle of emission, considering the opening angle of $\sim 3^\circ$ of the EUROBALL crystals. The red line indicates approximately the largest observation angle of the EUROBALL crystals. In the inset a photograph of a cluster detector consisting of seven crystals is shown.

For HPGe detectors, the standard way to process both time and energy information is to use an analog circuit, generally consisting in shaping amplifiers followed by ADCs and TDCs modules. To extract the energy information from the EUROBALL clusters, instead, a fully digital approach has been chosen: the signal out of the pre-amplifiers were immediately digitalized by Digital Gamma Finder (DGF) modules [62]. With a fast algorithm, called Moving Window Deconvolution (MWD) the real effective charge was calculated and the energy deposited by the radiation was obtained. The choice to digitize the signal after the pre-amplifiers allowed to treat pile-up events and to sustain higher rates. On the other hand, the time resolution given by the DGF is lower than the one from the analog electronics. Therefore, an analogue standard TFA - CFD - TDC circuit has been used to extract the time signals.

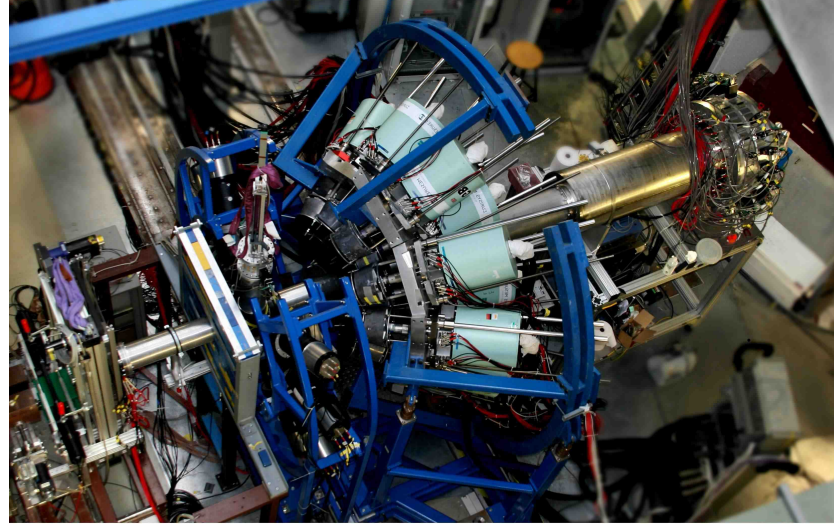


FIGURE 3.8. Photograph of the PreSPEC setup. The beam comes from the lower left side.

3.3.2 AGATA

AGATA is the new generation European γ -ray detector array, based on highly-segmented HPGe detectors (see Fig. 3.9). The measurement and the analysis of the waveforms that arise on a segment during the charge collection enables the identification of position, time and energy of each interaction of the γ -rays within the detector volume. These information allows to reconstruct the path in the crystals, making use of tracking algorithms, and to determine the full energy of the original γ -ray. The result of the application of these advanced techniques is high energy resolution and efficiency [63]. More details about AGATA at GSI can be found on the website [64]. In comparison to the EUROBALL cluster array, the higher granularity allowed to place the crystals much closer to the secondary target, down to 85 mm distance, for higher angular coverage and therefore higher total detection efficiency of AGATA with respect to EUROBALL.

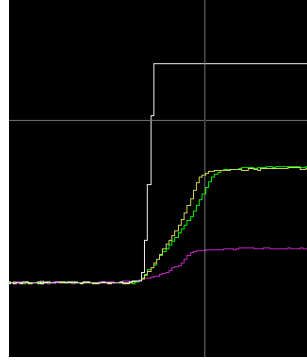


FIGURE 3.10. Short traces from an AGATA crystal, superimposed using different colors. The height of the trace is proportional to the energy deposited by the radiation. The white trace, at variance with the others, shows a saturation of the energy range.

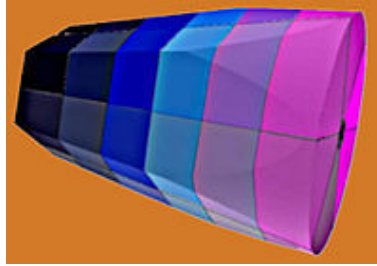


FIGURE 3.9. Drawing of an AGATA crystal. Each crystal is electrically divided in 36 segments, six azimuthal and six axial, plus a central contact, named *core*.

In the AGATA setup, in addition to the digitalization of the energy signals, also the time information is fully digitized. Moreover, the data-acquisition system is able to supply and store, together with the energy and time information, *short traces* of the digitized leading edge of each pulse. These feature is necessary to perform the pulse-shape analysis but it can be also usefull for further analysis purposes. The detailed analysis of not properly processed events can indeed provide an explanation for part of the background and for a possible loss of efficiency. An example of those traces is shown in Fig. 3.10.

3.4 Atomic and nuclear background

In fast beam experiments, a large amount of background radiation affects the γ -ray energy spectra, hampering the association of γ -rays from reactions with a very low cross section. Atomic processes are mainly occurring due to the interaction of the fast beam with the matter at the final focal plane. They can be distinguished as:

- the capture of target electrons by the projectile (radiative electron capture (REC)),
 $\sigma \sim Z_p^2 \cdot Z_t$;
- emission of primary bremsstrahlung (PB) from target electrons scattering off the projectile, $\sigma \sim Z_p^2 \cdot Z_t$;
- emission of secondary electron bremsstrahlung (SEC) from a target electron ejected and then rescattered in the target material, $\sigma \sim Z_p^2 \cdot Z_t^2$;
- emission of K and L X-rays from atoms of the target.

The cross section for the electron capture and bremsstrahlung processes has been indicated with σ and Z_p and Z_t are the proton number of the projectile and the target, respectively. From these relations, it follows that the production of atomic background therefore becomes more dominant using heavy projectiles and targets as it is shown in Fig. 3.11, where the γ -ray energy versus the cross section for production of atomic background is plotted for the case of ^{132}Sn beam on a ^{208}Pb target, considering different beam energies. The atomic background therefore puts a limit on the energy of the secondary beams and a minimum on the γ -ray energy registered for the reaction. In addition, the detection of the prompt bremsstrahlung reduces the detection efficiency. This is true especially for the EUROBALL array, since the electronics cannot process more than one hit per event for each crystal, while with AGATA, due to the segmentation of the crystals, the detection of background is less problematic.

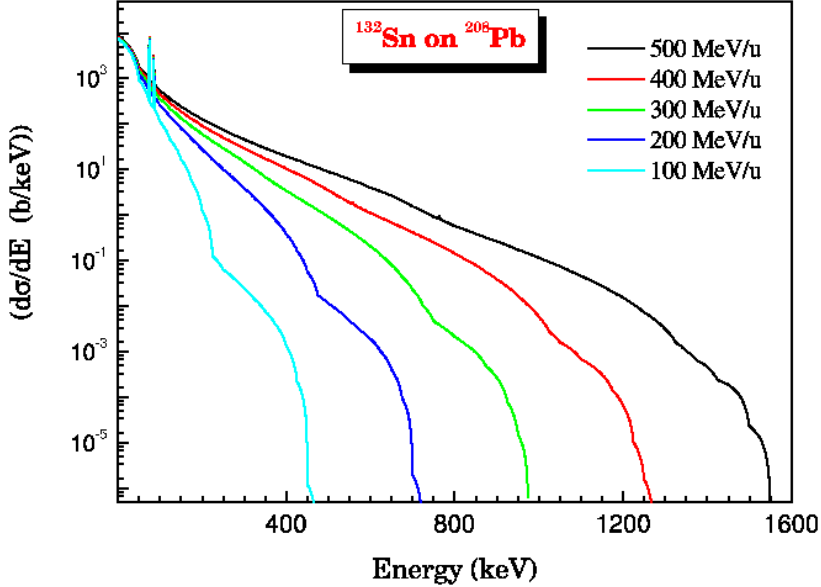


FIGURE 3.11. Angle-integrated cross section as a function of γ -ray energy for the atomic background from ^{132}Sn on a ^{208}Pb target at different beam energies.

In addition to atomic processes, because of the high energy of the beam, nuclear reactions are also contributing to the background. A total γ -ray energy spectrum from a PreSPEC experiment is presented in Fig. 3.12, where the typical smooth and high background profile can be noticed. The γ -ray peaks on top of it are related to unwanted nuclear reactions of the beam along the FRS or at the production target. The following background sources can contribute [65]:

- inelastic scattering of fast neutrons on Aluminium ($^{27}\text{Al}(\text{n},\text{n}')$), of which the beam pipe and the reaction chamber are made of;
- quasi-free proton scattering ($^{27}\text{Al}(\text{p},2\text{p})^{26}\text{Mg}$);
- activation of the surrounding materials and of the germanium crystals ($\text{Ge}(\text{n},\text{n}')$) from scattering with fast neutrons.

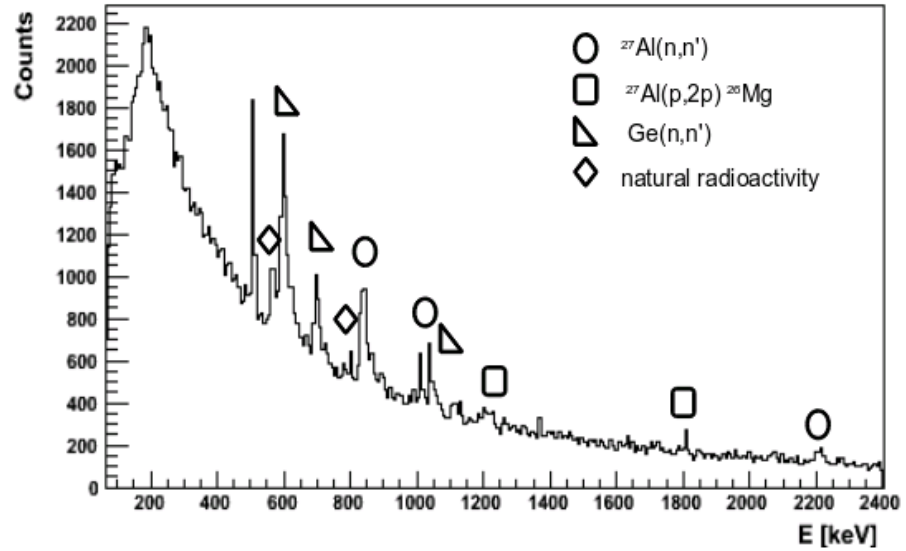


FIGURE 3.12. γ -ray energy spectrum of a EUROBALL cluster from an in-beam experiment at PreSPEC. The peaks on top of the smooth background are coming from nuclear reactions of the beam impinging on the surrounding material.

A detailed analysis of the components of the nuclear background and the impact on the analysis of the data is presented in Chapter 5.

Chapter 4

Experimental details and data analysis of the B(E2) value measurement in ^{104}Sn

Over the past few years, a series of experiments have been performed on neutron-deficient Sn isotopes in order to investigate the evolution of nuclear structure in proximity of the doubly magic nucleus ^{100}Sn . The data showed excessive experimental B(E2) strength compared to shell model calculations below neutron number $N=64$, not excluding a constant or even increasing collectivity below ^{106}Sn and bringing into question the $N=Z=50$ shell closure (as described in Chapter 2). Hence, the measurement of the B(E2) value in the next even-even isotope towards ^{100}Sn , i. e. ^{104}Sn , was a crucial step to verify the robustness of the shell closure in ^{100}Sn . Moreover, it is unclear at present whether the deviations between shell model calculations and experiments are due to truncation imposed by computational limits or due to deficiencies in the effective interactions. However, in the case of ^{104}Sn , shell model calculations without significant truncation of the valence space are possible due the smaller and more tractable model space. The comparison between the predicted value and the experimental result for ^{104}Sn is therefore an important test of the validity of Large Scale Shell Model (LSSM) calculations.

The B(E2) value in ^{104}Sn has been measured for the first time in GSI in 2010 with a Coulomb excitation experiment performed within the PreSPEC fast-beam campaign. ^{104}Sn was produced via nuclear fragmentation of a ^{124}Xe beam at 793 MeV/u impinging on a 4 g/cm^2 thick ^9Be target. To separate the products, two degraders of 2.0

g/cm^2 and $2.4 \text{ g}/\text{cm}^2$ thickness, at the first and at the intermediate focal plane of the FRS were used, respectively. At the final focal plane the isotopes were focused onto a $386 \text{ mg}/\text{cm}^2$ thick ^{197}Au target, in order to use the Coulomb excitation technique. The population of the first excited 2^+ state and the measurement of its decay strength for the very neutron-deficient Sn isotopes cannot be achieved via fusion-evaporation reaction, as done for heavier isotopes, due to the presence of low lying 6^+ isomers. The feeding of these long living states (life time $>2 \text{ ns}$) would, indeed, hamper the observation of the decay of the short living ($<\text{ns}$) first 2^+ state. Coulomb excitation, instead, populates the first excited state directly from the ground state, avoiding the problem of feeding higher states, and it is therefore the method of choice. To be able to neglect experimental details, as particle- γ angular correlations, feeding contributions from higher-lying states and possible systematic errors, the $B(E2)$ value of ^{104}Sn has been deduced relatively to the one of the stable ^{112}Sn , measured in very similar experimental conditions. It was produced from ^{124}Xe primary beam at $700 \text{ MeV}/u$ and it was separated via a $3 \text{ g}/\text{cm}^2$ thick degrader at the intermediate focal plane. As ^{112}Sn is the lightest stable Sn isotope, it guarantees minimum structural changes compared to ^{104}Sn and therefore is the best possible choice of the calibration measurement.

As described in the previous chapter, a fast beam experiment on such a rare isotope is very challenging due to the small production cross section and the large bremsstrahlung background, caused by the high energy beam, which by far dominates the gamma-ray spectra. For the full identification of the gamma-rays originating from the 2^+ state in ^{104}Sn , the PreSPEC experimental setup, which provided with identification and tracking detectors over 1000 parameters, has been used. The standard FRS detectors were employed, except for the scintillator at the intermediate focal plane that was replaced in the analysis with the Finger detector, as mentioned in Par. 3.1.3. The isotopes after the target were detected by LYCCA-0, the first implementation of the LYCCA setup. To detect the γ -rays, the full EUROBALL cluster array was employed. Nevertheless, seven crystals have been excluded in the data analysis because of missing or inadequate distribution of counts in their TDC time.

4.1 Relativistic Coulomb excitation

Coulomb excitation is an inelastic scattering process that involves solely electromagnetic interaction between the nuclei. At relativistic energies it can be considered as

a one-step process that populates a low spin state of a nucleus or excites the Giant Dipole Resonance (GDR), according to the energy of the projectile. In the case of even-even nuclei, the production of the first 2^+ state dominates at beam energies below 100 MeV/u, while the GDR occurs mainly above it (see Fig. 4.1) [60].

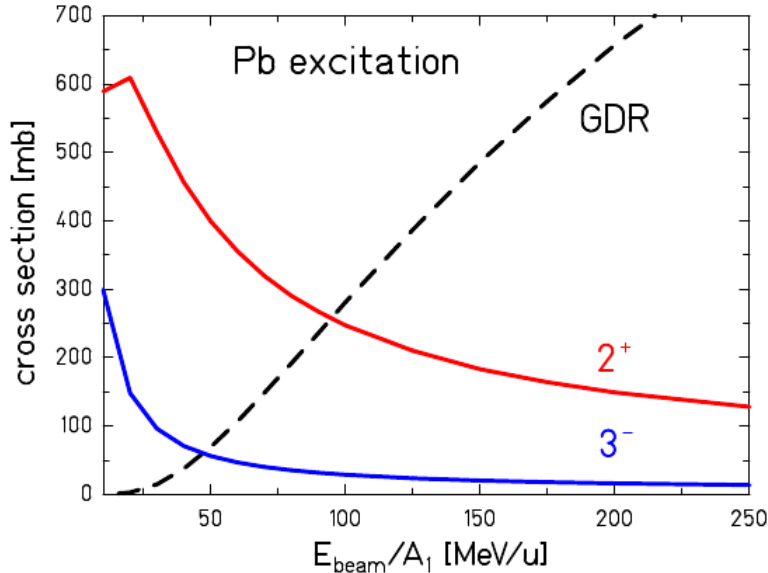


FIGURE 4.1. Beam energy versus Coulomb excitation cross sections for the first excited 2^+ and 3^- states and the giant dipole resonance (GDR), for a ^{136}Xe beam incident on a Pb target. A minimum impact parameter of 16 fm is assumed in the calculation [60].

One of the principal advantages of using the Coulomb excitation technique at relativistic energies is the possibility to use thick scattering targets, which can compensate for low production cross section facilitating experiments on rare isotopes. On the other hand, beam energies above the Coulomb barrier allow nuclear reactions to occur and contribute to the radiation yield. In order to exclude these reactions and have pure Coulomb interaction, the distance of closest approach between two ions has to exceed the sum of their radii plus several fm: at beam energies as in the experiment here described, a *safe* distance has been calculated to correspond to about 5 fm between the surfaces of the two nuclei [60] (see Fig. 4.2), which corresponds to scattering angles of the ions of $\pm 3^\circ$.

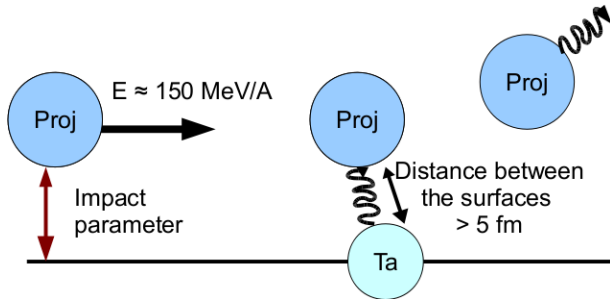


FIGURE 4.2. Schematic drawing of the Coulomb excitation reaction.

4.2 Analysis of the data

Performing in-beam spectroscopy experiments with high energy radioactive beams, the peak associated to the transition of interest cannot be observed without a detailed and tedious selection of the data. In the analysis of the data presented here, precise conditions on the information given by each detector of the setup have been applied in an iterative way, until the peak associated to the $2^+ \rightarrow 0^+$ transition in the γ -ray energy spectra of both nuclei has been observed and the peak-to-background ratio optimized. In the following paragraphs, the calibration procedures performed on the FRS detectors before the analysis on the γ -ray spectra are described. Afterwards, the techniques used to perform the principal selections of the data are also presented. Due to the scarce statistics in the γ -ray energy spectra produced from the data on ^{104}Sn , the selections explained in Par. 4.2.6 and 4.2.7 have been determined using the ^{112}Sn data. The final Doppler corrected γ -ray energy spectra have been obtained applying identical gating conditions to both sets of data.

4.2.1 Calibration of the MUSIC

The energy loss of an ion passing through a material, as shown in the equation (3.5), depends on the ion's atomic number Z and velocity. It is therefore needed to calibrate the response of the MUSIC detectors in a range of velocities that includes the one expected for the fragments during the $B(E2)$ measurement. Different values of β of the primary beam, that is similar to the one of the fragments, were obtained inserting matter of different thickness in the FRS. These values of β were then plotted versus the corresponding energy loss registered in the MUSIC, as shown in Fig. 4.3, and the data points were fitted with a second order polynomial function:

$$\Delta E = a_0 + a_1\beta + a_2\beta^2 , \quad (4.1)$$

The terms a_0 , a_1 and a_2 are the coefficients of the polynomial.

Hence, using the relation (3.5) and assuming that the ions are fully stripped ($q=Z$), the proton number of the fragments (Z_f) can be deduced from the known proton number of the primary beam (Z_p) with the relation

$$Z_f = Z_p \sqrt{\frac{\Delta E}{a_0 + a_1\beta + a_2\beta^2}} . \quad (4.2)$$

The Z values obtained after the calibration of the music MUSIC using the ^{104}Sn experimental data are shown in Fig. 4.4.

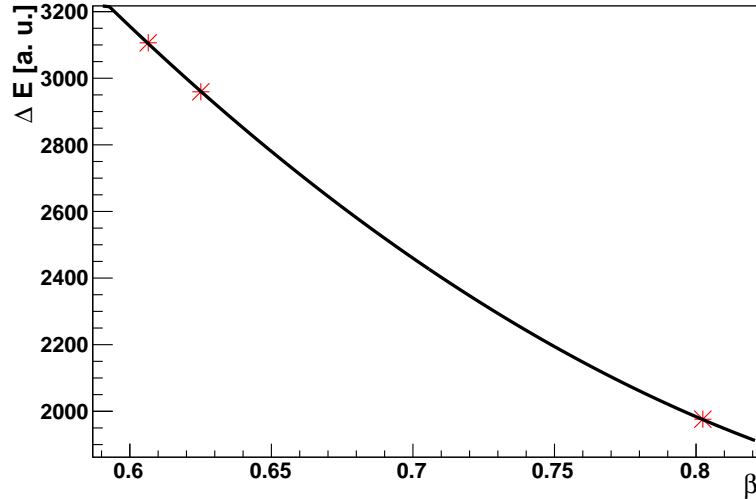


FIGURE 4.3. β values of the Xe beam versus the energy loss in the MUSIC. The data are fitted with a polynomial function of second order.

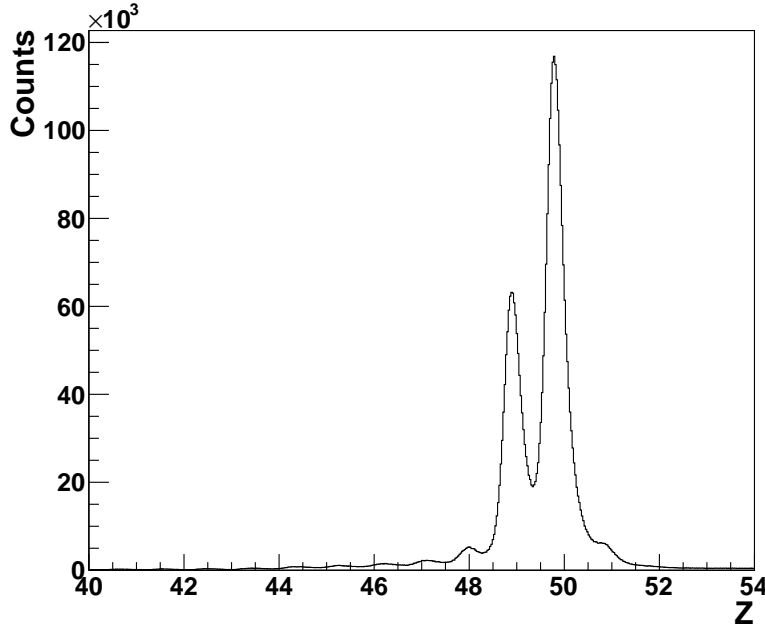


FIGURE 4.4. Z values obtained after calibrating the energy loss signals in the MUSIC detector for the dependency of the energy loss in the gas with the velocity of the fragments, for the ^{104}Sn measurements.

4.2.2 Calibration of the ToF

The ToF calibration is performed using the standard plastic scintillator at the intermediate focal plane and it is further used for the Finger detector calibration by means of an offset.

The ToF of the ions was measured in the second half of FRS and the quantity obtained can be expressed as

$$TOF_m = t_m + dt - t_f , \quad (4.3)$$

where t_m is the time from the scintillator at the intermediate focal plane, t_f is the time from the scintillator at the final focal plane and dt is the delay applied to t_m . The delay was needed since the plastic at the end of FRS is the one used to trigger the data acquisition system. From the previous equation, the following relation between TOF_m and the velocity of the fragments β could be deduced (all the steps can be found in [66]):

$$TOF_m \cdot \beta = \Delta T - \frac{d}{c} \beta . \quad (4.4)$$

The term d is the distance between the two scintillators, c is the speed of light and ΔT is an offset related to the value of β . The offset has been determined considering the velocity of the primary beam at different energies, similarly to the method used to calibrate the MUSIC, as shown in Fig. 4.5.

The relation between $TOF_m \cdot \beta$ and β has been fitted writing equation (4.4) as

$$TOF_m \cdot \beta = a_0 + a_1 \beta . \quad (4.5)$$

Hence the values of ΔT and $-\frac{d}{c}$ in eq. (4.4) have been obtained from the coefficients a_0 and a_1 , respectively.

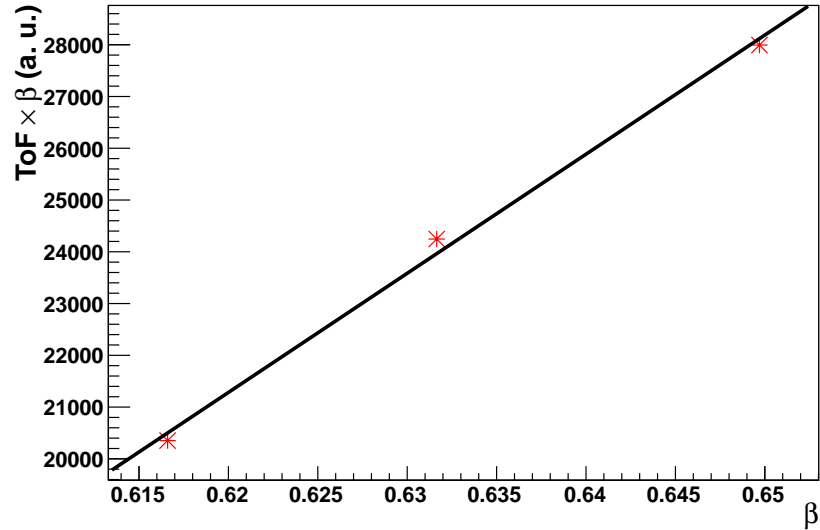


FIGURE 4.5. Plot of β versus $TOF_m \cdot \beta$ used to calibrate the ToF in relation to the velocity of the fragments. The range spanned by the three points, obtained using the primary beam at different energies, includes the expected energy of the fragments.

The function used for the fit was a polynomial of first order.

Moreover, since the light produced in the scintillators was collected at the sides by two PMTs, their signals has a time difference related to the position of the ion passing through the scintillator area. It has therefore been necessary to correct for this

dependency for the accurate extraction of the ToF. In Fig. 4.6 the position of the ion determined from the TPCs is shown versus the time difference from the two PMTs (Δt). The relation between the two values is obtained performing a fit of the data with the following polynomial function of second order:

$$X = a_0 + a_1\Delta t + a_2\Delta t^2 . \quad (4.6)$$

Hence, the coefficients a_0 , a_1 and a_2 , are used to correct the time signals.

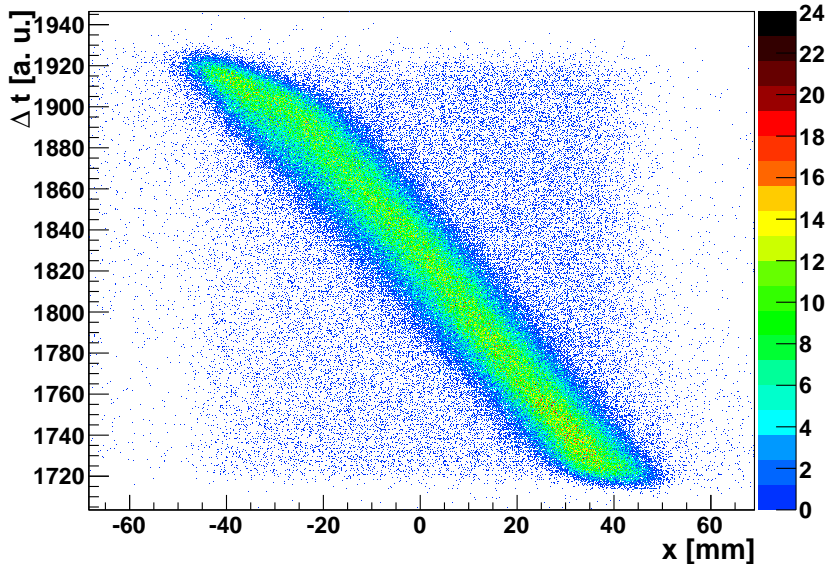


FIGURE 4.6. Position of the ion from the TPC versus the time difference of the two PMTs signals of the scintillator at the final focal plane.

4.2.3 A/q correction for position dependency

The A/q value can be uniquely deduced from equation (3.4) as the magnetic rigidity and the velocity β of the fragments is known. Nevertheless, the momentum spread of each species at the final focal plane results in a dependency of A/q on the position, as in the plot on the left of Fig. 4.7, which entails a broader distribution of A/q values. This effect has been corrected for in order to improve the separation of the isotopes in the identification plots presented in the following paragraphs.

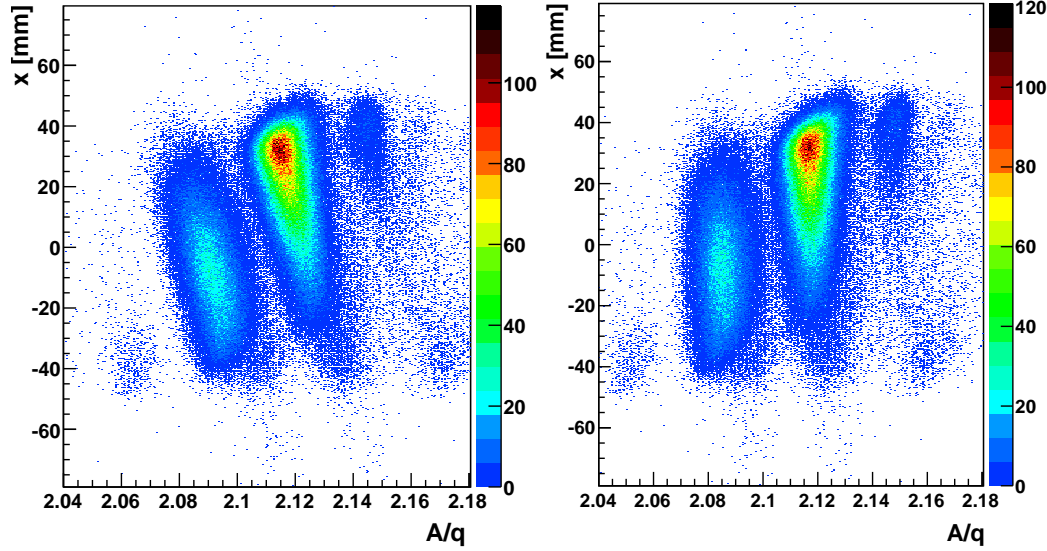


FIGURE 4.7. A/q versus the position of the ions from a TPC at the final focal plane, for the ^{104}Sn measurement. On the left it is possible to observe a dependency of A/q on the position, while on the right the same plot is shown with a correction of this dependency applied.

4.2.4 Isotope selection

For a clear identification of the wanted transition, it was fundamental to exclude from the analysis the isotopes different from the one of interest that passed through the FRS and could react in the target. ^{104}Sn , ^{105}Sn , ^{103}In and ^{104}In have been identified with the two-dimensional plot of Fig. 4.8. A selection was performed applying in a sequential way a condition on the Z values (as in Fig. 4.9) and a graphical cut on the A/q versus the position plot (Fig. 4.10).

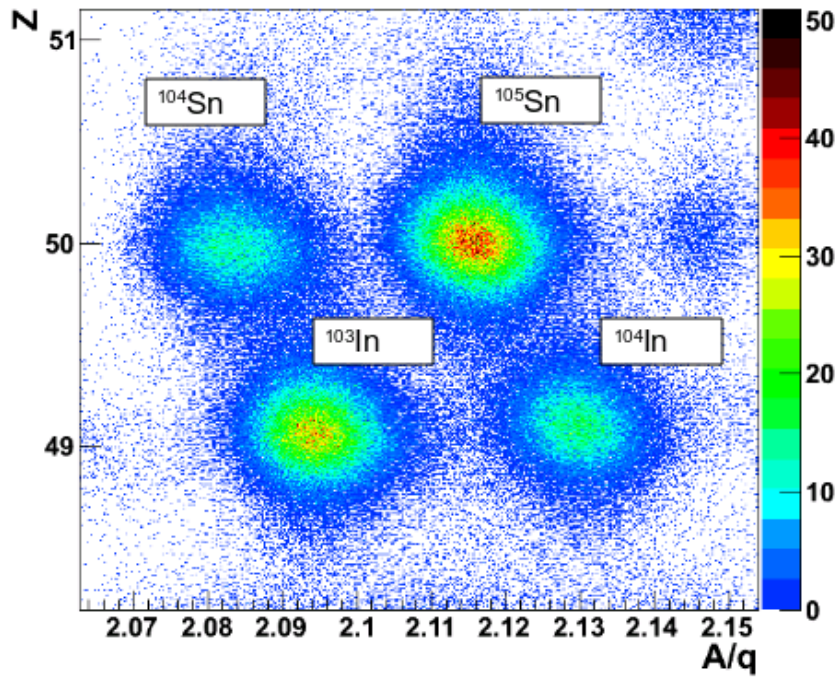


FIGURE 4.8. A/q distribution deduced from ToF measurement versus Z of the ions obtained from the MUSIC, for the ^{104}Sn measurement. The values of A/q have been corrected for the dependency on the x position at the final focal plane (see Par. 4.2.3).

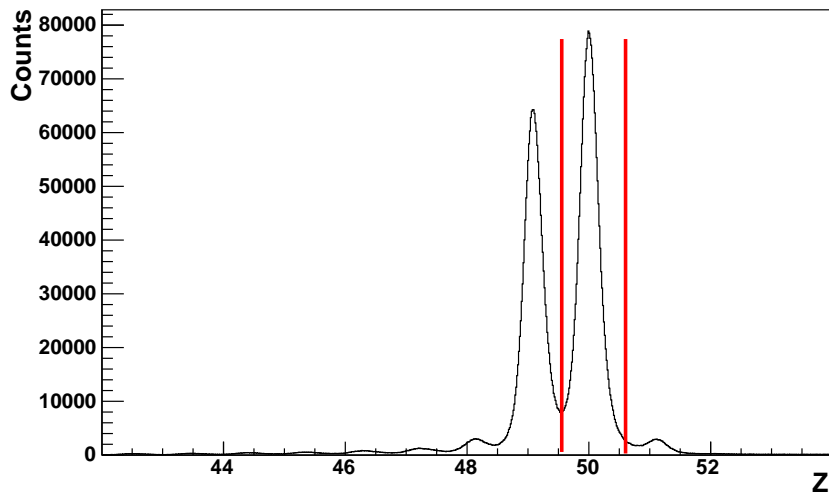


FIGURE 4.9. Spectrum of the values of Z obtained from the MUSIC detector. The events between the two red lines are the ones selected for the analysis of ^{104}Sn .

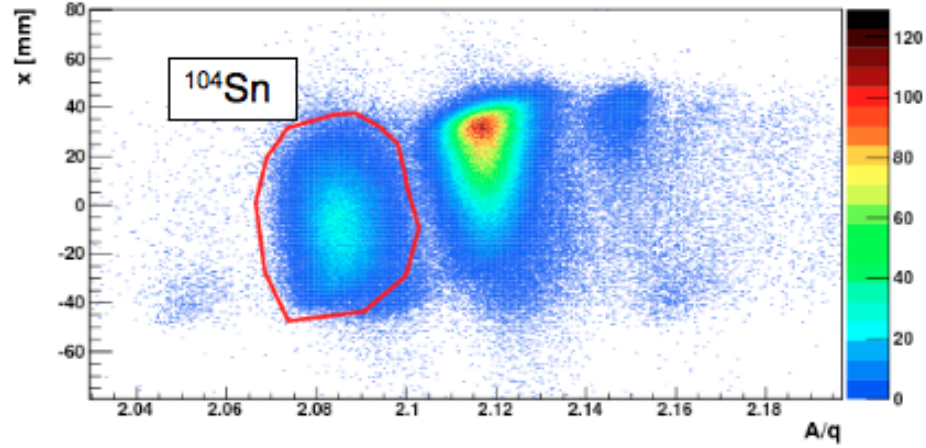


FIGURE 4.10. A/q from ToF measurement versus the position on the x axis of the ions at the final focal plane from the TPC, after a restriction on the nuclei with $Z=50$ has been applied to the data.

A selection of the isotope of interest had to be performed also after the secondary target to exclude products of proton knock-out or fragmentation reactions. It is possible to distinguish the Z of the nuclides after the target via the $\Delta E-E$ plot obtained from the LYCCA wall array (see Fig. 4.11). The selections of the events, also in this case, have been performed applying a graphical cut.

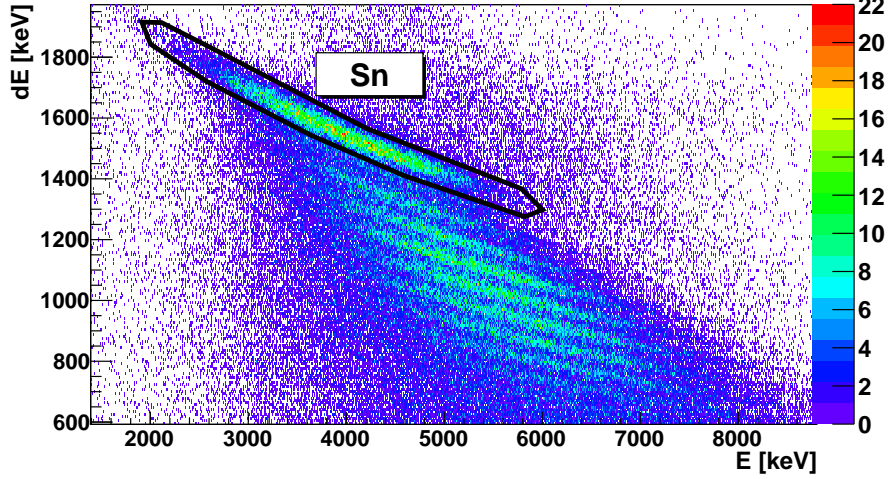


FIGURE 4.11. Total energy deposited by the ions in the CsI(Tl) crystals of the LYCCA wall telescope versus the energy loss from the DSSSD detectors for the events selected as ^{104}Sn in the FRS. The graphical cut, shown with a black line, selects the ions that had the same Z before and after the target.

4.2.5 Determination of the velocity of the ions after the target

Due to the high velocity of the ions after the secondary target (about $0.5 c$), the detected γ -rays were shifted in energy by the Doppler effect (see Sec. 3.3). The value of the energy emitted at rest ($E_{\gamma 0}$) have been deduced from the detected value (E_{γ}) with the formula

$$E_{\gamma 0} = E_{\gamma} \frac{1 - (v/c) \times \cos\theta_{\gamma}}{\sqrt{1 - (v/c)^2}} , \quad (4.7)$$

where v is the velocity of the ion and θ_{γ} is the angle between the emitted radiation and the trajectory of the ion. The velocity of the ions could not be obtained from the ToF measurement after the secondary target and it has been therefore extracted employing an indirect method. This was based on the consideration that the counts in the γ -ray energy spectrum were clustering around the proper energy (the one related to the $2^+ \rightarrow 0^+$ transition) when the Doppler shift correction was done with the right value of β , while they would have progressively smeared when moving away from it. The Doppler correction has been therefore performed for several values of β (see Fig. 4.12). The event-by-event β values obtained from ToF measurements in the FRS have been decreased by 0.1 % at each step, so that the information on the velocity spread before

the target was kept. A value has then been chosen by looking in which γ ray energy spectrum the peak associated to the transition of interest was having the best peak-to background ratio

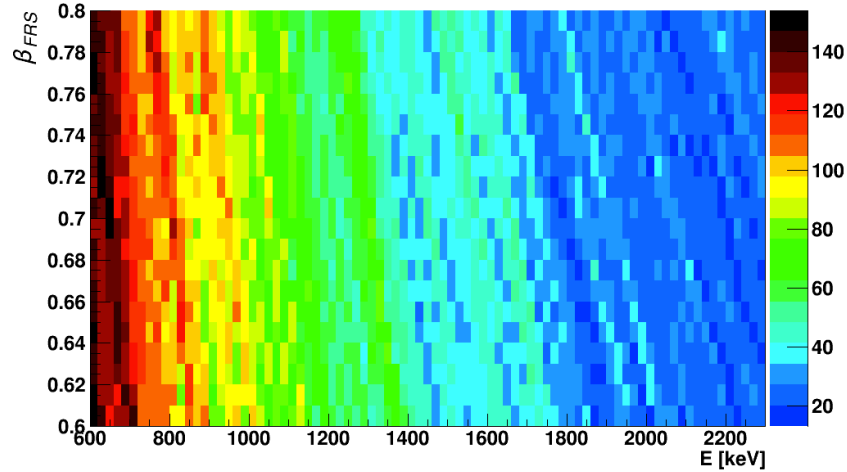


FIGURE 4.12. Doppler corrected γ -ray energy spectra (x axis) performed for twenty different values of β (y axis). The latter were obtained decreasing of 0.1 % at each step the event-by-event value measured in FRS. The final spectrum has been chosen by looking at the projections on the x axis [67].

4.2.6 γ -time range selection

The radiation originating from the decay of the first 2^+ state of ^{104}Sn was expected to lie in the prompt peak of the Ge-time spectrum since it had a life time of few ps. It is possible to observe in Fig. 4.13 that the peak associated to the prompt radiation is broad and has a high number of counts. This tells that the atomic background and the radiation from unwanted reactions in the target are also contributing to it and they are hiding the one of interest. In order to reduce as much as possible the background, the time spectrum has been plotted versus a Doppler corrected energy spectrum (once the value of β has been determined). The time window for which the transition peak of interest was visible best above the background was chosen. A narrow time range of about 15 ns has been then used in the analysis to select the data.

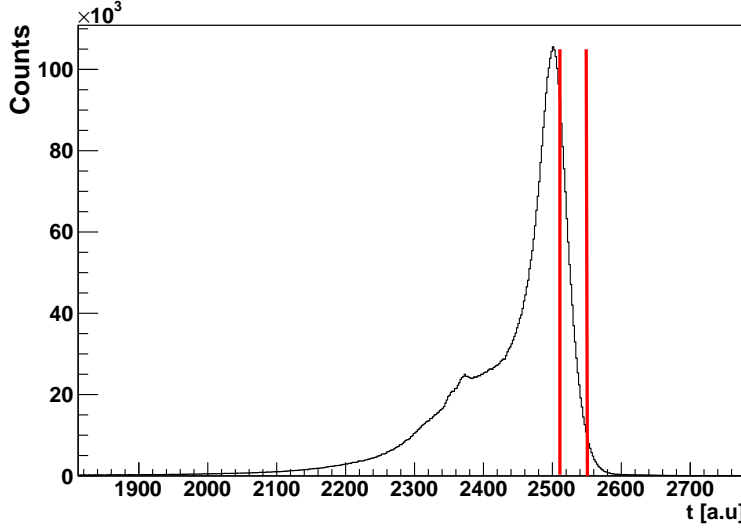


FIGURE 4.13. Time spectrum from the Germanium detectors (the scale is inverted). The borders of the chosen time range are shown by the two red lines (about 15 ns).

4.2.7 Scattering angle range selection

The scattering angle of the ions at the secondary target has been calculated using the position information from the TPCs at the final focal plane and the DSSSDs of LYCCA.

For experiments using beam energies of about 100 MeV/u and a ^{197}Au target, as in the measurement for ^{104}Sn and for ^{112}Sn , the largest scattering angle to consider in order to reduce the contribution of nuclear reactions has been calculated to be $\simeq 3^\circ$, as explained in Sec. 4.1. Nevertheless, the range of angles selected in the analysis has been chosen looking at the Doppler corrected energy spectra for different ranges of scattering angle (Fig. 4.14). This procedure allowed to exclude with more accuracy the angles at which the background was dominating and to select the range where the wanted transition could be observed. A final narrow range of 15 - 40 mrad (0.9° - 2.3°) was determined.

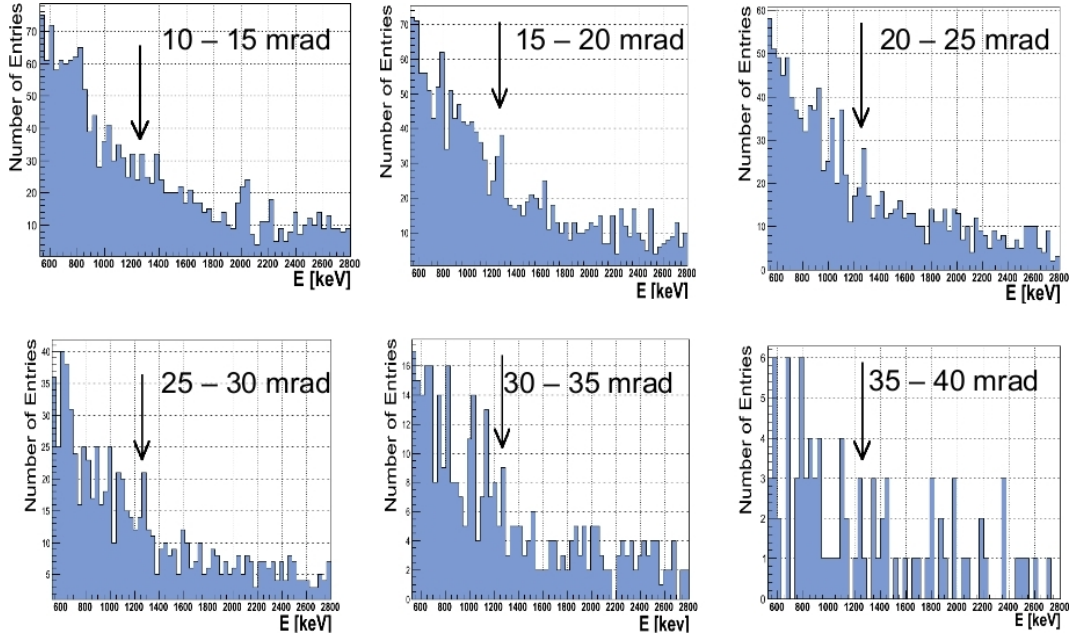


FIGURE 4.14. Examples of γ -ray energy spectra produced gating on different ranges of the scattering angle for the ^{112}Sn experimental data. Below 15 mrad the contribution from elastic scattering is covering the peak corresponding to the $2_1^+ \rightarrow 0^+$ transition.

4.3 Extraction of the result and discussion

After selecting the data via the aforementioned methods and performing Doppler shift correction of the γ -ray energies, the final spectra presented in Fig. 4.15 have been obtained. The peak associated to the transition from the first 2^+ state to the ground state are visible at 1257 keV and 1260 keV for ^{112}Sn and ^{104}Sn , respectively.

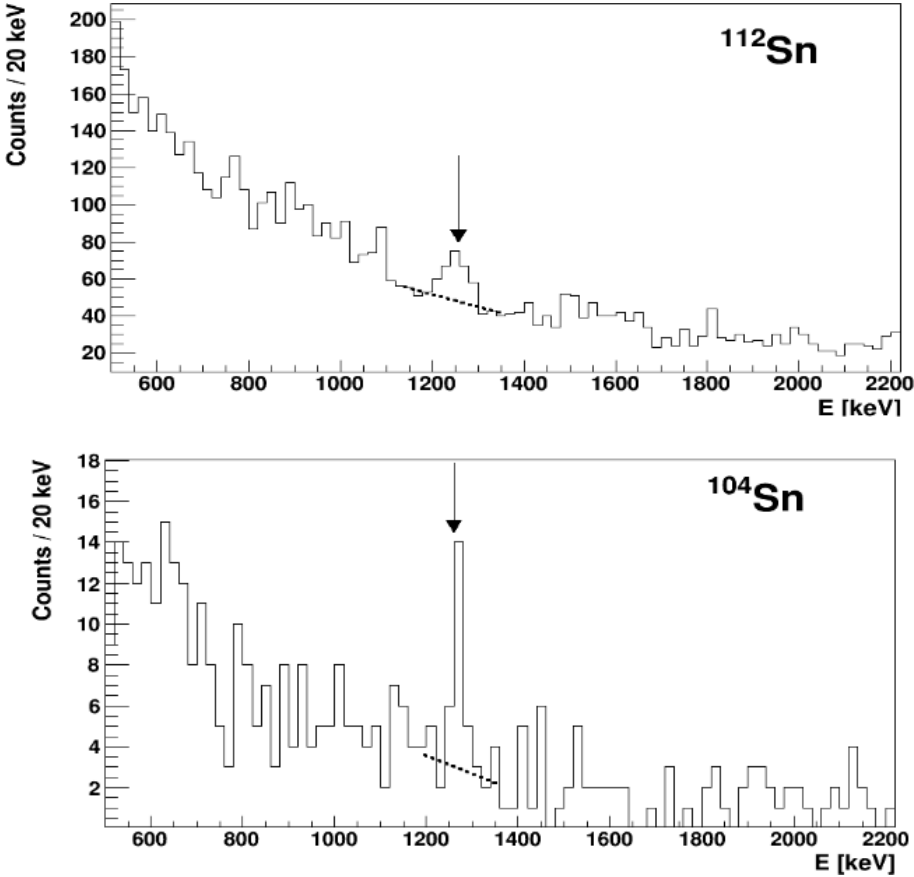


FIGURE 4.15. Doppler corrected energy spectra for ^{112}Sn (upper panel), and for ^{104}Sn (lower panel). The peak associated to the $2^+ \rightarrow 0^+$ transition is indicated by the arrow. The dashed line indicates the estimated background level.

It can be observed that the width of the peaks is different in the two cases. The larger FWHM in the case of ^{112}Sn is explained considering that the life time of its 2^+ state is shorter and the decay can occur more often inside the target. This entails a larger spread in velocity of the ions, and therefore a broader distribution of counts in the peak due to a less accurate Doppler correction. This hypothesis has been confirmed simulating the energy straggling in the target for the two different cases (see Fig. 4.16).

In the following paragraphs, the extraction of the photon yields from the identified peaks and how it leads to the estimation of the $B(E2)$ value is described. Furthermore the result is compared to predictions from LSSM calculations.

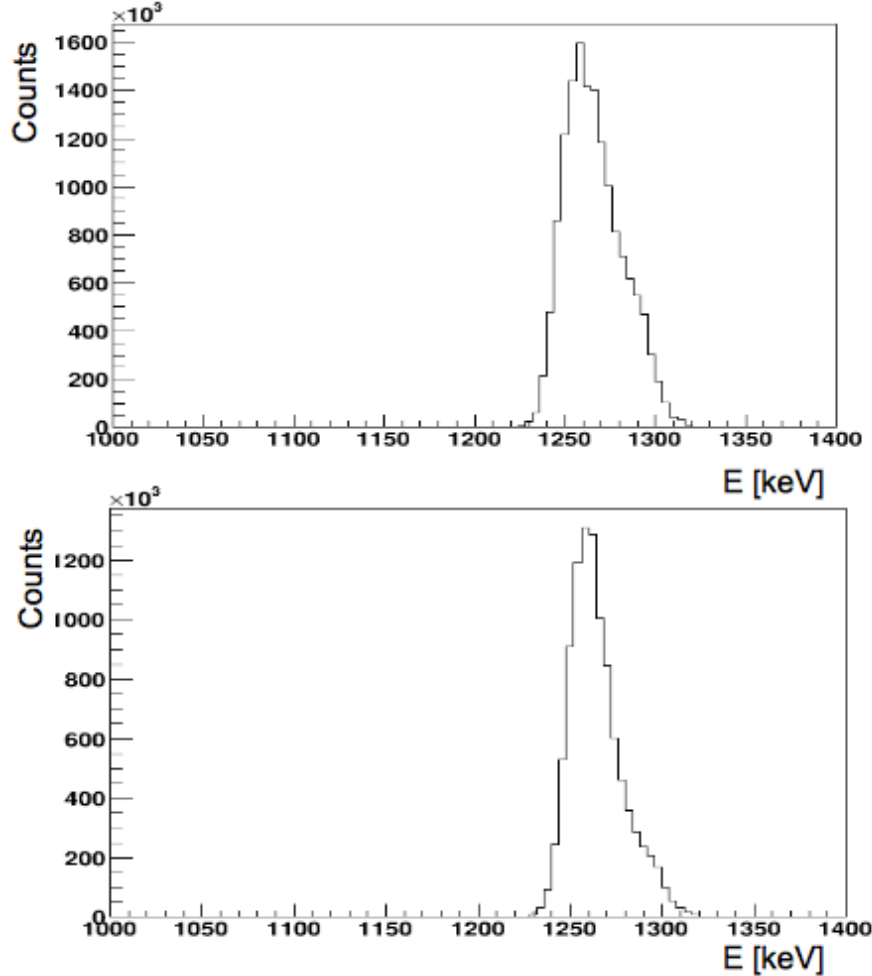


FIGURE 4.16. Simulated peak shape for the $2^+ \rightarrow 0^+$ transition for ^{112}Sn (up) and ^{104}Sn (down) considering the energy straggling in the target. The FWHM is 36 keV and 22 keV respectively. The simulation has been performed considering a fixed incoming velocity and only one angle for the Germanium detector (courtesy of P. Boutachkov).

4.3.1 Estimation of the background level

To determine the photon-yield, the background level was extracted considering the average number of counts in regions on the left and on the right of the peaks. In the following, B refers to the region which included the peak, A the one on the left and C the one on the right. The counts associated to the photon-yield (B_{ph}) were then evaluated as

$$B_{ph} = B - \frac{w_B}{w_A + w_C} (A + C) , \quad (4.8)$$

where w_A , w_B and w_C are the widths of region A, B and C respectively. The statistical error associated to B_{ph} was obtained with the error propagation method [68] using the formula

$$\sigma_{B_{ph}} = \sqrt{B + \left(\frac{w_B}{w_A + w_C} \right)^2 (A + C)} . \quad (4.9)$$

The width of the A and C regions was chosen considering several aspects. The shape of the background was similar for both spectra but the level was significantly higher in the ^{112}Sn case. This resulted from the higher instantaneous rate in the measurement of this nucleus, which increased the random coincidence probability. Moreover, the profile of the background is not a simple smooth decreasing exponential curve. Spurious peaks are present on the right of the peak associated to the $2^+ \rightarrow 0^+$ transition in ^{112}Sn . The origin from other reactions in the target was excluded as their presence is not stable in respects to slight changes in the analysis.

4.3.2 Extraction of the $B(E2)$ value

The reduced transition probability for the $2^+ \rightarrow 0^+$ transition is proportional to the cross section for Coulomb excitation of the 2^+ state (σ_{E2}) through the relation [69, 70]

$$\sigma_{E2} = f(b_{min}) \times B(E2) , \quad (4.10)$$

where the proportionality factor $f(b_{min})$ takes into account the dependence on the impact parameter. Hence, the reduced transition probability for ^{104}Sn was deduced relatively to the one for ^{112}Sn as

$$B(E2)_{104} = B(E2)_{112} \times \frac{\sigma_{E2}^{104}}{\sigma_{E2}^{112}} \times \frac{f(b_{min}^{112})}{f(b_{min}^{104})} . \quad (4.11)$$

The Coulomb excitation cross section is then determined with an experimental approach from the number of incoming particles (N_p), the number of atoms in the target per unit area (N_t) and the number of the detected γ -rays originated in the $2^+ \rightarrow 0^+$ transition. The latter can be expressed as the ratio between the photon-yield from

the $2^+ \rightarrow 0^+$ transition (N_γ) and the detection efficiency (ϵ). The Coulomb excitation cross section for the 2^+ state then results

$$\sigma_{E2} = \frac{\frac{N_\gamma}{\epsilon}}{N_p \times N_t} . \quad (4.12)$$

The term ϵ was assumed to have the same value in the two measurements, since the energies of the excited 2^+ states in ^{104}Sn and ^{112}Sn are very close (1260 keV and 1257 keV, respectively). A similar consideration was made for N_t since the same target was used in the two measurements. Hence, the B(E2) value for ^{104}Sn was obtained from the formula:

$$B(E2)_{104} = B(E2)_{112} \times \frac{N_p^{104}}{N_\gamma^{112}} \times \frac{N_p^{112}}{N_p^{104}} \times 0.96. \quad (4.13)$$

The factor 0.96 originates in the correction for different impact parameters for $^{104,112}\text{Sn}$ ions as calculated with the code DWEIKO [71]. The terms N_p^{104} and N_p^{112} indicate the incoming flux of ^{104}Sn and ^{112}Sn particles, respectively, determined from FRS identification plots. N_γ^{104} and N_γ^{112} are the corresponding photon-yields, which have been extracted from the peak integrals in the γ -ray energy spectra, once the contributions from the background was estimated.

4.3.3 Result and comparison with LSSM calculations

The final Doppler corrected energy spectra and the estimated background level are shown in Fig. 4.15. The photon-yield for the $2^+ \rightarrow 0^+$ transition was determined as 16(5) counts and 95(24) counts for ^{104}Sn and ^{112}Sn , respectively. A reference value of $B(E2) = 0.242(8) \text{ e}^2\text{b}^2$ for ^{112}Sn as measured in a sub-barrier Coulomb excitation experiment was used [41]. The final B(E2) value extracted for ^{104}Sn is $B(E2; 0^+ \rightarrow 2^+) = 0.10(4) \text{ e}^2\text{b}^2$ (or $B(E2) = 6.9(30) \text{ W.u.}$) [72], which corresponds to a lifetime of the first 2^+ state $\tau=1.3(4) \text{ ps}$. This new B(E2) value is three standard deviations smaller than the average of the $^{106-114}\text{Sn}$ values and two standard deviations smaller than the ^{106}Sn data [40] (see Fig. 4.17). It therefore clearly establishes a decreasing trend for the B(E2) values towards ^{100}Sn , despite the large uncertainty from the low statistics in the spectra.

Subsequently to the experiment presented in this work, new measurements of the B(E2) value in ^{104}Sn were carried out in two different laboratories. At RIKEN (Japan), the

availability of high intensity radioactive beams allowed to extract the E2 transition strength as $B(E2) = 0.173(28) \text{ e}^2\text{b}^2$ from the determination of an absolute cross section [73]. A measurement performed at MSU (USA), moreover, provided the result $B(E2) = 0.180(37) \text{ e}^2\text{b}^2$, normalized to the $B(E2)$ value of ^{102}Cd (measured during the same experiment) [74]. These further results are presented in Fig. 4.17 and summarized in Tab. 4.1. It can be noticed that they are located higher than the result obtained at GSI. However, all the measurements are in agreement within one sigma of the average value. All the results at present available for ^{104}Sn are consistent with the conclusion obtained from the GSI value: the persistence of a higher $B(E2)$ value toward ^{100}Sn is ruled out, while a decrease toward lighter tins is evident.

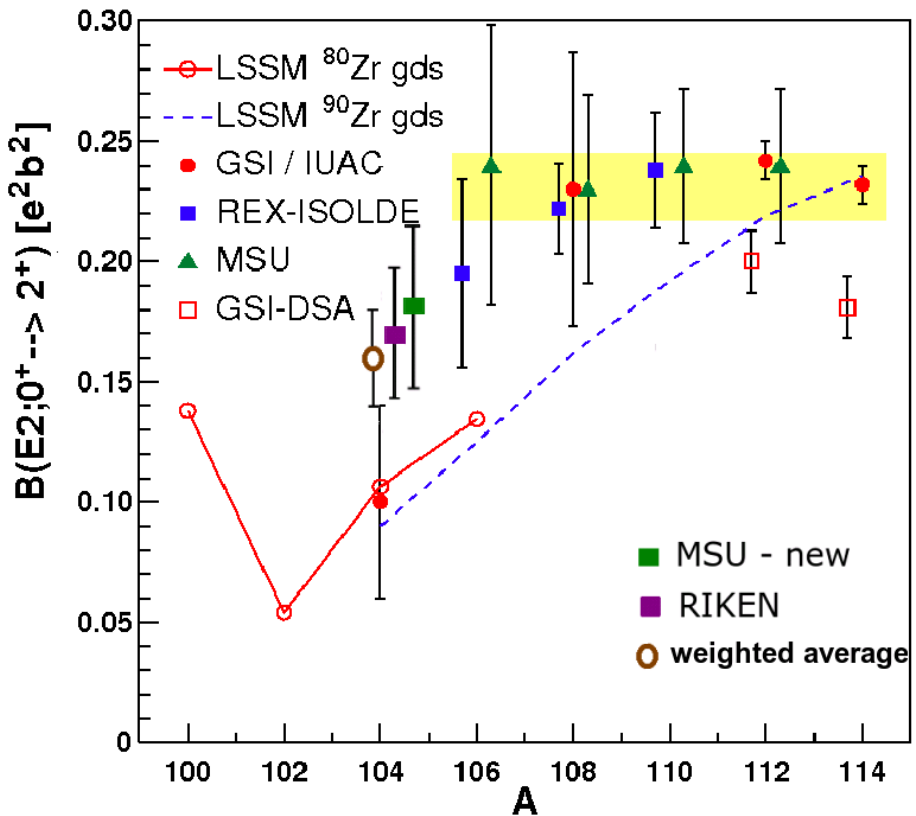


FIGURE 4.17. Experimental $B(E2; 0^+ \rightarrow 2^+)$ values for $^{104-114}\text{Sn}$. The average of the $B(E2)$ values in $^{106-114}\text{Sn}$, weighted on the respective uncertainties, is indicated by the yellow band (see references in the caption of Fig. 2.2) [72]. For ^{104}Sn , the results obtained from measurements performed in GSI, RIKEN [73] and MSU [74] and the average of the three values, weighted on the respective uncertainties, are reported.

TABLE 4.1. Results for the B(E2) value measurements performed on ^{104}Sn at the different laboratories and the average of the three values, weighted on the respective uncertainties.

Laboratory	B(E2) (e^2b^2)
GSI	0.10(4)
RIKEN	0.173(28)
MSU	0.180(37)
mean value	0.16(2)

The new results have been compared with predictions from LSSM calculations (introduced in Sec. 2.1). A calculation, performed for the N=104-132 Sn isotopes, considered a ^{90}Zr core and the full gds ($0g_{7/2}$, $1d_{5/2}$, $0g_{9/2}$, $1d_{3/2}$, $2s_{1/2}$) valence space (dashed-blue line). The effective interaction was derived from a realistic CD-Bonn potential and adapted to the model space by many-body perturbation theory techniques. For both protons and neutrons, a canonical polarization charge ($\delta e = 0.5e$) was used. A truncation $t_\pi = 4$ has been applied, which is at the limit of the current computational capabilities for $N > 56$ Sn isotopes. For the very light $^{100-106}\text{Sn}$, instead, calculations with more degrees of freedom are possible: the limit of t for ^{100}Sn is 6 and this value decreases as valence neutrons are added. In order to consistently compare the prediction for these light nuclei, the truncation level was set to $t_\pi = 4$ and $t_\nu = 2$ (full red line). In this case, a ^{80}Zr core was considered and the residual interaction has been normalized on account of this. The full gds space for both protons and neutrons was included. As in the previously described calculations, a canonical polarization charge was used. The local minimum of the predicted B(E2) values in ^{102}Sn is related to the assumption of a strong shell closure: assuming a relatively scarce configuration mixing, the presence of two neutrons in the $1d_{5/2}$ orbital induces the blocking of the E2 excitations. A similar local minimum of the E2 excitation strength is indeed observed in the neighboring semi-magic even-even isotope of the doubly magic ^{132}Sn .

In ^{104}Sn and ^{106}Sn , where the two calculations are overlapping, the moderate enhancement of the B(E2) values due to the inclusion of the two neutrons degrees of freedom can be observed. It can therefore be deduced that neutrons are contributing to the E2 excitation strength but most of the E2 strength is due to the protons. Despite this small difference in the overlapping predictions, both calculations predict a downward trend of the B(E2) values toward ^{100}Sn . The result for ^{104}Sn presented in this work

is in very good agreement with the predicted values from these calculations and it therefore establishes a strong reduction of E2 excitations toward the $N=Z=50$ core in the vicinity of ^{100}Sn , confirming the presence of a robust shell closure. However, a correct SM prediction of the experimental $B(E2)$ values in $^{106-114}\text{Sn}$ is still missing. At the moment, a better reproduction of the experimental $B(E2)$ values in the light tin isotopes has been obtained considering an isovector-dependent neutron effective charge, proposed already in the nuclear structure book of Bohr and Mottelson [75]. In Fig. 4.18, the $B(E2)$ values have been calculated considering an isovector-dependent neutron effective charge normalized at $N=66$ and using SPE states from fit on the available values of excited states in the tin isotopes [76, 77]. The curve obtained is asymmetric and provides a relatively good reproduction of the experimental $B(E2)$ values in light tin isotopes (even if the values at $^{112-114}\text{Sn}$ are not yet reproduced). In order to explain the enhancement of the experimental values and the need of a larger neutron effective charge to reproduce them, several effects that are not included in the calculations due to the truncation scheme have been considered. $2p - 1h$ proton excitations which drive to prolate core deformation were noticed in the Sb ($Z=51$) isotopic chain down to $N=56$ [78, 79]. This observation could suggest the necessity of an increased interplay of proton $p - h$ configurations, beyond the present truncation level [74]. Moreover, the presence of protons and neutrons occupying the same orbital, due to the proximity of the $N=Z$ line, induces an increase of the α -correlation energy. The formation of α -clusters have been used, for instance, to describe the low-lying spectrum of ^{58}Ni in terms of $4p - 2h$ proton excitations. Taking into account the similarities in the nuclear structure of ^{56}Ni and ^{100}Sn , α -clusters from $2p - 2h$ proton excitations can therefore be assumed to play an important role also in the light Sn isotopes and to influence their $B(E2)$ values [40]. However, more indications of the presence and of the impact of α -correlations have to be found to further proceed on this subject. Other experimental evidences, as the low 2^+ and 4^+ states in ^{110}Xe [80], suggested the presence of an increased collectivity at the $N=Z=50$ shell closure due to the arising of a strong isoscalar pn interaction. Nevertheless, the theoretical work in Ref. [81] attributed the rotational-like features in the light Xe isotope as an expected effect of the six neutrons and four protons outside the ^{100}Sn core, which does not entail a breaking of the shell closure.

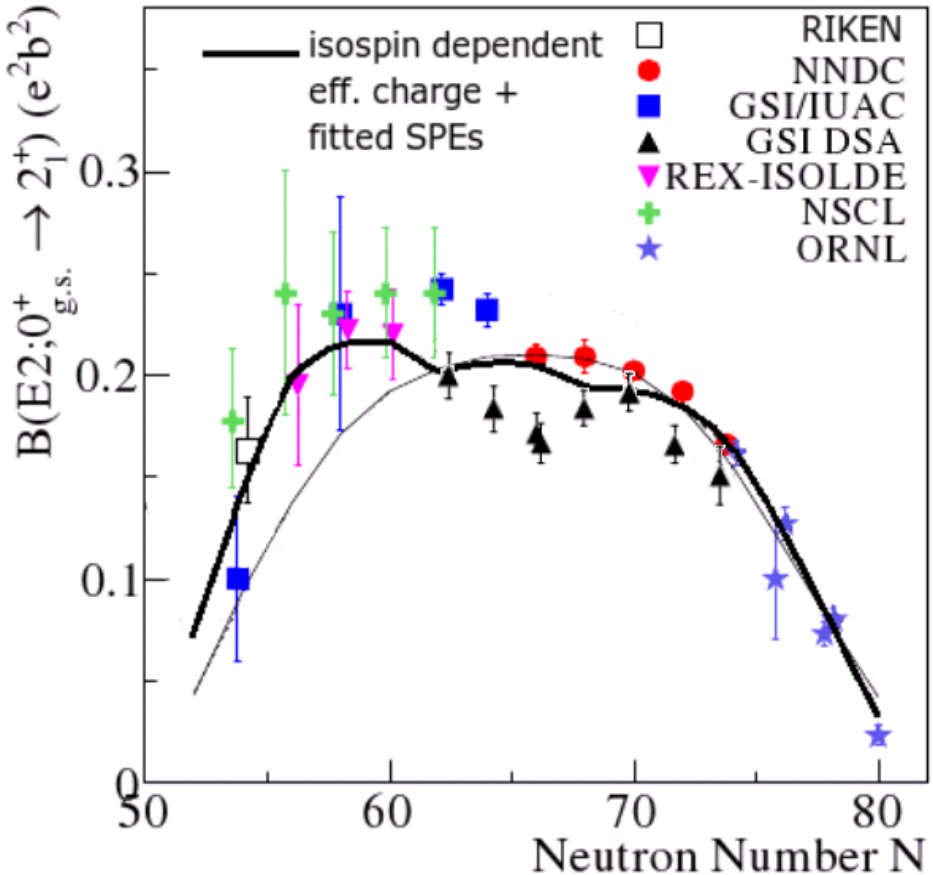


FIGURE 4.18. The $B(E2)$ values calculated considering an isovector-dependent neutron effective charge, normalized at $N=66$, and SPE states fitted on the excited states in the tin isotopes [76, 77] are represented by a thick black line (picture modified from Ref. [77]). The thin black line and the experimental $B(E2)$ values are described in the caption of Fig. 2.2.

In conclusion, an increase of $p - h$ excitations in the light tin isotopes is observed from the measured enhancement of the $B(E2)$ values with respect to the SM predictions. The use of a larger neutron polarization charge helps to reproduce these values, indicating that more proton correlations across the shell gap have to be included in the calculations. Whether this is required due to the present truncation limit, to the formation of α -clusters or from other collective phenomena related to the vicinity to the $N=Z$ line, is to be clarified. Nevertheless, the new result presented in this Chapter shows that the larger than expected collectivity at the shell gap in light tin isotopes is recovered already at ^{104}Sn , proving the presence of a stiff shell closure in ^{100}Sn .

Chapter 5

Analysis of the background observed with PreSPEC

Relativistic rare isotope beams allow spectacular results, however during their identification the large amount of background radiation co-produced is a great challenge for the analysis process. Even after a detailed analysis and the application of strict conditions, a large component of the background can remain in the γ -ray energy spectra and often hamper the observation of the searched for transition. Moreover, the loss in γ -ray detection efficiency that it involves goes beyond the background sources described in Chapter 3. Hence, a dedicated and detailed analysis has been performed in order to better disentangle several components of the background that affects γ -ray energy spectra, and understand their nature and origin, i.e. in which reaction they are produced and whether they are real physical phenomena or failure in the electronics detector response. The final aim is to figure out which modifications of the experimental setup or specific conditions in the data analysis can reduce the presence of background events in the γ -ray energy spectra and, therefore, facilitate the achievement of new physics results in fast beam experiments on very rare nuclei.

In the following paragraphs, the main evidences obtained from the analysis of the background performed on the data from the ^{104}Sn experiment (EUROBALL phase) are presented. The investigation started classifying the different type of hits registered in the detectors according to different parameters provided by the cluster array (energy, time, crystal and cluster multiplicity, position of the crystal). Each class of events has been then characterized by means of the information provided by all the other detectors available in the setup. Afterwards, an evaluation of the impact of the background events in the observation of the transition of interest has been performed. Data from

an AGATA experiment conducted in 2012 analyzing the signal traces have been also used for a comparison of the observed effects with Euroball data.

To provide a clear understanding of the analysis described in the following sections, it is important to define few terms, as well as some specifications of the setup. In experiments with the PreSPEC setup, an *event* is considered to occur every time a particle passes through the scintillator at the final focal plane and a γ -ray (with energy ≥ 100 keV) is registered in at least one crystal. All the signals registered in coincidence, within a fixed time interval, to this triggering signal are acquired by the data-acquisition system and associated to the same event. Obviously, more than one hit in the germanium detectors can be registered for each event. In the case of the Euroball cluster array, each crystal can produce only one signal per event, even if it was hit more than once. In the following, the number of crystals which provided a signal within one cluster is called *cluster multiplicity*), while the number of crystals with a hit among the full array is referred to as *array multiplicity*. The number of events that have at least one time signal in the germanium detectors has been considered as the *total number of events*.

5.1 Background analysis with Euroball data

Looking at the correlation of the time versus energy values of the hits recorded in the Euroball Cluster array (see Fig. 5.1), it is possible to distinguish different groups of hits. A large number of hits have very low (below 80 keV) or very high energy (above 6800 keV). Moreover, hits which are recorded with a time signal but no energy information (*missing energy* hits, which have energy value equal to -1, the number used to initialize the variable in the analysis code) have also been noticed to be often present. In order to investigate the characteristics and the origin of the events producing these hits with unusual energy values, a classification according to four time ranges and four energy ranges (Tab. 5.1 and Tab. 5.2, respectively) has been employed. In the distribution of the time signals of the germanium detectors, several peaks arise and the time ranges have been chosen in relation to them, as shown in Fig. 5.2. The peak in the time range B is the one generated by the prompt γ -rays produced by the interaction of the beam in the target area, since they are related to the expected energy values. Moreover, few hits have a time preceding the prompt ones (time range A) and a large number of hits form two delayed peaks (time range C and D). The presence of hits with unusual energy values in the different time ranges is shown in Tab. 5.3. It can be noticed that the hits in overflow or which have very low energy values are concentrated mainly in

the delayed time intervals (C and D). The missing energy hits, instead, are largely present in all the time intervals and they are 99% of the hits in the time peak before the prompt one (A).

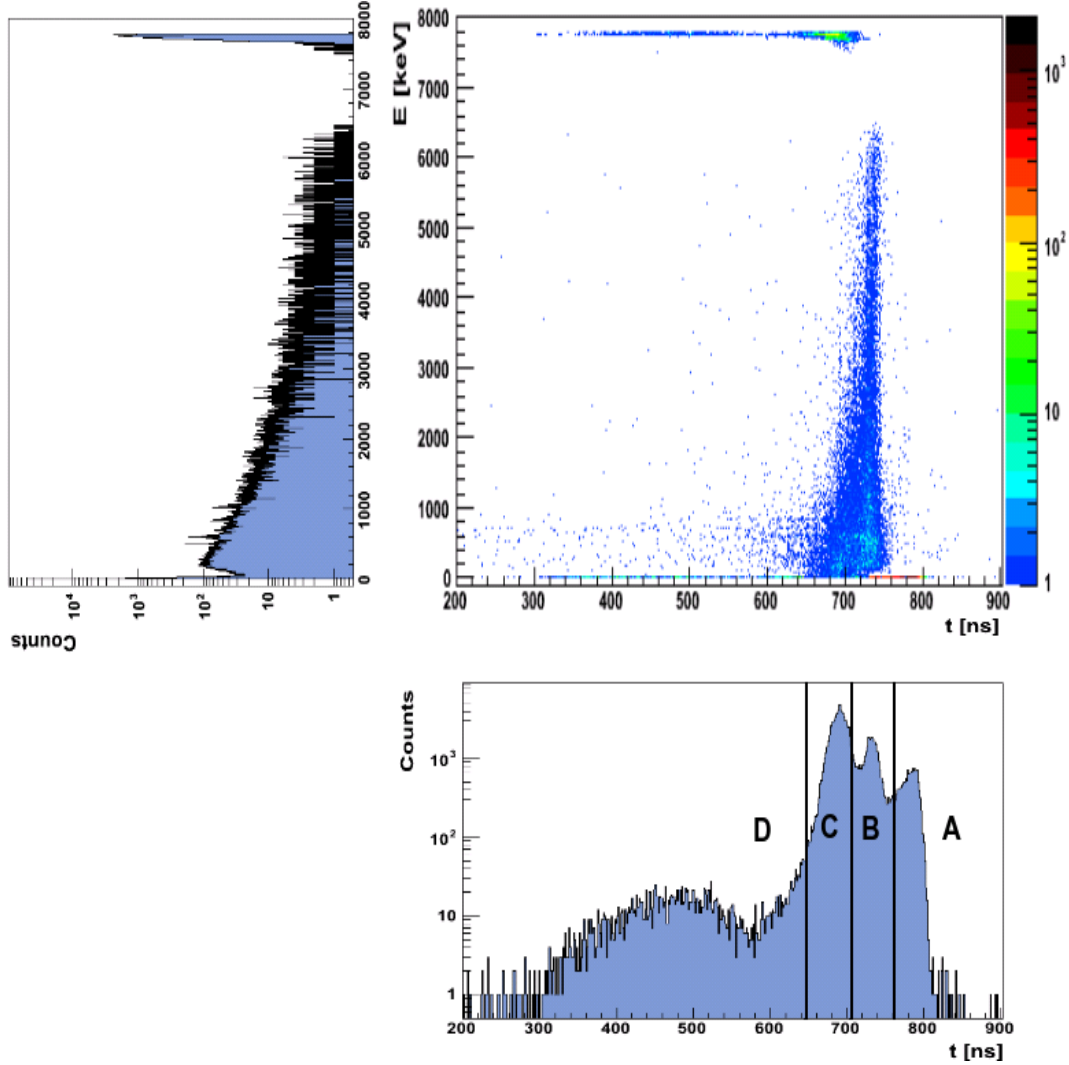


FIGURE 5.1. Time versus energy values of the hits in a crystal of the Euroball Cluster array (the time axis is reversed, i.e. the earliest events are on the right) and the projections on the x (time) and y (energy) axis. The time ranges A, B, C and D are defined in Tab. 5.1.

TABLE 5.1. Classification of hits according to the time registered in the array. In the third column, the occurrence of events with at least one of these hits is given in percent with respect to the total number of events.

Range	[ns]	%
A	≥ 760	40
B	700 - 760	79
C	645 - 700	60
D	≤ 645	16

TABLE 5.2. Classification of hits according to the energy registered in the array. In the third column, the occurrence of events with at least one of these hits is given in percent with respect to the total number of events.

Range	[keV]	%
good energy	80 - 6800	81
low energy	0 - 80	22
overflow	6800 - 8000	34
missing energy	-1	57

TABLE 5.3. Percent of events with at least one hit within the specific energy range and the different time intervals, among the total number of events with at least a hit in the same time range.

Time range	overflow (%)	low energy (%)	missing energy (%)
A	-	-	99
B	2	2	32
C	30	18	41
D	39	18	42

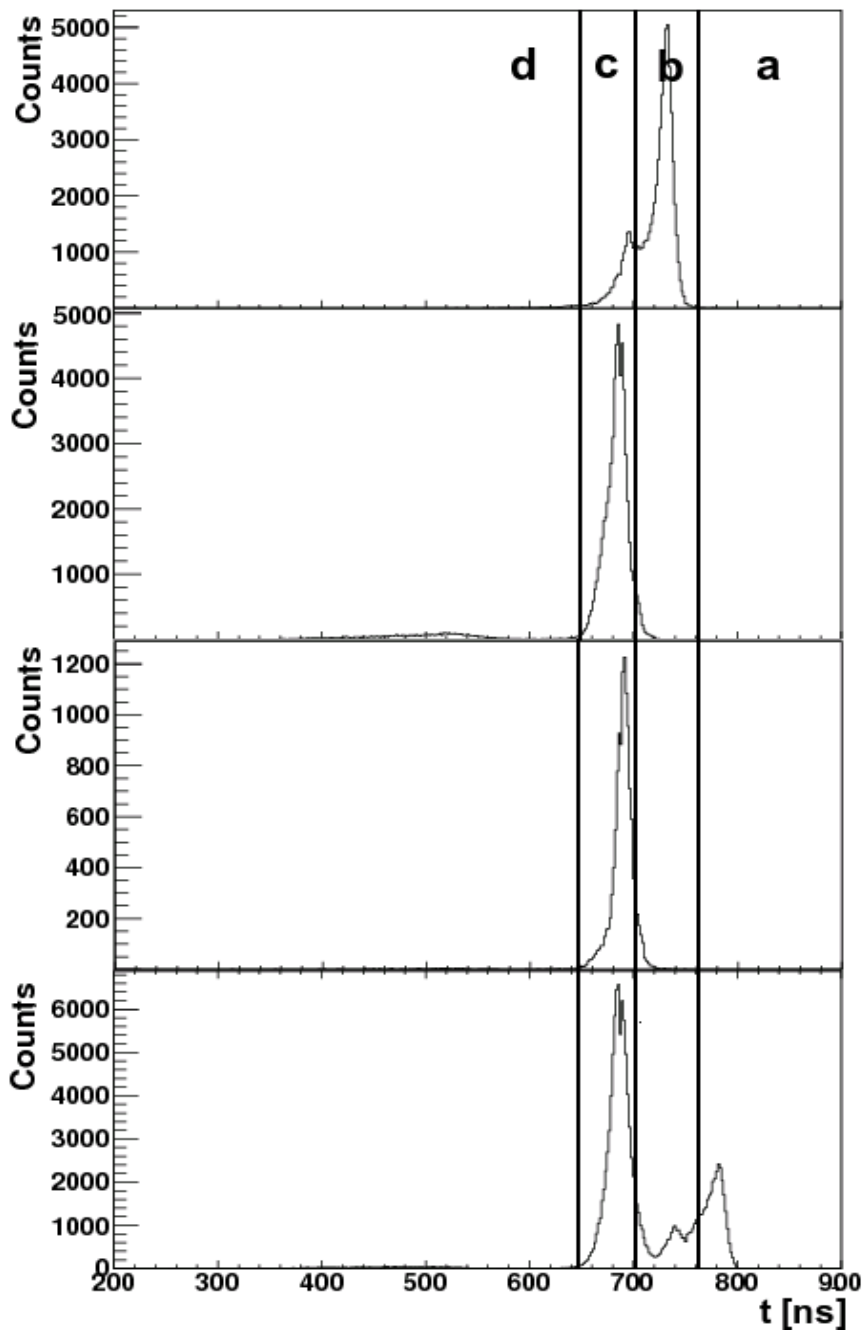


FIGURE 5.2. Crystal time spectra for the different energy ranges (from top to down: good, low, overflow and missing energy values). The vertical lines show the boundaries of the time ranges considered. The x axis is, as in the previous spectra, reversed.

Part of the γ -rays in the time range C (first delayed peak), observed selecting good energy values (80 - 6800 keV), have a time difference of ~ 40 ns, with respect to the time range B (prompt peak) (see Fig. 5.3). This time interval has been calculated to correspond to the sum of the time needed for the reaction products after the secondary target to reach the LYCCA ΔE -E wall telescope plus the time required by the γ -rays produced there to travel back to the Euroball detectors. These hits are therefore due to radiation produced by the implantation of the ions of the beam in the LYCCA ΔE -E wall telescope, similarly to what observed with the RISING setup [52]. Nevertheless, these γ -rays represent only a small part of the hits registered in the time range C. The origin of the rest of the hits in this time range has been therefore studied in more details.

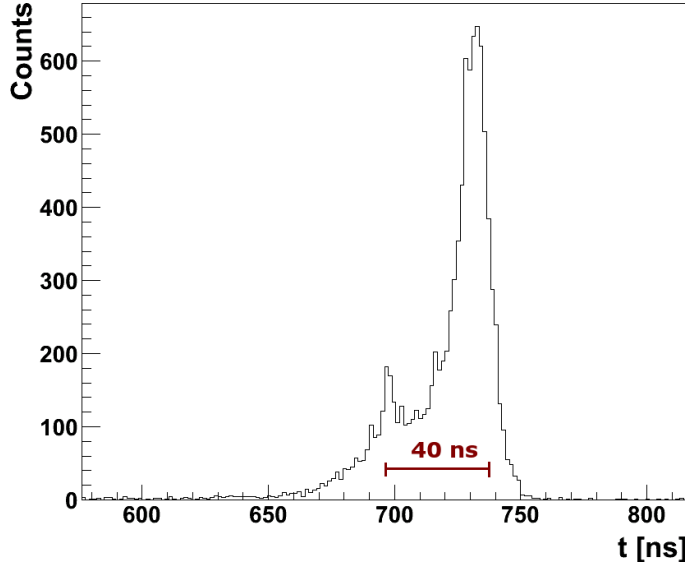


FIGURE 5.3. Time spectrum of the crystals selecting the hits with energy values between 80 and 6800 keV. The time axis is, as in the previous spectra, reversed.

In Fig. 5.4, the cluster multiplicity for the different time intervals is compared: while in A and B the cluster multiplicity is mainly one, in C and in D the average multiplicity is higher. In C, the distribution exhibits a peak at multiplicity one and at six, and considerable contribution at intermediate values. The events with multiplicity six present, most of the time, either hits in overflows, with no energy or with low energy. Moreover, rarely different types of hits are mixed in the same event. In the time range D, the cluster multiplicity is equal, in most of the cases, to one or two, even the average values are relatively high.

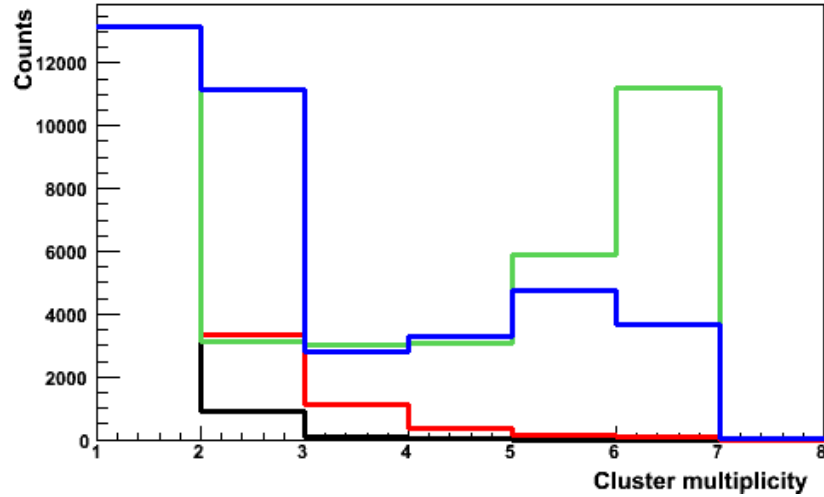


FIGURE 5.4. Cluster multiplicity for hits in time range A (black line), B (red line), in C (green line) and in D (blue line), normalized at the values for multiplicity one. No energy condition has been applied. It can be observed that in the first two cases, the cluster multiplicity is mainly one. In the time range C, instead, in addition to the peak at multiplicity one, a peak at multiplicity six is also present. In the time range D, the cluster multiplicity is mainly one and two but higher multiplicities are also present in a considerable amount.

It is noteworthy that cluster multiplicity seven is never occurring if any of the described time ranges is selected. When the cluster multiplicity is six in the time range C, the seventh crystals of the same cluster has been found to have always a hit in the time range A and no energy information. For multiplicity six in time range D, the situation is similar except that the seventh hit can be also in the time range B. It has been therefore deduced that these hits with no energy information associated to them and separated in time from the other six hits present in the same cluster correspond to the interaction of high energy particles in the germanium detectors that saturate the electronics of the crystal involved. It is indeed expected that the energy deposited in the crystal is far above the range of the preamplifier in use, which, as a consequence, does not provide any energy signal. Since the power of all the crystals in a cluster is provided by the same cable, it is expected that the saturation of the electronics of a crystal alters the voltages applied to all the other detectors in the same cluster. The overflow or the very low energy can be therefore explained as badly shaped signals in the crystals surrounding the saturated one that the DGF system is not able to interpret. Furthermore, the relation between interaction time and signal generation is

also expected to differ from the one for non-saturated signals. The time information provided by the CFD modules in these cases are therefore not directly comparable with the one for γ -rays. As it has been estimated in this work that in more than 30% of the total number of events at least one full cluster is involved, a more detailed investigation has followed.

As described in Chapter 3, the 15 clusters of the Euroball array are arranged in three rings (see also Fig. 5.5). Because of the Lorentz boost effect (see Sec. 3.3, the γ -rays emitted by the beam are mainly concentrated in the inner ring. Nevertheless, the background radiation beam-related is also expected to hit predominantly the crystals closer to the beam line. The analysis of the distribution of the hits with respect to the position of the crystal has revealed that hits in the time ranges A, B and C, are mostly concentrated in the inner ring and less in the outer ones (see Fig. 5.6), confirming the relation with the beam.

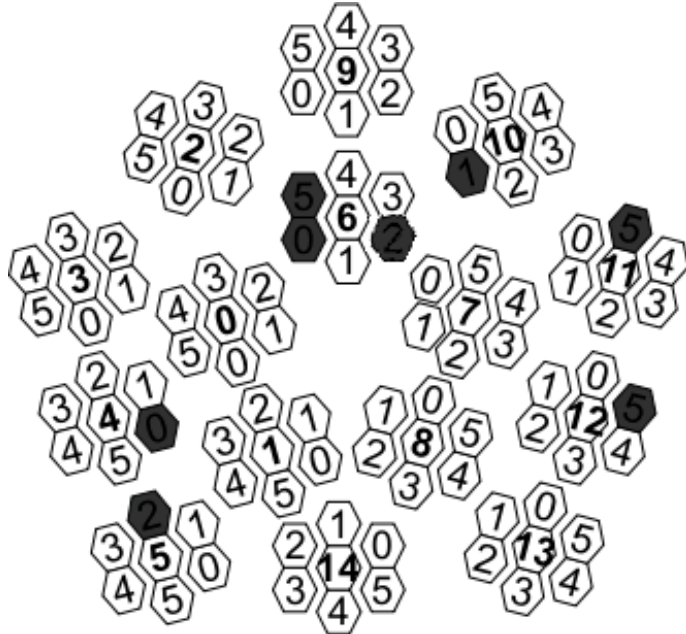


FIGURE 5.5. Scheme representing the arrangement of the 15 clusters of the Euroball array. The crystals are numbered from 0 to 6, anticlockwise, and 6 is always the central one. In this scheme, the number in the central crystal refers to the cluster number. The crystals drawn in black are not considered due to bad or missing response of the detectors.

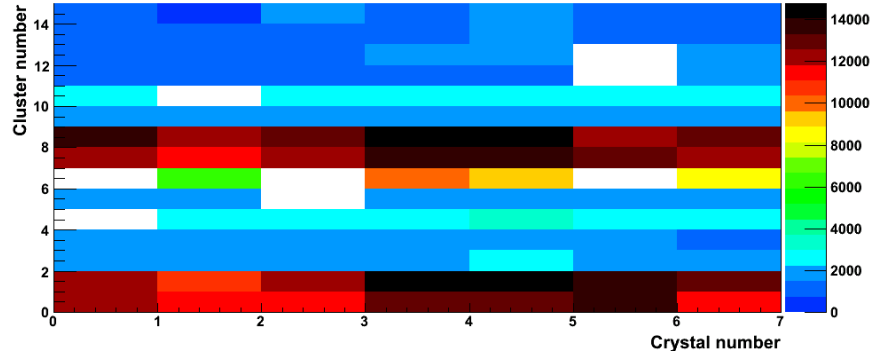


FIGURE 5.6. Hit pattern of the Euroball array when signals in time range C are selected. The clusters with a higher numbers of counts (0, 1, 6, 7, 8) are the ones forming the inner ring. The hit pattern for signals in time range A and B is similar.

Most of the hits in the time range D, instead, are mainly distributed in the upper part of the array: in cluster 6 and 7 of the inner ring and 2 and 11 of the outer ones (see Fig. 5.7).

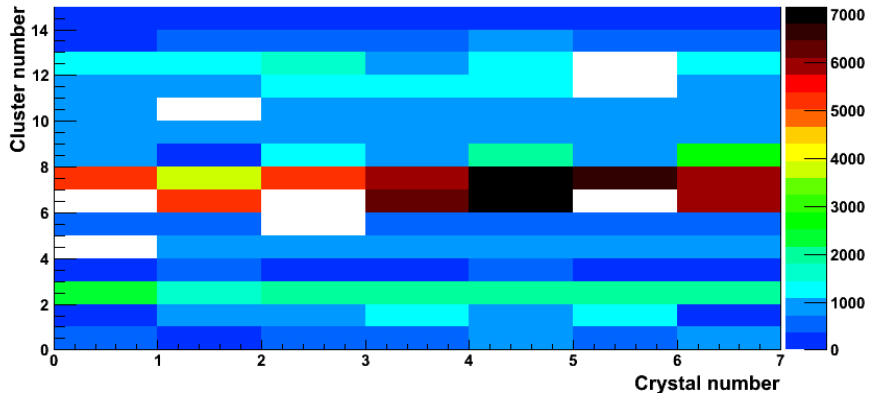


FIGURE 5.7. Hit pattern of the Euroball array when signals in time range D are selected. The clusters with a higher numbers of counts (1, 6, 7, 11, 12) are in an horizontal band in the upper part of the array (see scheme in Fig. 5.5).

The correlation between the position of the crystal which had a hit and the position of the beam at the final focal plane has then been considered. In Fig. 5.8, the events with a cluster saturated (array multiplicity equal to six in C) is compared to the case of events with low multiplicity in the time range B. In the latter case, no correlation has been seen between crystal and beam position. In the former case, a clean left-right

correlation of the crystal and beam position is observed. This behavior confirms, once more, that the particles responsible of the saturation come with the beam and have a straight trajectory. For the events with hits in the time range D, a similar correlation has not been observed.

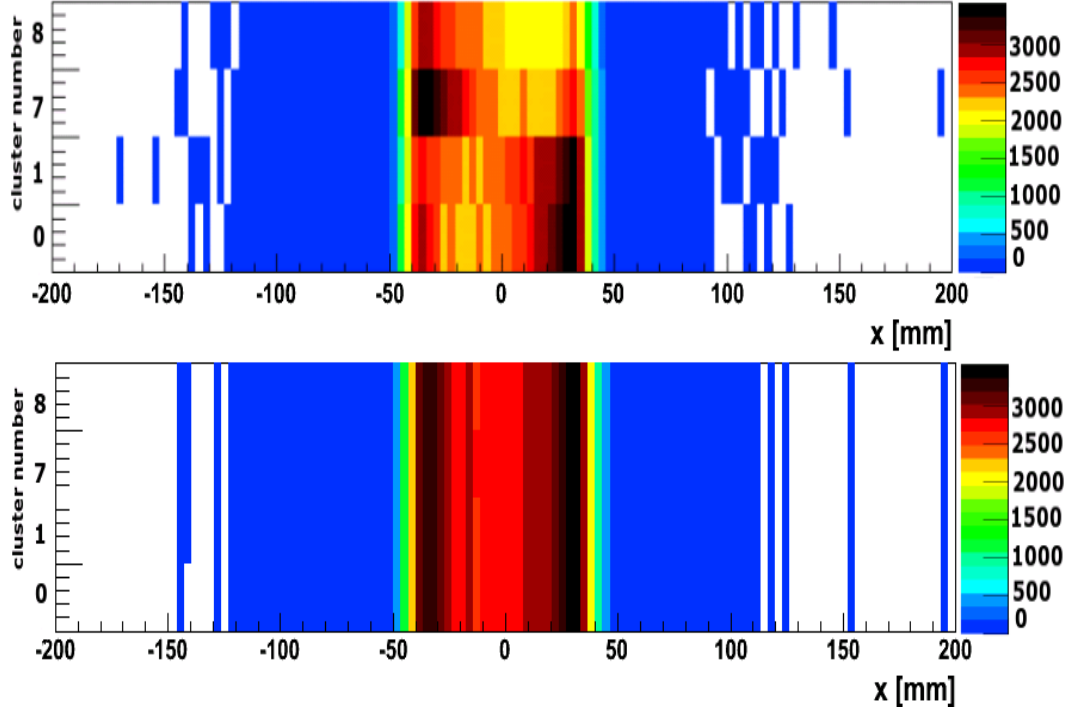


FIGURE 5.8. Position of the ions at the final focal plane of FRS from the TPC detector (scale reversed) versus the cluster number of the inner ring which registered a hit in coincidence. In the upper plot, the events with cluster multiplicity equal to six in the first delayed time peak (C) are selected, while in the lower plot events that produce low cluster multiplicity in the prompt time peak (B) are chosen. Only in the first case, a correlation between the position of the beam and the hit in the germanium detectors is noticeable.

The distribution of the energy loss in the MUSIC detector, which is related to the charge of the ion passing through (as described in Sec. 3.1.3), has been observed not to change significantly for the events that saturate the germanium detectors. This result can be explained considering that the MUSIC was set up and calibrated to detect medium-mass ions (Sn ions, in the case of the data used in this work). It is therefore plausible that it does not produce a signal in coincidence of a high-energy

light particle or that the signal generated is swamped by the bigger signal of the heavy ion. Alternatively, it is possible that the light particles are produced downstream with respect to the MUSIC, in the slits, plastic scintillators or in the target. Furthermore, Fig. 5.9 shows that the distribution of the energy loss (ΔE) of the ions in the target DSSSD, detected in coincidence with events with cluster multiplicity equal to six, is similar to the ones associated to low multiplicity. In the case of high array multiplicity, instead, the ions have a broad distribution of energy loss, which suggest their origin in fragmentation reactions of the secondary beam. One can conclude that the events that provoke saturation of the clusters are not related to the fragmentation of the beam in the target. In contrast, after neglecting the saturated cluster, the rest of event is relevant for further analysis.

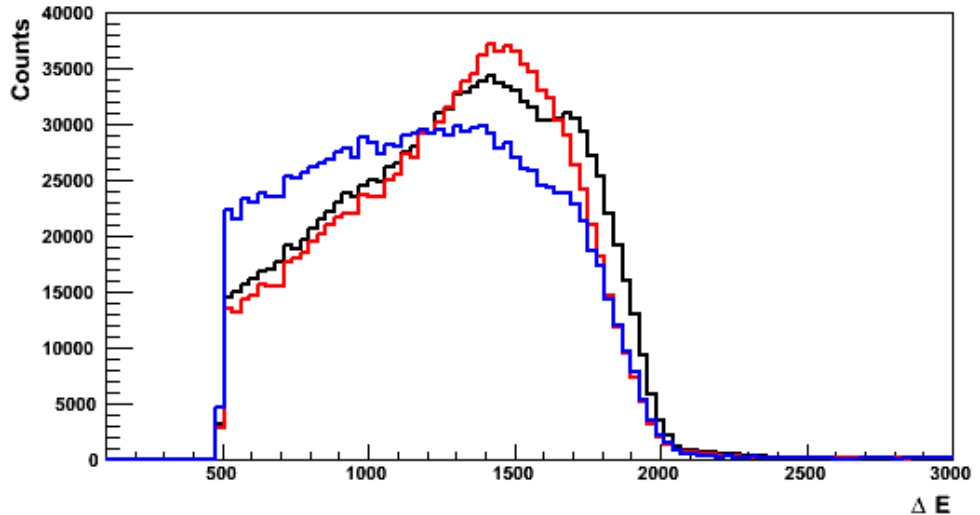


FIGURE 5.9. Energy loss (ΔE) in the target DSSSD selecting events with cluster multiplicity one and two in the time range B (black line), equal to six in the time range C (red line) and array multiplicity higher than six (blue line) in the time range C. All the distributions have been normalized at $\Delta E = 1200$ keV.

The relation between events with low ΔE (< 1000 keV) or cluster multiplicity equal to six and the number of counts in different ranges of the x position registered by the TPC (see Fig. 5.10) have been also considered. The strong increase of number of counts in the sides, as reported in Tab. 5.4, demonstrates that both type of events occur mainly when the beam is not at the central position at the final focal plane.

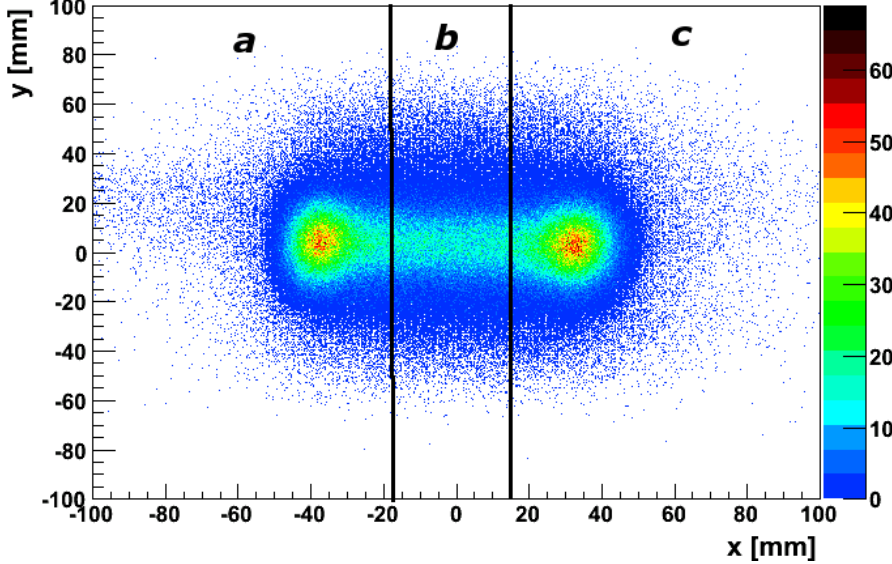


FIGURE 5.10. X position versus y position of the hit in the TPC at the final focal plane. The area has been divided in three regions (**a**, **b**, **c**), in order to verify the variation of the number of counts in the lateral region with respect to the center, applying different analysis conditions. For this picture, the condition on energy loss in the target DSSSD lower than 1000 keV has been applied.

TABLE 5.4. Fraction of counts on the sides (**a** and **c**) and on the center (**b**) at the TPC at the final focal plane, when the different conditions listed are applied. It can be noticed that, when a signal is registered in both target and wall DSSSD, the hits in the TPC are more concentrated in the center. Requiring cluster multiplicity six in the time range C and/or low energy loss in target DSSSD, instead, the number of counts on each side exceed the number of counts in the center.

Conditions	a (%)	b (%)	c (%)
hit in target & wall DSSSD	28	49	23
cluster multiplicity = 6	34	36	30
$\Delta E < 1000$	37	24	39
cluster multiplicity = 6 & $\Delta E < 1000$	39	26	35

Finally, the profiles of the γ -ray energy spectra with different time and multiplicity conditions have been examined. In Fig. 5.11 it can be observed that, when the hits in the prompt time peak (B) with low multiplicity are selected, the background lines are

almost suppressed (except for the 511 keV transition caused by the positron-electron annihilation). In the case of high multiplicity in the first delayed time peak (C), instead, the background transitions associated to interaction of neutrons with the germanium or with the material surrounding the beam line (presented in Sec. 3.4) are pronounced.

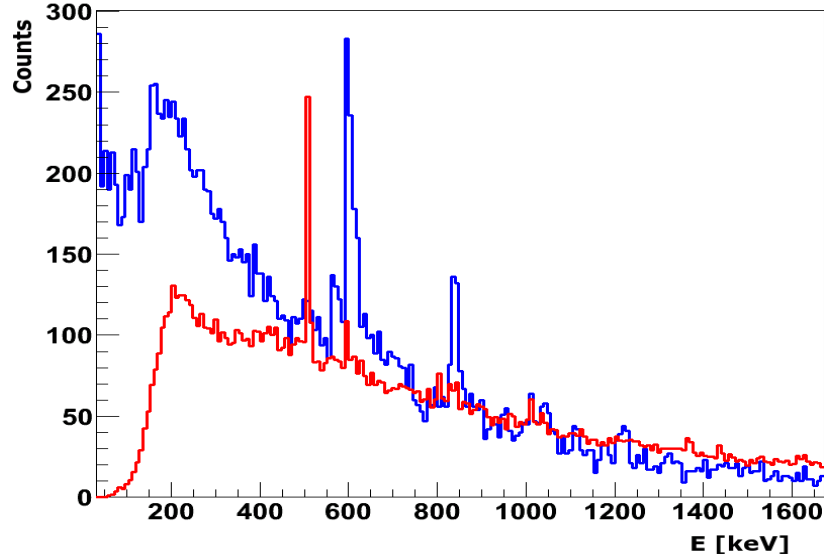


FIGURE 5.11. γ -ray energy spectra selecting the events with array multiplicity equal to one or two in the time range B (red line) and the events with array multiplicity higher than six in the time range C (blue line). In the first case, only the 511 keV transition (the energy released by the positron-electron annihilation) is pronounced above the smooth exponential background. In the second case, the 596 keV and the 834 keV neutron lines are clearly visible.

5.2 Information on the background events from AGATA

An overflow in the γ -ray energy spectra due to the saturation of the electronics is visible also in the data recorded in PreSPEC-AGATA experiments (see Fig. 5.12). The segmentation of the crystals and the advanced features of AGATA, introduced in Par. 3.3.2, open new possibilities to study the background radiation observed with the PreSPEC data. In Fig. 5.13 it is shown, as an example, two traces from the core signal of an AGATA crystal. The trace with a standard shape (on the left) has an exponential decay, while a very different shape (on the right) corresponds to a saturated signal. It is therefore evident that the latter cannot be properly processed by the preamplifier, as

it has been supposed in the case of the Euroball setup, and it can induce the presence of overflows, missing energies or unusual energy values in the data.

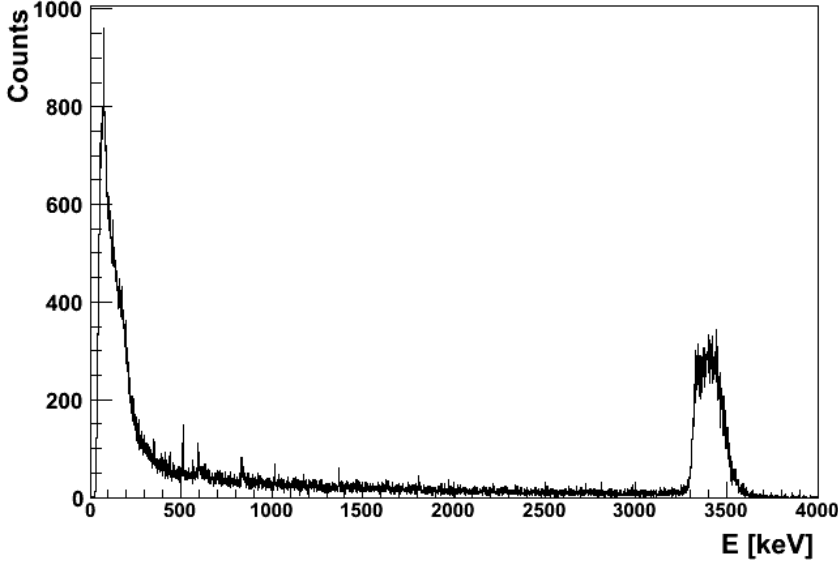


FIGURE 5.12. γ -ray energy spectrum of an AGATA crystal, from an experiment of the PreSPEC fast-beam campaign. The broad peak at very high energies is caused by the saturation of the preamplifier.

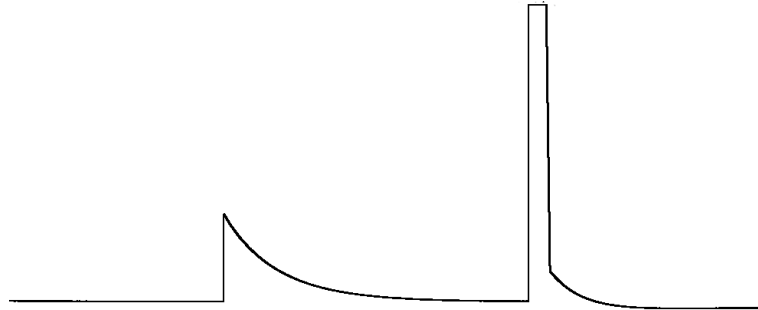


FIGURE 5.13. Core preamplifier signals of an AGATA crystal. The trace on the left has the typical shape, with an exponential decay, while the trace on the right saturates the range of the preamplifier. The energy range, in this case, was 22 MeV.

The distribution of signals in overflow in the AGATA crystals has been observed (see Fig. 5.14) and compared with the distribution of regular hits (Fig. 5.15). In both cases, as with the Euroball setup, the hits are concentrated at small angles and present a

radial distribution. Nevertheless, the number of overflows decreases more rapidly, moving to larger angles, then the standard hits.

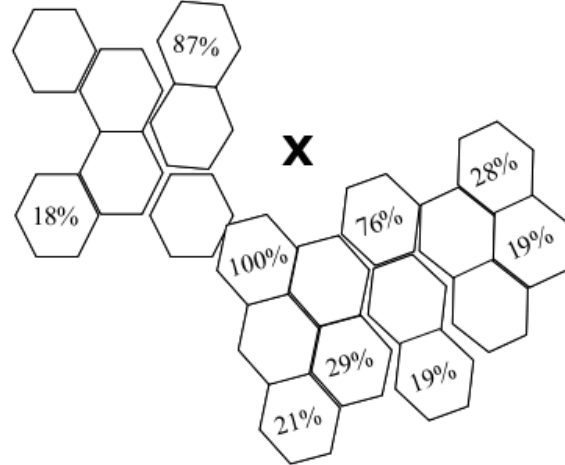


FIGURE 5.14. Distribution of the overflows in AGATA, normalized to a central crystal.

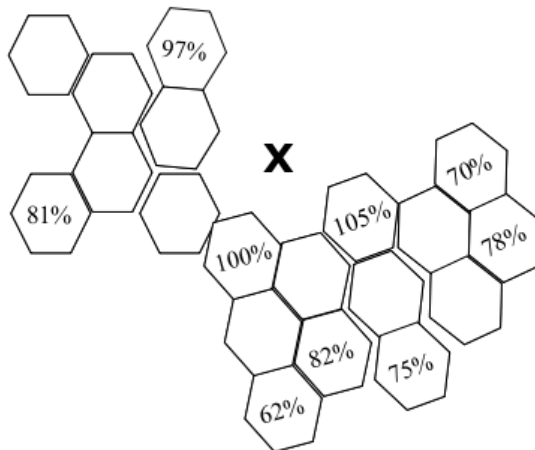


FIGURE 5.15. Distribution of the regular energy signals in AGATA, normalized to a central crystal.

Moreover, in a previous study of the occurrence of the traces saturating an AGATA crystal, it has been observed that all the segments through out the full depth of the detector are saturated [82]. Hence, it has been concluded that the phenomena of

saturation are compatible with the impact of protons at energy higher than 200 MeV. Nevertheless, due to the availability of more parameters, a more complex analysis of the AGATA data is required for a direct comparison of the evidences obtained from the Euroball data presented in the previous sections.

5.3 Impact of the background for PreSPEC experiments

The adequacy of the standard analysis procedures has been evaluated in relation to the characteristics of the background phenomena presented in the previous sections. Since the unwanted hits provoked by the saturation of the electronics are mainly in time ranges different than the prompt one, the application in the data analysis of a narrow time gate, as performed for the extraction of the $B(E2)$ value in ^{104}Sn (see Sec. 4.2.6), could at first be considered sufficient to discard them all. Nevertheless, the presence of *bad* hits in an event has been observed to entail a higher array multiplicity also of the *good* ones in the same event. A higher multiplicity, in turn, can hamper the application of commonly used analysis conditions: in the analysis of Coulomb excitation experiments (see, for example, Ref. [42]), events with array multiplicity of hits, with energy ≥ 500 keV, equal to one are usually selected in order to reduce contributions from other reactions. Fig. 5.16 shows the array multiplicity of hits in the time range B with energy ≥ 500 keV, in the case of cluster multiplicity equal to six in the time range C and at least a hit with energy between 1000 keV and 3000 keV (the energy range of the γ -rays of interest). Instead of a peak at multiplicity one, as for the general case presented in Fig. 5.4, the multiplicity is very often two or higher. In other words, in coincidence with the hit of the high energy particles, a higher multiplicity is present also in the time range considered for the analysis. For the ^{104}Sn analysis, indeed, this condition could not be applied for the final spectra since it was lowering the statistics without improving the peak-to-background ratio.

The higher multiplicity, moreover, interferes with the application of the add-back procedure, the technique used to recover γ -rays that underwent Compton scattering in one cluster detector. Standard add-back algorithms, indeed, use the cluster multiplicity as one of the parameters to select the hits in neighboring crystals. Two examples of hit distribution in the Euroball array in the case of high multiplicity in the time range C, in coincidence with high multiplicity in the time range B, are displayed in Fig. 5.17, showing that the two types of signals can be in different region of the array (figure on the left) as well as in the same cluster (figure on the right).

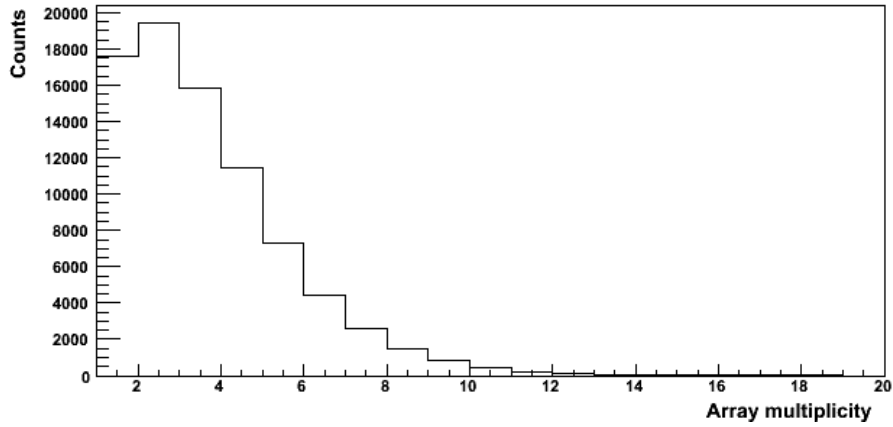


FIGURE 5.16. Array multiplicity of hits with energy higher than 500 keV in the prompt time range. A selection on the events with cluster multiplicity equal to six in the time range C and with at least a hit with energy between 1000 keV and 3000 keV in the time range B is applied.

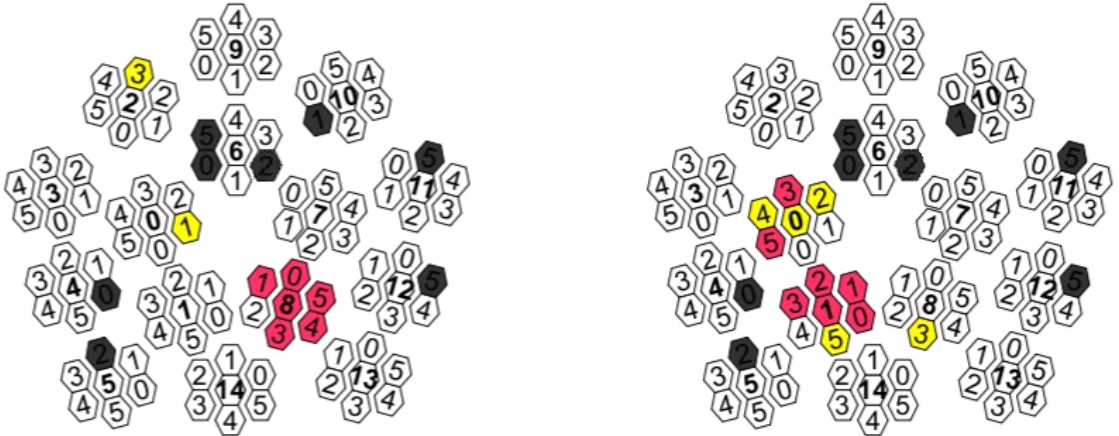


FIGURE 5.17. Examples of possible hit patterns in the Euroball array when multiplicity six in the time range C (pink crystals) occurs in coincidence with multiplicity higher than one in the time range B (yellow crystals). The case of prompt hits well separated from the saturated crystals is shown on the left. An example of an event with the prompt hits in the vicinity of the saturated crystals is on the right.

The multiplicity pattern for hits in the good energy range, after they are processed by

the add-back procedure, is shown in Fig. 5.18. In this plot (82 % of the total number of events), the events with array multiplicity equal to one are only 35 %, which means 29 % with respect to the total number of events. Only one third of the available data is therefore usefull for analysis purposes. If the energy range is then restricted to 1000-3000 keV, where the Doppler shifted γ -rays are expected to be, the number of events with multiplicity one is only 22 % with respect to the total number of events (see Fig. 5.19). Certainly this is only a rough estimation as the data analysis is usually optimized by means of many other conditions in a order to maximize the extraction of usefull data. Nevertheless, it provides indications that the structure of the data is dominated in large part by useless hits.

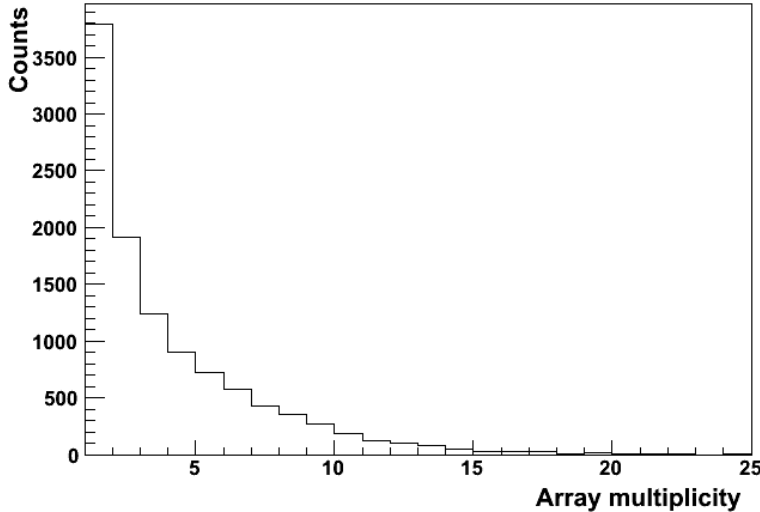


FIGURE 5.18. Array multiplicity of all the hits in the good energy range after add-back.

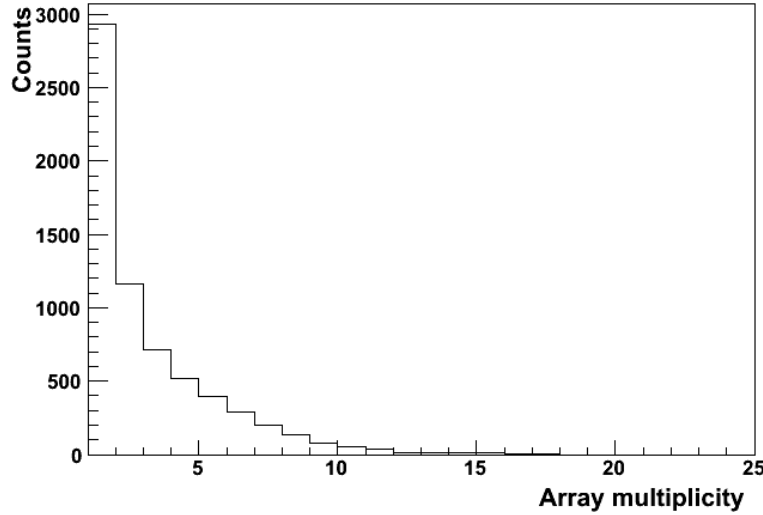


FIGURE 5.19. Array multiplicity of all the hits between 1000 - 3000 keV after add-back.

Moreover, the frequent occurrence of events that blinds part of the array can cause a severe reduction of the detection efficiency. In Tab. 5.5, the average presence, per event, of the different type of hits in one crystal of the Euroball Cluster array, if at least one hit with bad energy value occurred, is presented. The three rings are considered separately as the intensity of the beam varies with the θ angle due to the Lorentz boost. In Tab. 5.6, the same numbers for events with only good hits in the array are shown. From these results, it can be observed that the presence of bad hits reduces the detection efficiencies of the middle and outer rings. The increased detection of good hits in the inner ring, instead, can be related to the increased multiplicity observed in Fig. 5.17, which is also a drawback, as already discussed, since it hinders the application of standard conditions in the analysis.

TABLE 5.5. Average presence of the different hit types in the three rings of the Euroball array, per crystal and per event, when at least one bad hit is present (58 % of the total number of events).

Energy range	inner ring (%)	middle ring (%)	outer ring (%)
low	2.1	0.3	0.2
high	4.6	0.4	0.5
missing	10.5	2.1	1.2
good	4	0.6	0.5

TABLE 5.6. Average presence of the hits with good energy values in the three rings of the Euroball array, per crystal and per event, when no bad hits are present (42 % of the total number of events).

Energy range	inner ring (%)	middle ring (%)	outer ring (%)
good	3	1.3	1.4

Assuming that the background hits are dominating over the γ -rays of interest, the former reduce the number of crystals available for the detection of the latter. A loss in detection efficiency has been therefore calculated considering the array multiplicity patterns. Since the probability of detecting one γ -ray in an array of N detectors with efficiency ϵ_{sing} is [83]

$$\epsilon_0 = N\epsilon_{sing} , \quad (5.1)$$

the probability of detecting one γ -ray, when a given multiplicity N_{mult} of background hits is present, can be expressed as

$$\epsilon_{red} = \epsilon_{sing}(N - N_{mult}) . \quad (5.2)$$

Considering then the number of events (n_{ev}) for each multiplicity value ($i = 1, 2, \dots, N_{mult}^{max}$), the average reduced efficiency (ϵ_{red}^{av}) results:

$$\epsilon_{red}^{av} = \frac{\sum_i \epsilon_{red}(i) \cdot n_{ev}}{\sum_i n_{ev}(i)} . \quad (5.3)$$

The efficiency of the full Euroball Cluster array and the efficiency scaled for the number of crystals working properly during the experiment are reported in Tab. 5.7.

TABLE 5.7. Calculated efficiencies of the three rings (positioned at 700 mm distance from the target) of the full Euroball Cluster array, for γ -rays of energy equal to 1.3 MeV, and the efficiencies scaled considering only the available crystals.

Ring	efficiency full array [84]	efficiency with available crystals
inner	0.010	0.0092
middle	0.0091	0.0083
outer	0.0089	0.0084
total	0.0281	0.0258

Considering the array multiplicity in each ring for the events with at least a bad hit (58 % of the total number of events) shown in Fig. 5.20, the average reduced efficiency, for this part of the events, has been calculated as $\epsilon_{red}^{av}=0.0216$ (see Tab. 5.8). If for the rest of the events (42 % of the total number of events) the total efficiency (0.0258 %) is assumed, the average reduced efficiency for all the events is $\epsilon_{red}^{av}=0.0234$. The loss of efficiency is therefore 9.5 %, with respect to the total efficiency. In Fig. 5.21, the array multiplicity in each ring, as in the previous figure, considering events with only good hits are presented.

TABLE 5.8. Reduced efficiency for the detection of one γ -ray in the three rings of the Euroball cluster array when the number of crystals is decreased in relation to the multiplicity of bad hits.

Ring	ϵ_{red}^{av}
inner	0.0068
middle	0.0074
outer	0.0073
Tot	0,0216

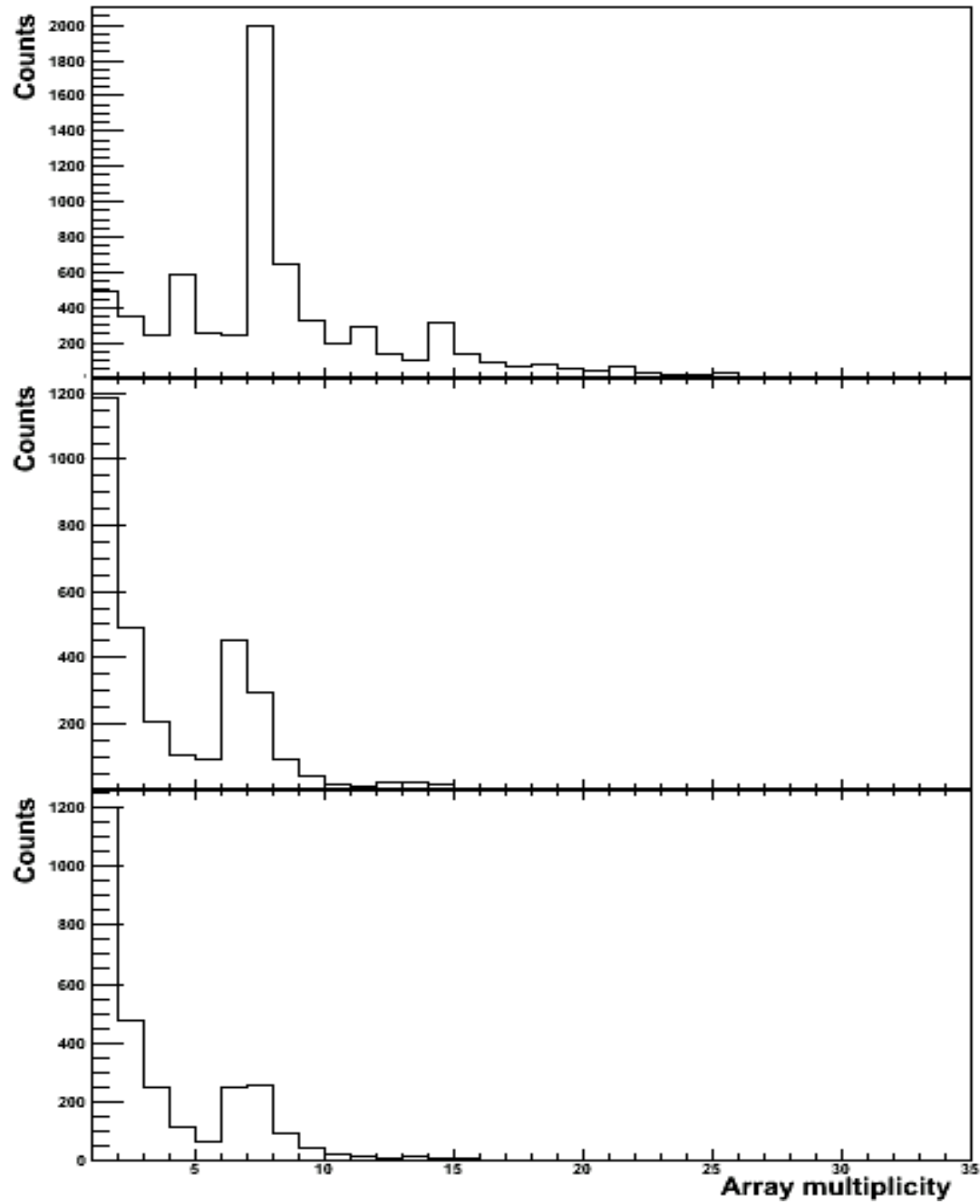


FIGURE 5.20. Array multiplicity for the events with at least a bad hit (58 % of the total number of events) (from top to bottom: for the inner, the middle and the outer ring).

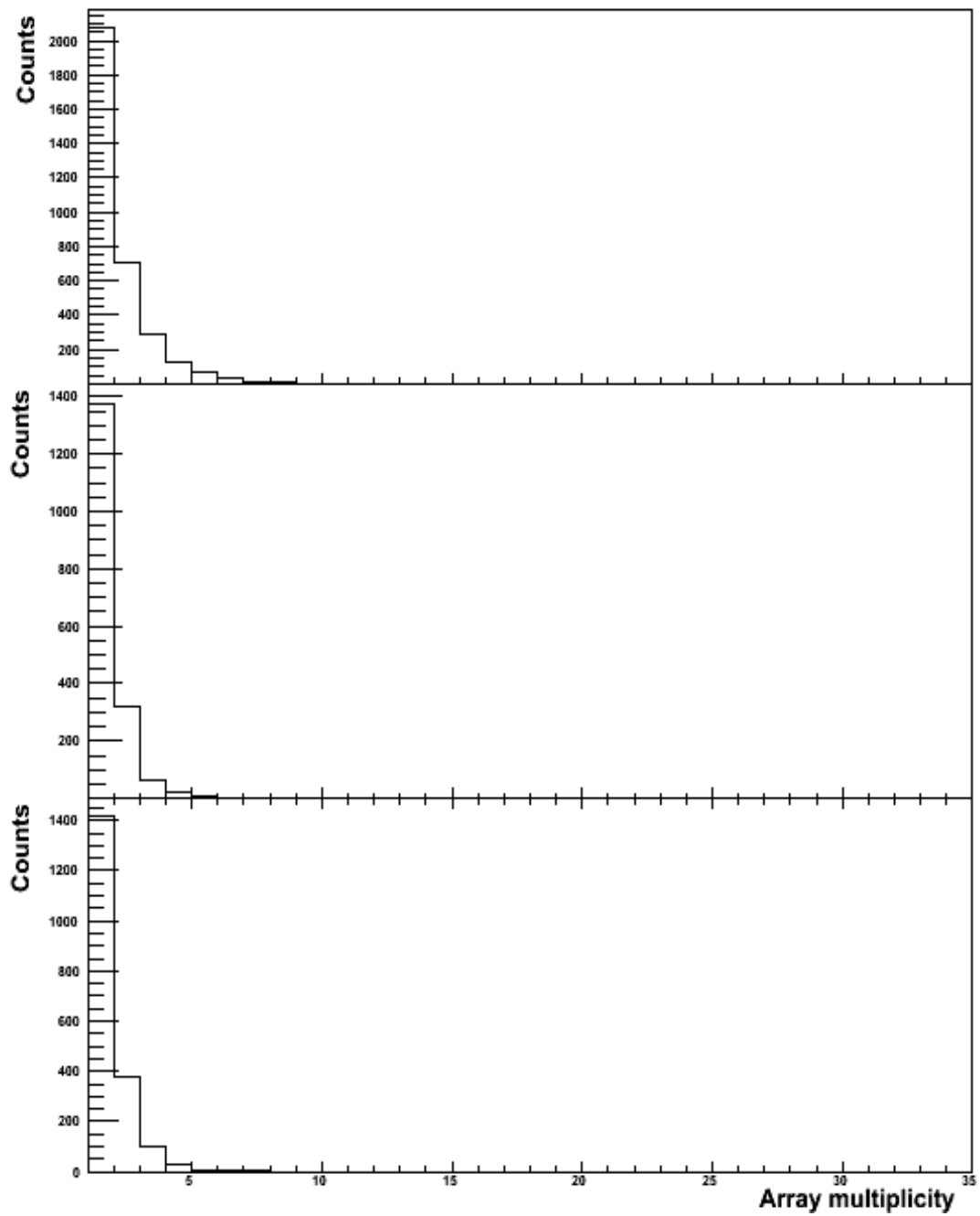


FIGURE 5.21. Array multiplicity for the events with only good hits (42 % of the total number of events) (from top to bottom: for the inner, the middle and the outer ring).

Taking then into account that the hits in the photopeak of the nuclear reaction of interest are only a negligible percentage of the total number of counts in the so called (in this chapter) *good* energy range of the γ -ray spectrum, the *good* hits also can be counted as background hits (produced in the processes described in Sec. 3.4) which reduce the detection efficiency of the array. The array multiplicity for the three rings considering both good and bad hits are shown in Fig. 5.22. The reduced efficiency obtained considering these multiplicity values are reported in Tab. 5.9. From these numbers, the total efficiency of 0.0258 is decreased to 0.0226, which corresponds to a loss of 13% of the efficiency.

TABLE 5.9. Reduced efficiency for the detection of one γ -ray in the three rings of the Euroball cluster array when the number of crystals is decreased in relation to the multiplicity of all the hits.

Ring	ϵ_{red}^{av}
inner	0.0075
middle	0.0076
outer	0.0075
Tot	0.0226

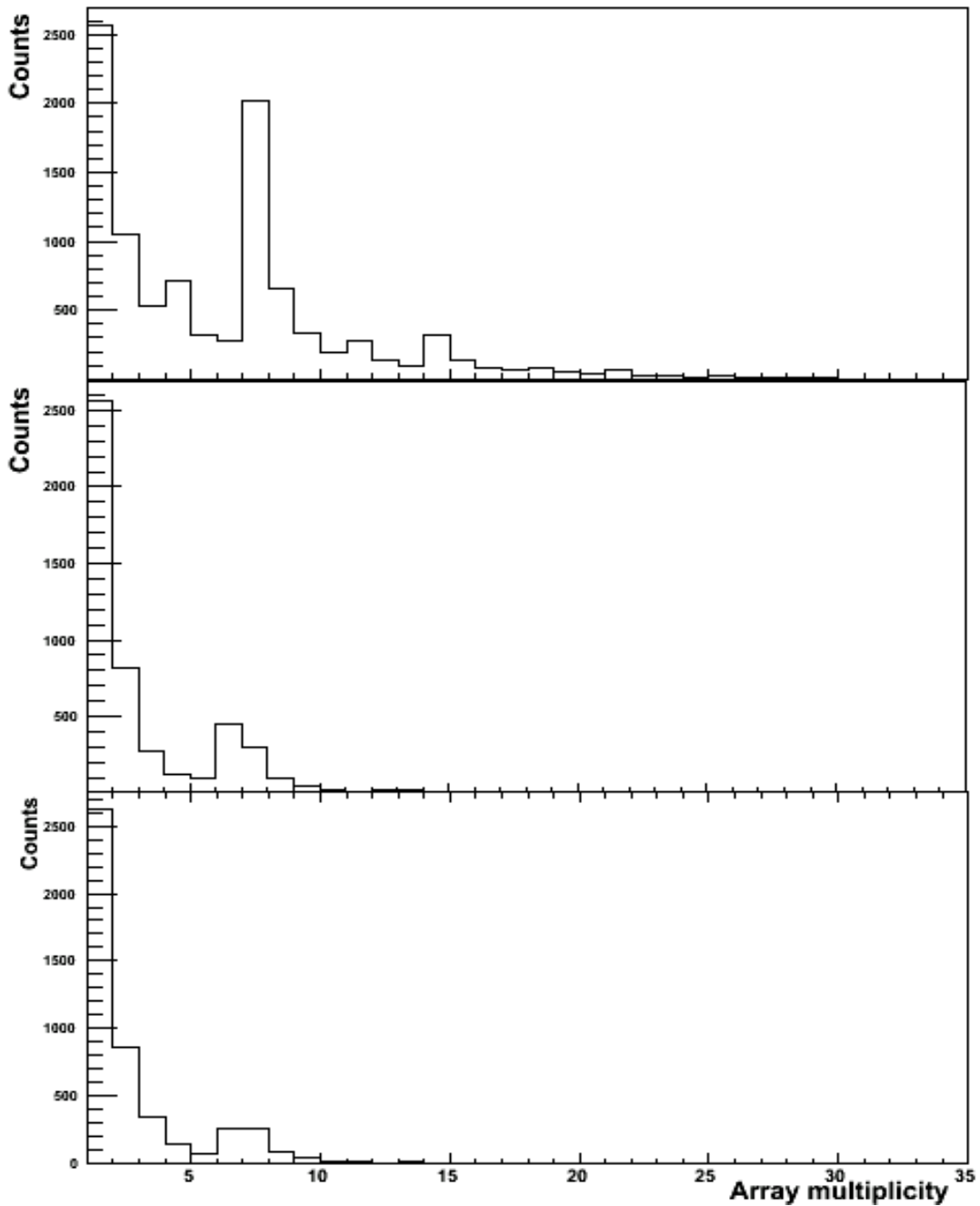


FIGURE 5.22. Array multiplicity of all the hits in the event (from top to bottom: for the inner, the middle and the outer ring).

5.4 Summary and conclusions

The signals produced in the germanium detectors of Euroball Cluster array by either γ -rays or high energy particles have been separated in four time ranges and four energy ranges. Hence, from the analysis of the correlations between the hits in the germanium detectors and the signals registered in other detectors in the same events, the following components of the background have been distinguished:

1. atomic background and radiation from the interaction of the beam with the surrounding material, as described in Sec. 3.4, with
 - energy signals in the good range,
 - time signals in range B (prompt, see Tab. 5.1),
 - low cluster multiplicity;
2. γ -rays emitted by the ions implanted in the Lycca dE-E telescope, with
 - energy signals in the good range,
 - time signals in range C (first delayed peak),
 - low cluster multiplicity;
3. high energy protons, produced in the final focal plane or in the target area, mainly when the beam ions are off the central trajectory, with
 - energy signals in overflow, in the low range or without energy signals
 - time signals in range C and A (peak before the prompt),
 - cluster multiplicity mainly one and six;
4. high-energy particles, whose origin could not be clarified, with
 - energy signals in overflow, in the low range or without energy signals
 - time signals in range D (second delayed peak), B and A,
 - cluster multiplicity higher than one considerably present.

This last component of the background, at variance with all the other classes of events, is characterized by a particular distribution of the hits in the upper part of the Euroball Cluster array. However, with the information provided by the Euroball cluster array, its nature could not be clearly established.

The impact of the background radiation has been estimated as:

- $\sim 9.5\%$ loss in efficiency, due to the interaction of high energy protons (p. 77),
- $\sim 13\%$ loss in efficiency, considering all the background components (p. 80),
- $\sim 78\%$ of data not usefull for the extraction of the aimed physics result (p. 74, 75).

However, the estimates of loss of efficiency represent only a minimum value, as only few parameters are included. In particular, the dead-time of the DGF modules processing the hits has also to be taken into account. This parameter is rate-dependent and it can severely decrease the detection efficiency at high rates.

The conclusions of the analysis described in this chapter give support to the implementation of some devices in the future experimental setups at FAIR:

- an high energy threshold that prevent high energy particles to trigger the DAQ, in order to reduce the dead time of the system,
- a fast-reset modules, to decrease the time needed by the front-end electronics to recover from the saturation state,
- a shield between the identification and tracking detectors and the target area.

A detailed analysis of the background events with AGATA data will provide, through the tracking of the incoming particles, a better understanding of the sources of all the background events.

Some parts of this thesis have been already published or have contributed to scientific articles.

The following list gives the complete record of scientific publications that I have coauthored:

- *Analysis and results of the ^{104}Sn Coulomb excitation experiment*, G. Guastalla et al., J. Phys.: Conf. Ser. 533 012047, 2014.
- *Coulomb Excitation of ^{104}Sn and the Strength of the ^{100}Sn Shell Closure*, G. Guastalla et al., Phys. Rev. Lett. 110, 172501, 2013.
- *Proton Radii of $^{12-17}\text{B}$ Define a Thick Neutron Surface in ^{17}B* , A. Estrade et al., Phys. Rev. Lett. 113, 132501, 2014
- *On the Road to FAIR: 1st Operation of AGATA in PreSPEC at GSI*, N. Pietralla et al., EPJ Web of Conferences 66, 02083, 2014.
- *Level lifetimes and quadrupole moments from Coulomb excitation in the Ba chain and the $N = 80$ isotones*, C. Bauer et al., EPJ Web of Conferences 38, 10003, 2012.
- *Doped polysiloxane scintillators for thermal neutrons detection*, A. Quaranta, et al., Journal of Non-Crystalline Solids 127, 1921-1925, 2011.
- *The RIPEN Array for Neutron Spectroscopy*, M. Cinausero, T. Marchi, G. Guastalla, F. Gramegna, V. Kravchuk for the NUCLEX Collaboration, LNL Annual Report 2009.
- *Doped Polysiloxane Scintillators for Thermal Neutrons Detection*, A. Quaranta, S. Carturan, T. Marchi, M. Buffa, M. Degerlier, M. Cinausero, G. Guastalla, F. Gramegna, G. Valotto, G. Maggioni, LNL Annual Report 2009.
- *Statistical Decay of Light Hot Nuclei*, G. Baiocco et al., LNL Annual Report 2009.
- *Light Charged Particle Emission in the Reaction $^{16}\text{O} + ^{116}\text{Sn}$ at 192 MeV*, S. Sambi et al., LNL Annual Report 2009.

Bibliography

- [1] <http://www.nndc.bnl.gov/chart/>
- [2] M. G. Mayer and J. H. D. Jensen, *Elementary Theory of Nuclear Shell Structure*, 1955, Wiley.
- [3] D. Bazin, *Nature*, vol. 486, pp. 330–331, 2012.
- [4] F. Nowacki, *Act. Phys. Pol.*, vol. B 38, pp. 1369–1373, 2006.
- [5] G. Lorusso et al., *Phys. Rev. C*, vol. 86, p. 014313, 2012.
- [6] G. D. Dracoulis, *Phys. Scr.*, vol. T152, p. 014015, 2013.
- [7] S. N. Liddick et al., *Phys. Rev. Lett.*, vol. 97, p. 082501, 2006.
- [8] C. B. Hinke et al., *Nature*, vol. 486, p. 341, 2012.
- [9] A. Bohr and B. Mottelson, *Nuclear Structure*, vol. 1, 1969.
- [10] E. Caurier, F. Nowacki, A. Poves, and A. P. Zuker, *Rev. Mod. Phys.*, vol. 77, p. 427, 2005.
- [11] H. Grawe, *Lect. Notes Phys.*, vol. 651, pp. 33–75, 2004.
- [12] J. H. Wilkinson, *The algebraic Eigenvalue problem*, 1965.
- [13] A. Poves, *Lecture Notes in Physics*, vol. 138, pp. 282–287, 1981.
- [14] P. J. Brussaard and P. W. M. Glaudemans,, “Shell-model applications in nuclear spectroscopy,” 1977, North-Holland publishing company.
- [15] T. R. H. Skyrme, *Nucl. Phys.*, vol. 9, pp. 615, 635, 1959.
- [16] D. H. Vautherin and D. M. Brink, *Phys. Rev. C*, vol. 5, p. 626, 1972.
- [17] D. Gogny, *Nucl. Phys.*, vol. A, pp. 237, 399, 1975.

Bibliography

- [18] J. Dechargé and D. Gogny, *Phys. Rev.*, vol. 21, p. 1568, 1980.
- [19] T. Faestermann, M. Górska, and H. Grawe, *Prog. Part. Nucl. Phys.*, vol. 69, pp. 85–130, 2013.
- [20] M. Hjorth-Jensen, T. T. Kuo, and E. Osnes, *Phys. Rep.*, vol. 261, pp. 125–270, 1995.
- [21] S. Bogner, T. T. S. Kuo, L. Coraggio, and A. and N. Itaco, *Phys. Rev. C*, vol. 65, p. 051301, 2002.
- [22] M. Hjorth-Jensen, T.T.S. Kuo, and E. Osnes, *Phys. Rep.*, vol. 261, p. 125, 1995.
- [23] I. Talmi and I. Unna, *Phys. Rev. Lett.*, vol. 4, p. 469, 1960.
- [24] H. Grawe, A. Blazhev, M. Górska, R. Grzywacz, H. Mach, and I. Mukha, *Eur. Phys. J.*, vol. A 27, pp. 257–267, 2006.
- [25] D. Seweryniak et al., *Phys. Rev. Lett.*, vol. 99, p. 022504, 2007.
- [26] H. G. K. Langanke and G. Martínez-Pinedo, *Rep. Prog. Phys.*, vol. 70, p. 1525, 2007.
- [27] A. F. Lisetskyi, B. A. Brown, M. Horoi, and H. Grawe, *Phys. Rev. C*, vol. 70, p. 044314, 2004.
- [28] M. Wang et al., *CPC*, vol. 36, pp. 1603–2014, 2012.
- [29] <http://www.nndc.bnl.gov/nudat2/>
- [30] H. Grawe and M. Lewitowicz, *Nucl. Phys.*, vol. A 693, pp. 116–132, 2001.
- [31] J. Janas et al., *Eur. Phys. J.*, vol. A 23, pp. 197–200, 2005.
- [32] M. Sasano et al., *Phys. Rev. Lett.*, vol. 107, p. 202501, 2001.
- [33] J. R. Beebe et al., *Nucl. Phys. A*, vol. 746, p. 471, 2004.
- [34] D. Radford et al., *Nucl. Phys. A*, vol. 752, p. 264, 2005.
- [35] J. Terasaki, J. Engel, W. Nazarewicz, and M. Stoitsov, *Phys. Rev. C*, vol. 66, p. 054313, 2002.
- [36] J. M. Allmond et al., *Phys. Rev. Lett.*, vol. 112, p. 172701, 2014.
- [37] I. Talmi, *Nucl. Phys. A*, vol. 172, p. 1, 1971.

Bibliography

- [38] J. Cederkäll et al., *Phys. Rev. Lett.*, vol. 98, p. 172501, 2007.
- [39] A. Ekström et al., *Phys. Rev. Lett.*, vol. 101, p. 012502, 2008.
- [40] C. Vaman et al., *Phys. Rev. Lett.*, vol. 99, p. 162501, 2007.
- [41] R. Kumar et al., *Phys. Rev. C*, vol. 81, p. 024306, 2010.
- [42] A. Banu et al., *Phys. Rev. C*, vol. 72, p. 061305, 2005.
- [43] P. Doornenbal et al., *Phys. Rev. C*, vol. 78, p. 031303, 2008.
- [44] A. Jungclaus et al., *Phys. Lett.*, vol. B 695, pp. 110–114, 2011.
- [45] J. F. Liang et al., *Phys. Rev. Lett.*, vol. 91, p. 152701, 2003.
- [46] W. S. Freeman et al., *Phys. Rev. Lett.*, vol. 50, p. 1563, 1983.
- [47] J. M. Allmond et al., *Presentation at Nuclear Structure 2012, Argonne Laboratory*, 2012.
- [48] O. Kester et al., *Nucl. Instrum. Methods Phys. Res. Sec. B*, vol. 204, p. 20, 2003.
- [49] A. Stolz et al., *Nucl. Instrum. Methods Phys. Res. Sec. B*, vol. 241, p. 858, 2005.
- [50] T. Otsuka et al., *Phys. Rev. Lett.*, vol. 95, p. 232502, 2005.
- [51] H. Geissel et al., *Nucl. Instrum. Methods Phys. Res.*, vol. B 70, pp. 286–297, 1992.
- [52] H. J. Wollersheim et al., *Nucl. Instrum. Methods Phys. Res.*, vol. A 537, p. 637, 2005.
- [53] P. Golubev et al., *Nucl. Instrum. Methods Phys. Res.*, vol. A 723, pp. 55–66, 2013.
- [54] N. Pietralla et al., *EPJ Web of Conferences*, vol. 66, 2014.
- [55] F. Camera et al., *EPJ Web of Conferences*, vol. 66, 2014.
- [56] G. Münzenberg, *Progress in Particle and Nuclear Physics*, vol. 46, pp. 335–342, 2001.
- [57] G. F. Knoll, *Radiation Detection and Measurement*, 2010.
- [58] F. Ameil, M. Danchev, P. Boutachkov, J. Kurcewicz, S. Pietri, D. Ralet, J. Gerl, and N. Pietralla, *GSI Scientific Report 2011*, vol. PHN-NUSTAR-FRS-29, 2011.
- [59] <http://www-w2k.gsi.de/frs/technical/FRSsetup/detectors-new.asp>.

Bibliography

- [60] H. J. Wollersheim, *Act. Phys. Pol.*, vol. 42, pp. 705–716, 2011.
- [61] R. Hoischen et al., *Nucl. Instrum. Methods Phys. Res.*, vol. A 654, p. 354, 2011.
- [62] X.-R. I. Associates, “Digital gamma finder (dgf) and user’s manual and version 3.04,” 2004.
- [63] S. Akkoyun et al., *Nucl. Instr. Meth.*, vol. A 668, pp. 26–58, 2012.
- [64] <http://www-win.gsi.de/agata/overview.htm>.
- [65] P. Bednarczyk et al., *Act. Phys. Pol.*, vol. 41, pp. 505–510, 2010.
- [66] P. Doornenbal, *PhD Thesis*, 2004.
- [67] G. Guastalla et al., *J. Phys.: Conf. Series*, vol. 533, p. 012047, 2014.
- [68] J. R. Taylor, *An Introduction to Error Analysis: The Study of Uncertainties in Physical Measurements*, 1996.
- [69] C. A. Bertulani and G. Baur, *Nucl. Phys. A*, vol. 442, p. 744, 1985.
- [70] L. A. Banu, *PhD Thesis*, 2005.
- [71] C. A. Bertulani, C. M. Campbell, and T. Glasmacher, *Comput. Phys. Commun.*, vol. 152, p. 317, 2003.
- [72] G. Guastalla et al., *Phys. Rev. Lett.*, vol. 110, p. 172501, 2013.
- [73] P. Doornenbal, *private communication*.
- [74] V. M. Bader et al., *Phys. Rev. C*, vol. 88, p. 051301, 2013.
- [75] A. Bohr and B. Mottelson, *Nuclear Structure*, vol. 2, 1975.
- [76] T. Bäck, C. Qi, B. Cederwall, R. Liotta, F. G. Moradi, A. Johnson, R. Wyss, and R. Wadsworth, *Phys. Rev. C*, vol. 87, p. 031306, 2013.
- [77] P. Doornenbal et al., *arXiv:1305.2877[nucl-ex]*, 2013.
- [78] R. E. Shroy, A. K. Gaigalas, G. Schatz, and D. B. Fossan, *Phys. Rev. C*, vol. 19, p. 1324, 1979.
- [79] H. Schnare et al., *Phys. Rev. C*, vol. 54, p. 1598, 1996.
- [80] M. Sandzelius et al., *Phys. Rev. Lett.*, vol. 99, p. 022501, 2007.

Bibliography

- [81] E. Caurier, F. Nowacki, A. Poves, and K. Sieja, *Phys. Rev. C*, vol. 82, p. 064304, 2010.
- [82] N. Lalovic, *private communication*.
- [83] S. Y. Van Der Werf, *Nucl. Instr. Meth.*, vol. 153, p. 221, 1978.
- [84] J. Simpson , R. Griffith , and K. Fayz, *RISING Designs Status for Steering Committee Meeting on 7/10/2002*, 2002.

Acknowledgements

This work was supported by the Helmholtz International Center for FAIR (HIC for FAIR) within the LOEWE program by the State of Hesse (BMBF under grant No. 05P12RDFN8).

I would like to thank Prof. Dr. Norbert Pietralla, for providing me a position as PhD student in his group in TU Darmstadt and for the continuous supervision and support along these years.

I am grateful to Dr. Magda Górska, for supervising closely my work all these years, teaching me nuclear structure with patience, enriching my education in different ways and, especially, for the extraordinary understanding and support.

My gratitude goes also to Dr. Jürgen Gerl, for taking me in his group and helping me in the analysis during the first year, as well as in all the other occasions it was needed.

Few words here will not be enough to express once more my gratitude to Joachim Cederkäll, Douglas DiJulio, Hubert Grawe and of course Magda for the help writing the publication on the result of ^{104}Sn , their excellent contributions and the comprehension toward my difficulties due to a health problem. Special thanks also to Tugba and Natasa for the practical support in the same period.

In the occasion of the submission of this final work, I have to think how the PhD started and to thank Namita for many things, as for rescuing me in the university bureaucracy, for sharing good and bad moments and for being my first real good friend here in Germany. I am grateful, of course, to all the gamma-spectroscopy group in GSI, including all the persons that came and that left it in these years. Thanks to Tobias for the good friendship, to Cesar for being the best officemate, to Edana and Farheen for answering all my questions, to Stephane for the numerous explanations, to Ivan for the clarifications I needed for the thesis and all the other people that I bothered with my doubts and to who I might have forgotten. My gratitude for Liliana is due, in particular, to her precious gift for seeing all the moments of discomfort and to her dedication to change them.

Lots of thanks also to my close friends Frederic, Natasa, Marco and Michele, for becoming the fundamental and nicest part of this experience. Infinite gratitude to Damian for being nothing less than the perfect mate also in this adventure.

Bibliography

Erklärung zur Eigenständigkeit

Hiermit versichere ich die vorliegende Dissertation ohne Hilfe Dritter nur mit den angegebenen Quellen und Hilfsmitteln angefertigt zu haben. Alle Stellen, die aus Quellen entnommen wurden, sind als solche kenntlich gemacht. Diese Arbeit hat in gleicher oder ähnlicher Form noch keiner Prüfungsbehörde vorgelegen.

Darmstadt, Oktober 14, 2014.

Giulia Guastalla

Giulia Guastalla

Planckstrasse 1

Darmstadt, Germany 64291

g.guastalla@gsi.de

Persönliche Daten

Geburtsdatum	August 19, 1986
Geburtsort	Mantova, Italien
Staatsangehörigkeit	Italienisch
Familienstand	Ledig

Schulausbildung

2000 - 2005 Liceo Classico Virgilio, Mantova (humanistisches Gymnasium), Italien.

Studium

2005 - 2008 Bachelor in Physik an der Universität zu Bologna, Italien.

2008 - 2010 Master in Teilchenphysik und Kernphysik an der Universität zu Bologna, Italien.

Berufliche Tätigkeiten

2011 Beschäftigung als Doktorandin im Bereich Experimentelle Kernstrukturphysik,
GSI Helmholtzzentrum für Schwerionenforschung GmbH, Darmstadt, Deutschland.